GLAUKOMATÖSE VERÄNDERUNGEN IN DER βB1-CTGF MAUS

DISSERTATION ZUR ERLANGUNG DES DOKTORGRADES DER MEDIZIN DER FAKULTÄT FÜR BIOLOGIE UND VORKLINISCHE MEDIZIN DER UNIVERSITÄT REGENSBURG

vorgelegt von
Felix Hutmacher

aus
Regensburg

im Jahr
2025

Das Promotionsgesuch wurde eingereicht am:
31.08.2025

Die Arbeit wurde angeleitet von:
Prof. Dr. rer. nat. Rudolf Fuchshofer

GLAUKOMATÖSE VERÄNDERUNGEN IN DER βB1-CTGF MAUS

DISSERTATION ZUR ERLANGUNG DES DOKTORGRADES DER MEDIZIN DER FAKULTÄT FÜR BIOLOGIE UND VORKLINISCHE MEDIZIN DER UNIVERSITÄT REGENSBURG

vorgelegt von
Felix Hutmacher

aus
Regensburg

im Jahr
2025

Contents

1 Abstract

1.1 Deutsch

Das Glaukom zählt zu den häufigsten Ursachen irreversibler Erblindung und ist durch eine chronische Schädigung des Sehnervs mit einem fortschreitenden Verlust der Axone retinaler Ganglienzellen gekennzeichnet. In früheren Studien wurde ein transgenes Mausmodell mit einer linsenspezifischen Überexpression von CTGF validiert, das pathologische Veränderungen des Glaukoms repliziert, wie erhöhten Augeninnendruck, Umbau der extrazellulären Matrix und Axonverlust. Dieses transgene Mausmodell wurde in dieser Arbeit erneut validiert, wobei der Schwerpunkt auf Mäusen im Alter von 26 und 52 Wochen lag. Zu den wichtigsten Untersuchungen gehörten Messungen des Augeninnendrucks, Elektronenmikroskopie und Fluoreszenzmikroskopie. Es wurden verschiedene Instrumente zur Objektivierung der Bildanalyse getestet, darunter die Quantifizierung der Helligkeit in fluoreszenzmikroskopisch aufgenommenen Bildern, die Messung von Veränderungen in elektronenmikroskopisch aufgenommenen Bildern und die automatische Axonzählung, ausserdem erfolgte die erstmalige Anwendung von Structured Illumination Microscopy an Proben aus ganzen Augen von Mäusen. Zudem wurde mit dem Transfer des genetischen Konstrukts auf die Stämme BALB/c und C57BL/6J begonnen. Bei Mäusen im Alter von 26 und 52 Wochen zeigten sich signifikante Unterschiede zwischen transgenen und Wildtyp-Mäusen. Der Vergleich der Helligkeiten zur Objektivierung von Unterschieden zwischen fluoreszenzmikroskopischen Bildern erwies sich als zuverlässig, und die Anwendung von Structured Illumination Microscopy war erfolgreich. Die automatische Axonenzählung ergab jedoch im Vergleich zur manuellen Zählung eine uneinheitlich hohe Axonenzahl, was darauf hindeutet, dass vor der Anwendung eine tiefergehende Validierung erforderlich ist. Die Validierung des Mausmodells an BALB/c- und C57BL/6J-Stämmen war bis zum Abschluss der Arbeit noch nicht abgeschlossen. Insgesamt bestätigt diese Arbeit die Bedeutung des CTGF-Modells für die Glaukomforschung, insbesondere in älteren Altersgruppen, und öffnet Möglichkeiten für die Anwendung des Modells in Langzeitstudien.

1.2 English

Glaucoma, a leading cause of irreversible blindness, is defined as chronic neuropathy and gradual loss of axons of retinal ganglion cells. Previous studies validated a transgenic mouse model with a lens-specific overexpression of CTGF that replicates key features of glaucoma, such as elevated intraocular pressure, extracellular matrix remodeling, and axon loss. This study validated the CTGF mouse model, focusing on mice aged 26 and 52 weeks. Key assessments included intraocular pressure measurements, electron microscopy and fluorescence microscopy. Various tools for objective image analysis were tested, including quantification of brightness in images acquired through fluorescence microscopy, measurement of changes in images acquired through electron microscopy and automated axon counting. We also applied Structured Illumination Microscopy for the first time on whole tissue slides of eyes of mice. A transfer of the transgenic construct onto mice of BALB/c and C57BL/6J strains was initiated. Significant differences emerged between transgenic and wild-type mice aged 26 and 52 weeks. The comparison of the brightness of images from fluorescence microscopy proved to be reliable, while Structured Illumination Microscopy protocols enhanced imaging capabilities. However, automated axon counting produced inconsistently high axon counts, indicating refinement is necessary before application. Validation in BALB/c and C57BL/6J strains was not finished by the end of the thesis. Overall, this thesis affirms the CTGF model's relevance for glaucoma research especially in older age groups and allows for the use of the model in long-term studies.

2 Introduction

2.1 Glaucoma and its Subtypes

Glaucoma is the main reason for irreversible blindness in humans (Flaxman et al., 2017; Resnikoff et al., 2008). It is defined as a chronic neuropathy of the optic nerve (ON), characterized by the progressive loss of retinal ganglion cell (RGC) axons, followed by the loss of the RGCs themselves (Foster et al., 2002). As RGCs are the cells transmitting visual information from the eye to the brain, this loss results in scotoma and can, even if treated, finally lead to blindness (Mokhles et al., 2017).

Treatment is limited to non-causative agents as the exact pathological mechanisms remain subject to current research (Kang & Tanna, 2021). Current pharmacological treatment includes topical application of carbonic anhydrase inhibitors, beta-blockers, and prostaglandins. If pharmacological treatment fails, laser trabeculoplasty and surgery such as trabeculectomy may also be used to slow disease progression (Weinreb, Aung, & Medeiros, 2014). Treatment may be extended by the use of rho kinase inhibitors (Freiberg et al., 2022) or nitric oxide donators (Mehran, Sinha, & Razeghinejad, 2020). They act by relaxing of trabecular meshwork (TM) cells and therefore decreasing the outflow resistance, similar to the effect of the release of nitric oxide from cells of Schlemm's Canal (SC) endothelium when they are subject to shear stress (Stamer et al., 2011).

The number of people suffering from glaucoma worldwide is estimated to have increased from 60.5 million patients in 2010 to 79.6 million patients in 2020 (Quigley & Broman, 2006). As the disease can remain asymptomatic until it is severe, the number of people affected is probably even higher (Leite, Sakata, & Medeiros, 2011). The disease has a strong impact on the quality of life worsening with its progression, but the effect can already be detected in early stages of glaucoma (Garg et al., 2018; Kumar et al., 2018).

There are several forms of glaucoma. One can differentiate between open-angle and closed-angle glaucoma; the iridocorneal angle (ICA) is decisive for this categorization. If it is closed, the diagnosis is the former, if it is open, the latter. Both can be primary

diseases; also, secondary forms of the disease occur, then mostly caused by therapy with corticosteroids, inflammation, or tumor (Lang, 2019). In primary open angle glaucoma (POAG), the form of the disease studied in this thesis, the ICA is ergo open. It is the type of the disease that is most frequent (Kwon et al., 2009), usually affecting both eyes in patients above the age of 40 (Quigley, 1996).

Pathological changes in glaucoma take place in the lamina cribrosa (LC) and the Optic Nerve head (ONH), where the RGC axons leave the eye and form the ON. The ON itself is surrounded by meninges as it is an excrescence of the diencephalon. The meninges merge into the sclera, where the LC is formed. This meshwork- or sieve-like structure supports the axons and protects them from mechanical stress (Figure 1). The LC is tasked with both providing structural support to the ONH by withstanding intraocular pressure (IOP)-induced forces while also allowing the axons to leave the eye. Due to this double function, it is a weak spot in an otherwise robust structure from a biomechanical point of view (Downs & Girkin, 2017).

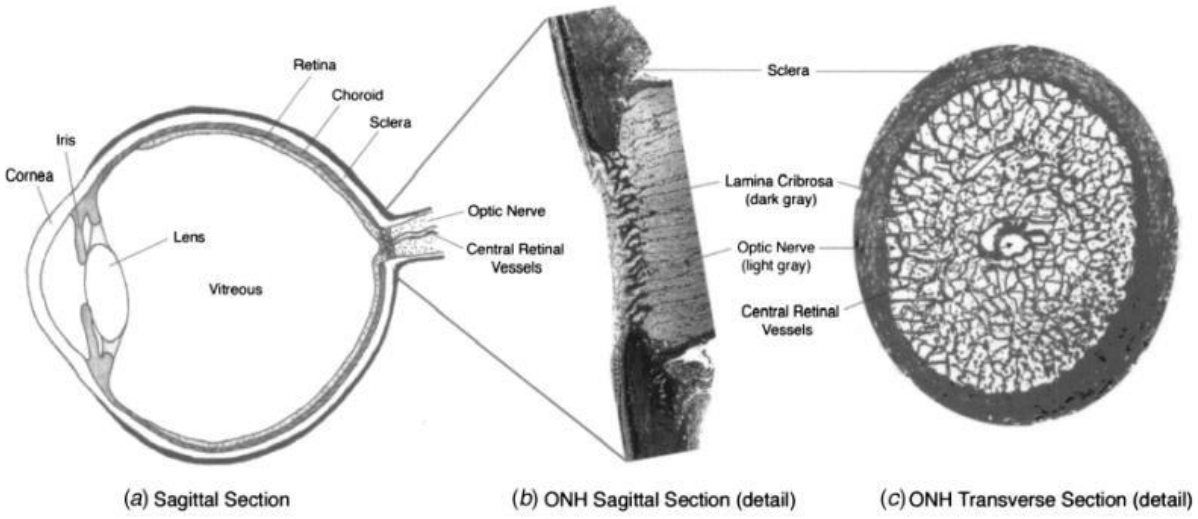

Figure 1 – Illustration of the LC (Downs, 2003). (a) Schematic sagittal section of the eye indicating the location of the LC. (b) Close-up view of the LC, showing portions of the sclera, RGC axons, and the LC itself. (c) Transverse section of the ONH, depicting central retinal vessels in addition to the structures shown in (b). The meshwork-like structure of the LC is clearly illustrated.

The cells forming the LC are mostly astrocytes and fibroblast-like LC cells. They synthetize extracellular matrix (ECM), for example collagens III and IV, fibronectin (FN) and Elastin (Hernandez, Igoe, & Neufeld, 1988).

In glaucoma, this region undergoes significant changes. Probably as a reaction to increased mechanical stress, the tissue stiffens, leading to decreased mechanical compliance (Albon et al., 2000). The stiffening of the surrounding tissue leads to difficulties in anterograde and retrograde transport of neurotrophic factors. The lack of neurotrophic factors can ultimately lead to RGC death (Pease et al., 2000; Quigley et al., 2000). The most visible consequence of RGC death is a phenomenon called *cupping*. Due to the loss of axons, the ONH shows a cup-shaped excavation (Figure 2).

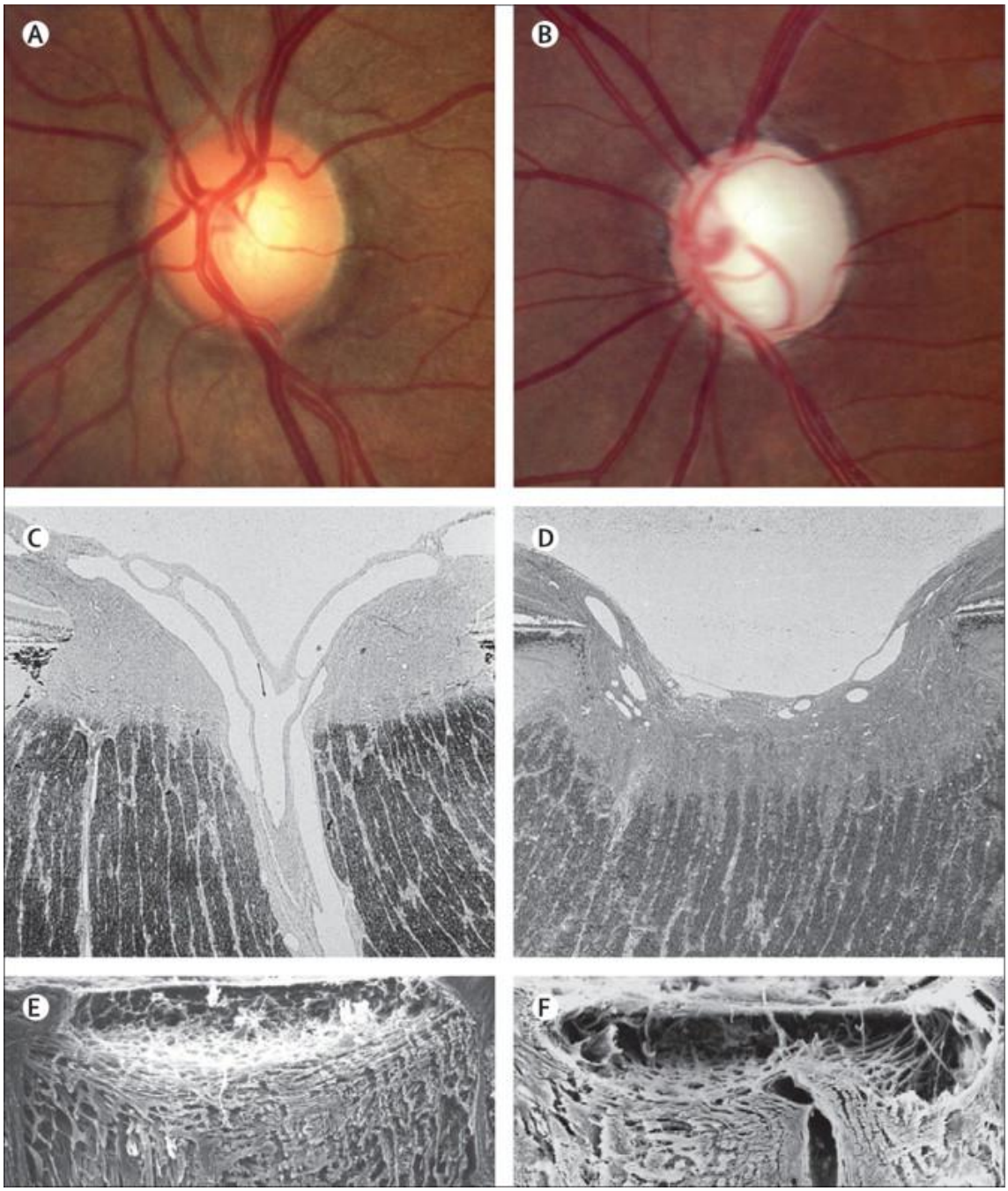

Figure 2 – ONH of healthy patients and those with glaucoma (Quigley, 2011). (A) and (B): The optic disc as seen in ophthalmoscopy. The central pale area (cup) enlarges from healthy (A) to glaucomatous (B) eyes. The surrounding orange rim of ON tissue also disappears. (C) and (D) show the typical histological findings: In the healthy state (C), there is more nerve tissue, especially at the rim, and the cup is not as deep as in (D), the glaucomatous state. In (E) and (F), only the connective tissue in the ONH region is visible. It is deepened in glaucoma (F) compared to a healthy subject (E). All these changes are the visible manifestations of excavation and cupping.

2.2 Primary Open Angle Glaucoma

Risk factors for developing glaucoma include age, genetic factors, ethnicity, thin corneas and abnormal ON anatomy (Quigley, 2011), with the main risk factor being IOP. IOP is directly linked to both presence and degree of ONH damage. The susceptibility

of each eye to glaucoma injury, however, is individually variable. Therefore, the relevant risk factor for glaucoma is the level of IOP (Quigley, 2015). This has been demonstrated across different stages and subtypes of the disease (Collaborative Normal-Tension Glaucoma Study Group, 1998; Garg et al., 2018; Gordon et al., 2002; Lichter et al., 2001; Miglior et al., 2005; The AGIS Investigators, 2000). Accordingly, the currently only modulatable causative factor in clinical treatment is IOP (Conlon, Saheb, & Ahmed, 2017; Mansouri et al., 2011).

In a healthy eye, IOP is maintained by a continuous production and outflow of aqueous humour (AH) (Tamm & Fuchshofer, 2007). Non-pathological values of IOP in humans vary between 10 and 21 mmHg, while in patients with Glaucoma, IOP can rise above 21 mmHg, with a lot of the glaucomatous damage probably depending on IOP variability (Musch et al., 2011). A normal IOP serves several functions, including the smooth coverage of the cornea, or maintaining a constant distance between cornea, lens and retina, among others (Lang, 2019) .

AH serves several functions apart from maintaining IOP; one of them is to nourish intraocular tissue, for example with oxygen, glucose, electrolytes and vitamin co-factors (Macknight et al., 2000), and it also removes cellular waste. In fact, AH takes over some functions usually executed by blood. It is present in parts of the eye where blood vessels would hinder proper vision – such as lens and cornea – because vessels are not transparent and would diffract light (Kiel, 2010; Weinreb et al., 2014).

AH production takes place in the non-pigmented epithelium of the ciliary body in the posterior eye chamber. It flows from there, passing iris and eye lens, to the anterior eye chamber. The majority of AH is drained at the ICA, mainly through TM into SC (Tamm, 2009). SC is connected to the episcleral vein system, through which the AH is finally drained. About 10 to 15 percent of the AH drains directly into the uveoscleral vein system (Lang, 2019). Following the latter pathway, AH flows across the base of the iris, passing the ciliary body through interstitial tissue into suprachoroidal space. Afterwards, it passes through sclera and perivascular spaces before being absorbed into the uveoscleral veins outside the eye (Bill & Phillips, 1971). The main outflow pathway is illustrated in Figure 3.

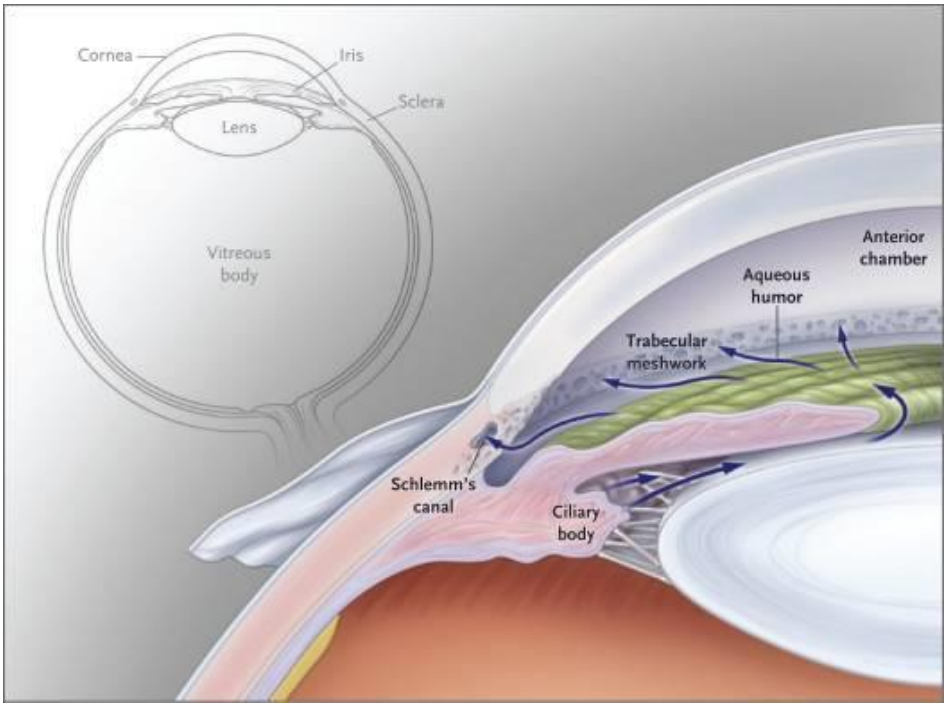

Figure 3 – Pathways of AH outflow (Kwon et al., 2009). Illustration of an anterior segment of the eye depicting the circulation of AH, with arrows indicating the direction of flow. Most of the AH flows from the ciliary body into the anterior eye chamber passing through the pupil. It then passes through the TM into SC and from there into the episcleral venous system. A smaller amount of AH leaves the eye directly through the face of the ciliary body, just below the TM.

Changes in IOP are mainly due to elevated outflow resistance, not to an elevated production of AH (Acott & Kelley, 2008; Johnson, 2006; Kwon et al., 2009). To understand the obstacles to AH outflow better, it makes sense to take a closer look at the anatomy of the TM.

2.3 Trabecular Meshwork

The TM is divided into three regions: the uveal meshwork, the corneoscleral meshwork and the juxtacanalicular or cribriform region (JCT) (Acott et al., 1989; Rohen, Futa, & Lütjen-Drecoll, 1981). The uveal meshwork and the corneoscleral meshwork consist of three layers of connective tissue beams covered by TM cells that form irregular intratrabecular fenestrations (Lütjen-Drecoll, 1999; Lütjen-Drecoll, Futa, & Rohen, 1981; Tamm, 2009). These intratrabecular spaces become smaller the closer one comes to SC, so they are still bigger in the uveal than they are in the cornoscleral meshwork. These regions mainly serve to filtering cellular debris out of the AH (Abu-Hassan, Acott, & Kelley, 2014). The JCT is formed by two to five amorphous and discontinuous cell layers embedded in a loose connective tissue ECM. JCT is the thinnest part of the TM, measuring 2 to 20 µm. It is directly adjacent to the inner wall endothelium of SC and,

together with it, also referred to as the inner wall region (Johnson, 2006). This inner wall region appears to create nearly all of the resistance to AH outflow (Ethier, 2002; Johnson, 2006).

The inner wall endothelium of SC forms giant vacuoles in response to AH passing through, often associated with pores. Those pores are approximately 0.1 to 3 µm in diameter (Johnson, 2006), with an average diameter ranging from 0.40 µm to 0.67 µm (Braakman et al., 2014). These pores cannot exceed a certain size because they must facilitate AH outflow while also being sufficiently restrictive to preserve the blood-aqueous barrier and prevent blood and serum proteins from entering back into the eye (Braakman et al., 2015). The pores can be further differentiated into two subtypes: transcellular “I” pores that pass directly through cells of SC, and paracellular “B” pores that pass through the junction between neighbouring SC cells (Ethier et al., 1998).

The inner wall endothelium displays one of the highest hydraulic conductivities in the body (Johnson, 2006). Paradoxically, calculations showed that the inner wall endothelium generates no more than 10% of total trabecular outflow resistance (Bill & Svedbergh, 1972). Johnson et al. (1992) developed a so-called funnelling model to resolve this paradox by exploring synergistic models of outflow resistance generation, taking into account hydrodynamic interactions between different layers of tissue, which allows them to explain most of the generated outflow resistance.

There is an active debate and ongoing research concerning the role of the inner wall endothelium of SC and JCT regarding their importance for the generation of outflow resistance. Namely, contraction of the ciliary muscle widens the outflow pathways and increases AH outflow (Gong, Tripathi, & Tripathi, 1996). The TM is also able to regulate the size of the outflow pathways through which the AH can physiologically drain, as TM cells themselves have contractile properties, exhibiting smooth muscle cell-like characteristics (Iwamoto & Tamura, 1988). Thus, they can influence the geometry of the TM and increase outflow resistance by contraction (Tian et al., 2000; Wiederholt, Thieme, & Stumpff, 2000).

2.4 Transforming Growth Factor β

Transforming Growth Factor β (TGF-β) is a member of the TGF superfamily. Three forms of TGF have been described in humans so far: TGF-β1, TGF-β2 and TGF-β3 (Clark & Coker, 1998). TGFβ-2 is the predominant form in the human eye (Jampel et al., 1990). TGF-β2 is produced by epithelial cells of the ciliary body and the lens and secreted into the AH (Fuchshofer & Tamm, 2009). In the eye, TGF-β2 can play a beneficial role. It provides the eye with immune protection against intraocular inflammation and it is able to normalize the ECM environment in degenerative diseases (Dobolyi et al., 2012). It may also play a role in the protection of RGCs (Braunger et al., 2013).

However, in patients with POAG, TGF-β2 plays a key role in pathogenesis. Levels of TGF-β2 are elevated in AH (Agarwal, Daher, & Agarwal, 2015), in the ICA (Inatani et al., 2001) and in the ONH (Pena et al., 1998) and induce characteristic pathological changes. These are the induction of contraction in TM cells as well as changes in ECM in the TM. Cell contractility and the secretion and composition of ECM in the inner wall region are possibly regulating the outflow resistance.

These effects are also observable in tissues outside the eye. Treatment with TGF-β induces contraction via an activation of Ras homolog family member A (RhoA) in many cell types (Edlund et al., 2002), and TGF-β2 plays a role in many diseases that involve changes in ECM, like Loeys-Dietz syndrome (Loeys et al., 2006). Regarding the eye, treatment of TM cells *in vitro* with TGF-β2 increases the expression of FN (Welge-Lüssen, May, & Lütjen-Drecoll, 2000) and inhibits degradation of ECM via Plasminogen activator inhibitor-1 (Fuchshofer, Welge-Lüssen, & Lütjen-Drecoll, 2003). Treatment of astrocytes in the ONH with TGF-β2 elevates the expression of ECM proteins (Fuchshofer et al., 2005).

In many patients with POAG, the amount of ECM in the JCT is increased. More precisely, elevated amounts of fibrillary collagen (Rohen et al., 1993) and FN are present, one of the main composites of ECM in the TM (Babizhayev & Brodskaya, 1989). Perfusion of human eyes with matrix metalloproteinases (MMPs) that are able to degrade fibrillary collagen and FN was able to diminish the outflow resistance, accordingly (Bradley et al., 1998).

In addition, there is an increase in so called sheath-derived plaque material in the JCT region (Lütjen-Drecoll & Rohen, 2001). The name derives from its composition of mainly the sheaths of the elastic fibres which form the cribriform plexus underneath the endothelial lining of SC. Although there is a correlation between the amount of sheath-derived plaque material and axonal damage in glaucomatous eyes, no correlation with IOP could be found. This indicates that the sheath-derived plaque material is not causative of the increase in trabecular outflow resistance in POAG on its own (Gottanka et al., 1997).

In conclusion, elevated levels of TGF-β2 in the AH influence both cell contractility and ECM deposition in the TM via gene expression (Fuchshofer & Tamm, 2009).

2.5 Connective Tissue Growth Factor

Connective Tissue Growth Factor (CTGF) is a protein that is a downstream mediator of TGF-β2. It is a regulatory protein of the CCN superfamily; the acronym CCN is derived from the first three members of the family discovered, namely Cysteine-rich angiogenic inducer 61, CTGF and NOV, short for nephroblastoma overexpressed. CTGF is also known as CCN2.

Members of this superfamily are involved in intercellular signaling and multiple cellular processes, such as the regulation of cell migration (Igarashi et al., 1993) and cell cycle (Bradham et al., 1991) or production of ECM (Frazier et al., 1996), just to name some. CTGF shares its basic structure with all members of the CCN superfamily. It has four conserved, cysteine-rich domains and is composed of a sequence of 349 amino acids. CTGF itself is known to play a key role in many fibrotic diseases, such as liver cirrhosis, hypertrophic scars, diabetic nephropathy, atherosclerosis, cardiac disease, pulmonary hypertension, fibrosis and others (Shi-Wen, Leask, & Abraham, 2008). Several in-vitro studies have shown that CTGF is required for, or acts in synergy with TGF-β in the induction of pro-fibrotic genes (Abreu et al., 2002; Shi-Wen et al., 2008; Winter, Leoni, & Abraham, 2008). CTGF is present in the eye, namely the TM (Tomarev et al., 2003), and secreted into the AH (van Setten et al., 2002). The treatment of TM cells with TGF-β2 was shown to increase the expression of CTGF (Fuchshofer et al., 2005). This

reveals the function of CTGF as a downstream mediator (Grotendorst, Okochi, & Hayashi, 1996).

CTGF expression is primarily regulated at the level of transcription (Winter et al., 2008). Transcription of the CTGF gene is activated by the binding of TGF-β via a Smad protein to a certain nucleotide sequence, the so-called *response element* in the promoter region (Bartholin et al., 2007; Holmes et al., 2001). Also, amongst other factors, the Hypoxia inducible factor 1α (Fuchshofer & Tamm, 2009), oxygen radicals (Park et al., 2001), and mechanical stress (Chaqour, Yang, & Sha, 2006) regulate the expression of CTGF which may play a role in the development of POAG.

The same effect is not inducible by other growth factors, for example Fibroblast Growth Factor. An activation via the RhoA/Rho-associated protein kinase signaling pathway is subject to discussion (Heusinger-Ribeiro et al., 2001) – as described above, this is a pathway also activated in cells when they are treated with TGF-β. CTGF was shown to be a mediator for inducing FN in TGF-β2-treated cells (Fuchshofer et al., 2005).

Even though CTGF was initially named a growth factor on discovery (Bradham et al., 1991), it does behave like a matricellular protein. There is no unique receptor for CTGF. Instead, CTGF works through many mechanisms simultaneously. In addition, cytokine environment and cell genotype might all influence effects of CTGF themselves, which means it works in a context-dependent manner (Lipson et al., 2012).

CTGF interacts with a number of different molecules after its secretion from the cell, with each of these interactions being dependent on various of its four domains. It can interact with cytokines and growth factors such as TGFβ, as described above, but also insulin-like growth factor 1, bone morphogenetic protein 4, bone morphogenetic protein 7 and vascular endothelial growth factor (Hashimoto et al., 2002). It can also bind to cell surface receptors with other known ligands such as tropomyosin receptor kinase A (Wahab, Weston, & Mason, 2005), low density lipoprotein receptor-related protein 1, low density lipoprotein receptor-related protein 6 (Segarini et al., 2001) and several different integrins (Jedsadayanmata et al., 1999; Schober et al., 2002). CTGF has also been reported to interact with ECM proteins such as FN (Gao & Brigstock, 2004).

Transcription factors and signalling pathways that are directly stimulated by CTGF include p42/p44 mitogen-activated protein kinase, Akt or protein kinase B, c-Jun N-terminal kinases and the Smad pathways (Abraham, 2008). All of those mediate important functions. Direct activation of p42/44 mitogen-activated protein kinase is important in cell adhesion and ECM production (Chen, Chen, & Lau, 2001). The interaction with the Smad pathway was already described above.

In the present study, a well-established mouse model was used that shows many features comparable to POAG in humans: The βB1-CTGF mouse that seems to be a promising tool to analyse pathological mechanisms in POAG. The genetically modified mice show a lens-specific overexpression of CTGF leading to an increased IOP accompanied with a progressive loss of ON axons (Junglas et al., 2012). In a different study, also an apoptotic loss of RGCs could be detected in the same mouse model (Reinehr et al., 2019). The time course of progression in βB1-CTGF mice seems to be similar to the time course of POAG in humans.

In the mouse model, also other features of POAG can be observed. POAG is associated with reactive gliosis and reactive Müller glial cells (Hernandez, 2000; Pena et al., 1999). This is accompanied by an increased expression of GFAP in human eyes (Seitz, Ohlmann, & Tamm, 2013; Tezel & Wax, 2003). Both could also be shown in βB1-CTGF mice (Reinehr et al., 2019).

2.6 Study Objectives

The present study had two main objectives:

(A) To validate the present and widely used CTGF-animal-model in different conditions.
(B) To assess and test new methods of analyzing the findings, especially in microscopy.

Regarding (A), prior studies on the development of POAG and its effects relied on βB1-CTGF mice not older than 12 weeks. In humans, POAG is a disease of the older age (Tuck & Crick, 1998). Hence, there might be a possible effect of the age in mice as well that has not been examined yet. In addition, it is also possible that the strongest effects induced by the transgenic (tg) construct occur after the age of 12 weeks as it

might take more time for them to fully manifest. Plus, validating the model over a longer period of time might be beneficial in studying long-term interactions in a mouse model. This is why the present study investigates the changes in the eyes of 26 and 52 weeks old βB1-CTGF-mice.

In addition, all prior experiments were done using mice of the CD1 strain. Therefore, the aim of this study is to investigate a possible effect of the mouse strain on prior findings. By crossbreeding for 8 generations with mice of either the BALB/c or the C57BL/6J strain, the tg construct can be transferred into another strain. However, the breeding itself takes time, and the detailed analysis is extensive, hence it will be subject to another M.D. thesis and not be presented in this study.

As in prior studies, IOP measurements were performed in all groups of mice. The aim of the present thesis, however, was not only to consolidate existing knowledge about a well-known paradigm. The goal was to improve histological assessment of mice's eyes, as well, by applying several new techniques to microscopy images (objective B). Until now, the investigation of differences in between microscope pictures has mostly been based on experts' opinions. To cross-validate the findings, a method was developed to quantify fluorescence in microscope images. In addition, an automated axon-counting method (Zarei et al., 2016a, 2016b) was validated by comparing it to manual axon count. Furthermore, ECM in the ICA was quantified after assessing samples with electron microscopy (EM).

As to improve histological assessment of murine eyes more broadly and to open a way towards a different method of investigation of pores in the SC endothelium, Structured Illumination Microscopy (SIM) was applied onto several samples (Gustafsson, 2000; Gustafsson et al., 2008; Heintzmann & Huser, 2017). SIM has previously been applied to retinal cells (Ach et al., 2012), but not on whole tissue slides. The goal was to establish this method for future application.

3 Materials and Methods

3.1 Materials

3.1.1 Reagents

Designation	Source of supply
1,4-Diazabicyclo(2.2.2)octan (DABCO)	Roth, Karlsruhe, Germany
2 N hydrochloric acid (HCl)	Merck, Darmstadt, Germany
4′,6-Diamidin-2-phenylindol (DAPI)	Sigma-Aldrich, Taufkirchen, Germany
Acetone	Merck, Darmstadt, Germany
Agarose	Biozym Scientific, Oldendorf, Germany
Ammonium Sulfate ($(NH_4)_2SO_4$)	Roth, Karlsruhe, Germany
Borate (Sodiumtetraborate)	AppliChem, Darmstadt, Germany
Bovine Serum Albumin (BSA)	Roth, Karlsruhe, Germany
Cacodylate acid	Merck, Darmstadt, Germany
Cold water fish gelatin (CWFG)	Aurion, Wageningen, The Netherlands
Cresol Red	Sigma-Aldrich, Taufkirchen, Germany
DakoCytomation fluorescent mounting medium	Sigma-Aldrich, Taufkirchen, Germany
Deoxynucleoside-Triphosphates (dNTPs)	Qiagen, Hilden, Germany
Ethylenediamine-tetraacetic acid (EDTA)	PAA Laboratories, Pasching, Austria
Epon	Serva, Heidelberg, Germany
Ethanol 100%	Roth, Karlsruhe, Germany
Ethidium bromide	Serva, Heidelberg, Germany
Gelatin	Sigma-Aldrich, Taufkirchen, Germany
Gene ruler DNA standard	New England Biolabs, Frankfurt, Germany
Glutaraldehyde, 2,5% in water	Serva, Heidelberg, Germany
Glycerine	Roth, Karlsruhe, Germany
Heparin	B. Braun Melsungen, Melsungen, Germany
Isoflurane	Ecuphar GmbH, Greifswald, Germany
Isopropanol	Fluka Chemie, Buchs, Switzerland
Ketamine	beta-pharm, Vechta, Germany
Lead citrate	Leica, Wetzlar, Germany
Magnesium dichloride $MgCl_2$ (25 and 50 mM)	New England Biolabs, Frankfurt, Germany
Methylene blue/Azure II	Roth, Karlsruhe, Germany
Mowiol Fluorescent Mounting Medium	Vector Laboratories, Newark, CA, USA
Osmium tetroxide	Merck, Darmstadt, Germany
Paraffin wax	Engelbrecht, Munich, Germany
Paraformaldehyde (PFA)	Sigma-Aldrich, Taufkirchen, Germany
Poly-L-lysine	Merck, Darmstadt, Germany
Potassium dihydrogen phosphate (KH_2PO_4)	Roth, Karlsruhe, Germany

Potassium ferrocyanide	Merck, Darmstadt, Germany
Potassium chloride (KCl)	Merck, Darmstadt, Germany
Purified water (dH_2O)	Self-purification
Sodium chloride (NaCl)	Roth, Karlsruhe, Germany
Sodium dihydrogen phosphate (NaH_2PO_4)	Merck, Darmstadt, Germany
Sodium phosphate dibasic (Na_2HPO_4)	Merck, Darmstadt, Germany
Sucrose	Roth, Karlsruhe, Germany
Tergitol	Sigma-Aldrich, Taufkirchen, Germany
Tissue-Tek optimal cooling temperature compound	Sakura Finetek Europe, Zoeterwoude, The Netherlands
Tris HCl	Roth, Karlsruhe, Germany
Triton	Roth, Karlsruhe, Germany
Tween 20	Roth, Karlsruhe, Germany
Uranyl acetate	Serva, Heidelberg, Germany
Xylazine	Serumwerk Bernburg, Bernburg, Germany
Xylene	Roth, Karlsruhe, Germany

Table 1 – Reagents

3.1.2 Enzymes

Designation	Source of supply
Proteinase K	Roth, Karlsruhe, Germany
Taq DNA Polymerase	Self-purification

Table 2 – Enzymes

3.1.3 Oligonucleotide Primers

Primer	Species	Orientation	Sequence 5' to 3'
βB1	*Mus musculus*	forward	gtgcgggacagaaacctg
		reverse	ggaagtgccagctcatcagt
SV40	*Mus musculus*	forward	gcgaaggaaccttacttctgtggtg
		reverse	gtccttggggtcttctacctttctc

Table 3 – Oligonucleotide Primers

All primers were purchased from Invitrogen, Karlsruhe, Germany.

3.1.4 Antibodies

Targeting protein	Primary antibody	Source of supply
α-Smooth-Muscle-Actin (α-SMA)	Anti-α-SMA Rabbit IgG	Sigma-Aldrich, Taufkirchen, Germany
CD31	Anti-CD31/PECAM-1 Goat IgG	R&D Systems, Minneapolis, MN, USA
FN	Anti-FN Rabbit IgG	Dako, Hamburg, Germany

Table 4 – Primary Antibodies

Secondary antibody	Source of supply
AffiniPure Donkey Anti-Rabbit Cy™3-conjugated	Dianova, Hamburg, Germany
Goat Anti-Rabbit Biotinylated Antibody	Vector Laboratories, Newark, CA, USA
Donkey Anti-Goat Biotinylated Antibody	Dianova, Hamburg, Germany
Streptavidin Alexa Fluor 488 conjugated	MoBiTec Molecular Probes, Göttingen

Table 5 – Secondary Antibodies

3.1.5 Chemical Composition of Solvents and Buffers

Solvent/Buffer	Composition
0.1 M Cacodylate Buffer	10.7 g cacodylate acid in 500 ml dH_2O
0.1 M Phosphate Buffer (PB), pH 7.4	100 ml 0.2 M Na_2HPO_4 x $2H_2O$ + 0.2 M NaH_2PO_4 x H_2O, pH 7.4 dilute with dH_2O to 0.1 M
1.0 M Tris-HCl, pH 6.8	121.14 g Tris ad 1 l dH_2O
10x Buffer Q	1 ml Tris (1 M) 1 ml $(NH_4)_2SO_4$ (1 M) 0.075 ml $MgCl_2$ (2 M) 2 ml KCl (1 M) ad 50 ml dH_2O
10x Phosphate-Buffered Saline (PBS), pH 7.4	80 g NaCl 2 g KCl 4.4 g Na_2HPO_4 2.4 g KH_2PO_4 ad 1 l dH_2O, autoclave
5x PCR Buffer	34.5 ml glycerol tip of a spatula cresol red (1 mM) ad 50 ml dH_2O

Karnovsky's Solution	2.5% glutaraldehyde 2.5% PFA in 0.1 M cacodylate buffer
Mouse Tail Buffer	3.74 g KCl 0.51 g $MgCl_2$ x $6H_2O$ 0.1 g gelatin 4.5 ml Tergitol 4.5 ml Tween 20 10 ml Tris-HCl (1 M) ad 1 l dH_2O
Mowiol with DAPI	2.4 g Mowiol 6.0 g Glycerine 6.0 ml dH_2O 12.0 ml 0.2 M Tris-HCl (pH 8.5) 25.0 ml DABCO per 1.0 ml DAPI (1:10)
Tris-Borate-EDTA (TBE) Buffer	108 g Tris 55 g borate 40 ml EDTA (0.5 M), pH 8.0 ad 1l dH_2O

Table 6 – Chemical Composition of Solvents and Buffers

3.1.6 Laboratory Equipment

Designation	Source of supply
60x 1.42 NA oil-immersion objective	Olympus, Tokyo, Japan
Centrifuges 5415D, 5415R, 5804R, 5810R	Eppendorf, Hamburg, Germany
DeltaVision OMX V4 Blaze imaging system	GE Healthcare, Issaquah, WA, USA
Ear punching device	Fine Science Tools, Heidelberg, Germany
Embedder	EM TP Leica, Wetzlar, Germany
Icare tonometer LAB Original Icare tonometer probes	Icare Finland Oy, Espoo, Finland
Isoflurane evaporator	Self-provided
Julabo SW20 water bath	Julabo Labortechnik GmbH, Seelbach, Germany
LAS-3000 Intelligent Dark Box	Fujifilm, Düsseldorf, Germany
Mastercycler Gradient Personal (thermocycler)	Eppendorf, Hamburg, Germany
Memmert water bath	Memmert, Schwabach, Germany
Microm HM 500 OM Kryostat	Microm International, Walldorf, Germany
Microscope Axio Imager Z1	Zeiss, Göttingen, Germany
MilliQ Plus PF water purification system	Millipore Corporation, Billerica, MA, USA
PowerShot G5 Digital Camera	Canon, Krefeld, Germany
Research pipets	Eppendorf, Hamburg, Germany

Surgical instruments	Fine Science Tools, Heidelberg, Germany
Systec V75 Autoclave	Systec, Wettenburg, Germany
Thermal Mixer Comfort	Eppendorf, Hamburg, Germany
TonoLab tonometer TV02	Icare Finland Oy, Espoo, Finland
Ultracut E-Ultramicrotom	Reichert-Jung, Kirchseeon, Germany
Ultra violet light screen	Bachhofer Laboratoriumsgeräte, Reutlingen, Germany
Vortex-Genie 2	Scientific Industries, New York, NY, USA
Zeiss Libra transmission electron microscope	Carl Zeiss, Göttingen, Germany

Table 7 – Laboratory Equipment

3.1.7 Consumables

Designation	Source of supply
Falcon Reaction Tubes 15 ml, 50 ml	Sarstedt, Nümbrecht, Germany
Biosphere Filter Tips	Sarstedt, Nümbrecht, Germany
Cover slips, 24 x 60mm	Menzel-Gläser, Braunschweig, Germany
Glassware	Schott, Roth, VWR, Germany
Liquid Blocker PAP-Pen	SCI Science Services, Munich, Germany
Pasteur pipettes	Brand, Wertheim, Germany
Personna Razor Blades	American Safety Razor Company, Verona, VA, USA
Pipette tips	Sarstedt, Nümbrecht, Germany
Powder-free Sempercare gloves	Sempermed, Vienna, Austria
Sterican injection cannula	B. Braun, Wertheim, Germany
SuperFrost Plus object slides	Menzel-Gläser, Braunschweig, Germany
Syringes	Henry Schein, New York, NY, USA

Table 8 – Consumables

3.2 Animal Models

3.2.1 βB1-CTGF Mice

For in vivo experiments, mice (*Mus musculus*) aged 4, 8, and 12 weeks and mice aged 26 and 52 weeks were used. All animals were part of a tg mouse line. Tg animals carried a βB1-CTGF genetic construct that leads to a lens-specific overexpression of CTGF. These tg βB1-CTGF mice were generated in Prof. Dr. R. Fuchshofer's team by adenoviral gene transfer (Junglas et al., 2012). Their wild type (WT) littermates were used as controls.

The mouse model mimics the pathogenesis of POAG. As CTGF is a downstream mediator of TGFβ2, this overexpression leads to changes in IOP. In this animal model, murine CTGF complementary deoxyribonucleic acid (cDNA) is controlled via the chicken-βB1 promotor. An additional SV40 poly(A) sequence from the SV40 small T-intron is located at the end of the construct. The stability of CTGF messenger ribonucleic acid (mRNA) is ensured by transcription of the polyadenylation signal. The construct is illustrated in Figure 4.

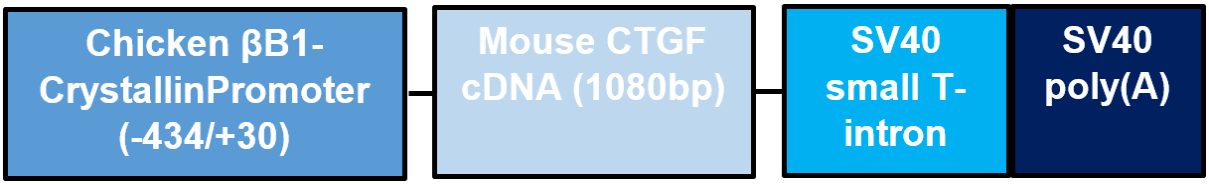

Figure 4 – Genetic construct of βB1-CTGF mice (kindly provided by Prof. Dr. R. Fuchshofer, modified)

All mice used in this study were bred in the animal facility of Prof. Dr. E. Tamm, Institute for Human Anatomy and Embryology, University of Regensburg. Both male and female mice were included. All animals were kept according to the Association for Research in Vision and Ophthalmology Statement for the Use of Animals in Ophthalmic and Vision Research, at temperatures of 23 ± 2 °C and a humidity of 55 ± 5%, food and water *ad libitum*. Light-dark cycles were set to 12 h.

3.2.2 CD1 βB1-CTGF Mice

Mice 26 and 52 weeks old belonged to the βB1-CTGF line with a CD1 background. These mice were shown to develop pathological changes typical for POAG even at younger age (Junglas et al., 2012).

3.2.3 BALB/c or C57BL/6 βB1-CTGF Mice

In order to study the tg construct in a different genetic background, an interbreeding between mice of the βB1-CTGF line with a CD1 background and WT mice of a BALB/c or C57BL/6 background was initiated. For the first generation, a βB1-CTGF line mouse with CD1 background was mated with either a WT BALB/c or a C57BL/6 mouse. Tg mice from these breeds were mated with a WT BALB/c or C57BL/6 mouse once again, as in the previous generation. By repeating this procedure eight times, it is possible to obtain mice of a pure BALB/c or C57BL/6J background with the tg CTGF overexpression. The scheme is illustrated for C57BL/6J mice in Figure 5.

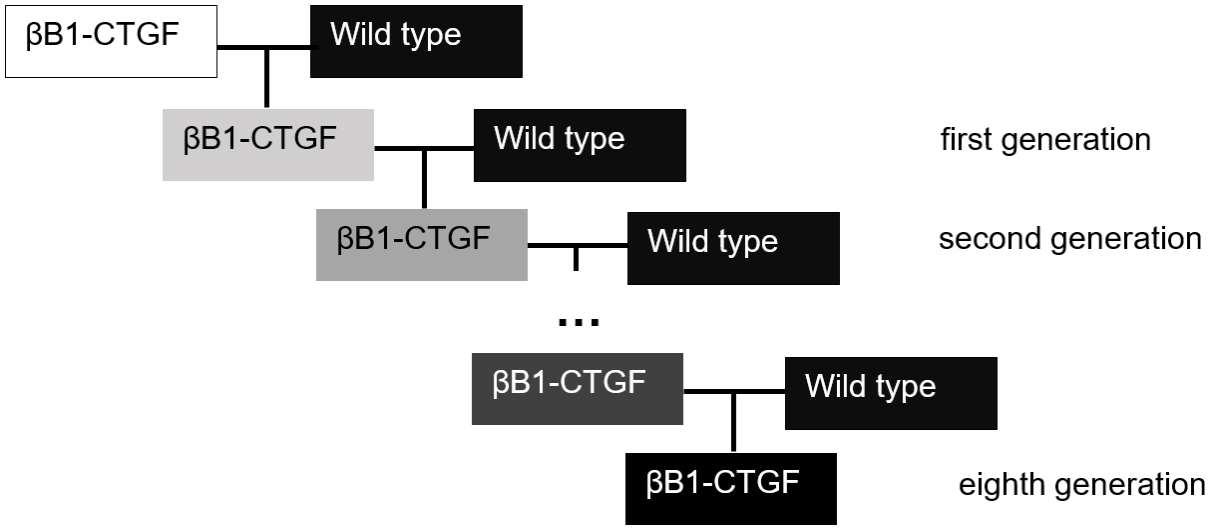

Figure 5 – Scheme of genetic modification via crossbreeding for CD1 and C57BL/6J mice, black background indicating C57BL/6J background, white background indicating CD1 background, and scales of grey intermediate generations.

3.3 Biomolecular Techniques

3.3.1 Isolation of Mouse DNA

In order to obtain mouse deoxyribonucleic acid (DNA) for genotyping, tissue samples obtained by ear punching were used. To make the DNA accessible for further investigation, tissue was lysed at 55 °C in 200 µl mouse tail buffer and with 5 µl proteinase K overnight. The next day, the proteinase was inactivated at 95 °C for 10 min. The lysate was then put into a centrifuge, running at 16.000 g for 10 minutes to separate the supernatant liquor containing the DNA from the remaining non-lysed tissue. The DNA was then stored at 4 °C.

3.3.2 Genotyping

PCR is a technique used to amplify a specific sequence of DNA. It is characterized by three main steps – denaturation, annealing and extension. These steps can be controlled by warming and cooling the samples to different temperatures in a thermocycler. During the denaturation step, the DNA is melted into two accessible single strands. During the annealing step, primers connect to the DNA that is meant to be amplified. During elongation, DNA polymerase synthesizes a new DNA strand using the dNTPs

from the solution. By repeating this procedure several times, the amount of DNA produced can be amplified exponentially. The obtained DNA can be detected by agarose gel electrophoresis.

3.3.2.1 βB1- and SV40-PCR

Two separate PCR assays were used to determine the genotype of the mice. Based on the genetic construct explained above, both the chicken βB1-crystallin promoter and the SV40-polyA-tail serve as markers to determine whether a mouse is tg. Table 9 shows the reagents used for each PCR, scaled to one 15 µl probe. Table 3 gives the exact primer sequences.

	Mastermix βB1-PCR	**Mastermix SV40-PCR**
dH_2O	11.15 µl	7.00 µl
10x Buffer Q	1.50 µl	1.50 µl
5x Buffer PCR	-	3.00 µl
1:10 forward primer	0.30 µl	0.30 µl
1:10 reverse primer	0.30 µl	0.30 µl
10 mM dNTPs	0.30 µl	0.30 µl
Taq DNA polymerase	0.30 µl	0.30 µl
25 mM $MgCl_2$	-	0.30 µl

Table 9 – Mastermixes Used for Each PCR, Scaled to One 15 µl Probe

DNA from a tg mouse was used as a positive control. As negative controls, dH_2O instead of DNA was added. Thermal cycling conditions for both PCRs are listed in Table 10.

βB1-PCR				**SV40-PCR**		
Step	**Temperature**	**Time**	**Cycles**	**Temperature**	**Time**	**Cycles**
1	96° C	02:00		94° C	02:00	
2	94° C	00:30	32x	94° C	00:30	35x
3	65° C	00:30		55° C	00:30	
4	72° C	00:20		72° C	00:45	
5	72° C	02:00		72° C	05:00	

Table 10 – Cycler Programs for βB1- and SV40-PCR, times are given in minutes.

3.3.3 Agarose Gel Electrophoresis

DNA amplified by PCR can be detected via agarose gel electrophoresis. Micropores in the gel separate DNA fragments by size when an electric current is applied - longer fragments migrate more slowly through the gel matrix. Ethidium bromide intercalates with DNA and fluoresces under ultraviolet light, allowing visualization of the DNA bands.

The 1 %-agarose gel was produced by boiling 1 mg of agarose in 100 ml of TBE buffer in a microwave. After the solution cooled, 3 µl of ethidium bromide was added. The gel was poured into a casting tray with a comb to create sample wells, and placed in an electrophoresis chamber filled with TBE buffer after polymerization. 5x PCR Buffer was added by pipetting into the βB1-PCR fluid. Every gel was loaded with 2 µl of 100 bp Gene ruler DNA standard. 12 µl of βB1- or SV40-PCR products were loaded into the wells. As to separate the different DNA bands, direct current with 130 V voltage was applied for 40 minutes. DNA bands were visualized under UV light and photographed. A 360 bp band indicated a tg genotype in both PCRs, while WT littermates showed no bands.

3.4 In Vivo Experiments

3.4.1 Intraocular Pressure Measurements

Changes in IOP are a sign of the development of a POAG. Mice of the CD1 βB1-CTGF strain were shown to develop these changes due to their overexpression of CTGF, resulting in changes in the TM and elevated IOP (Junglas et al., 2012). Since increased IOP strongly correlates with axonal loss in this model, IOP was measured in both tg and WT mice.

Mice received initial anesthesia with isoflurane until immobility was achieved. Then they were placed in prone position in front of an isoflurane evaporator delivering a constant flow of isoflurane mixed with air for several minutes prior to the beginning of the measurements. The time in front of the evaporator was kept consistent across all animals to minimize variability. The depth of anesthesia was controlled by monitoring respiratory patterns to ensure regular, deep breathing indicative of appropriate anesthesia depth.

IOP was measured using a TonoLab tonometer TV02 equipped with original Icare tonometer probes, always starting with the right eye. Measurements were performed by an investigator blinded to the genotype of the animals. The device automatically processes five measurements into one point of data, also checking the standard deviation (SD) of the measurements. Only measurements with low SD, as indicated by the device, were included in the analysis. Others were excluded. A minimum of five averaged measurements per eye was recorded.

3.4.2 Transcardial Perfusion

In order to gain eyes for histological investigation, mice had to be sacrificed. Preserving the tissue for microscopy and removing autofluorescent erythrocytes from the blood vessels was realized by transcardial perfusion with fixating substances. Mice were initially anesthetized with isoflurane in an induction chamber containing a mixture of isoflurane and air until their muscle tone decreased to complete relaxation. They were weighed and got an intraperitoneal injection of 0.02 mg xylazine 2% per gram bodyweight (g b. wt.) and 0.3 mg ketamine 10% per g b. wt. Mice were then regularly checked for defensive reflexes by squeezing their intermetacarpal region. Once they showed no reaction to this pain stimulus, the abdominal cavity, diaphragm, and thoracic cavity were opened. The beating heart was carefully held with a forceps and the right atrial auricle was cut open.

By injection into the left ventricle, the mice were perfused with 5 ml of a 1:1000 dilution of heparin in NaCl. Successful perfusion could be visually controlled by a change in the color of the liver from deep to light red. After this, the right eye was enucleated. By removing the NaCl tube and replacing it with a Karnovsky's solution tube in the same injection channel, mice were perfused with Karnovsky's solution afterwards. Successful performance of this procedure could be controlled by the strong contraction of muscles once the Karnovsky's solution was spread in the body. Then the left eye was enucleated. For mice aged 52 weeks, both eyes were obtained after a single perfusion with Karnovsky's solution.

3.5 Histological Techniques

3.5.1 Cryo- and Paraffin-Embedding

In order to prepare eyes for histological examination and immunofluorescence staining, they had to be embedded either in paraffin wax or frozen in Tissue-Tek. After storing the freshly acquired tissue in 5% PFA solution to keep it from desiccation, the cornea of the eyes that were meant to be frozen was cut open 1 hour after the eye enucleation to facilitate the diffusion process. It is necessary to dehydrate the eyes for cryo-processing; if the eyes were frozen containing too much moisture, the emerging ice crystals could destroy the surrounding tissue. This was realized by a graded series of sucrose immersion (10% sucrose the following morning, 20% sucrose overnight, and 30% sucrose for 24 hours two days after the enucleation). The eyes were embedded in Tissue-Tek and stored at -20 °C. The frozen blocks were cut 12 µm thin on a cryostat.

The eyes envisaged for paraffin embedding were also stored in 5% PFA solution for at least four hours at 4˚C. The next morning, they were washed three times for 20 minutes in 0.1 M PB, then inserted in 50% and 70% isopropanol for one hour each at room temperature (RT). Prior to embedding, they were stored in 70% isopropanol at RT.

3.5.2 Paraffin Sectioning and Mounting for Conventional Fluorescence Microscopy

Paraffin blocks were cut 8 µm thin on a microtome for regular immunohistochemical assessment and mounted afterwards.

3.5.3 Paraffin Sectioning and Mounting for Structured Illumination Microscopy

As to make them available for SIM imaging, paraffin blocks had to be cut into 3-µm-thin sections. This is not possible using a standard microtome knife, as the slides tend to fall apart during cutting at this thickness. A standard procedure to ensure the stability of paraffin sections is cooling them in a freezer prior to cutting (Ross & Pawlina, 2015). This actually changes the thickness of the paraffin to about 5 µm after reaching RT again, though, which might be linked to its chemical properties and changing density in different temperatures (Kaye & Laby, 1995; McKetta & Weismantel, 1999). Cooling is therefore not a solution to achieve very thin paraffin slides.

Therefore, they were cut with glass knives. A small water basin was attached directly to the knife to facilitate the acquisition of the cut slides and keep them from rupturing as it is usually done for ultra-thin sectioning (Suvarna, Layton, & Bancroft, 2019). Preparing slides for SIM microscopy requires mounting on a cover glass after cutting. In order to make the tissue stick to the unfrosted cover glass, they required preparation with poly-L-lysine that is also used to attach cells to surfaces for examination (Mazia, Schatten, & Sale, 1975). No. 1.5 cover glasses were washed with 100% ethanol and dH_2O to remove any possible dirt from them, then dried. Per cover glass, 120 µl of 0.1% poly-L-lysin solution were applied for five minutes, followed by four washing steps (3x with dH_2O, followed by glutaraldehyde). Cover glasses were then dried and could be used for mounting afterward. Mounting on usual frosted microscope slides also works if the samples are dried with a weight placed on them after staining to diminish the distance between cover glass and sample to the absolute minimum.

3.5.4 Epon-Embedding and Semi-Thin Sectioning

For accessing both ONs and ICAs in high resolution, left eyes were prepared for semi-thin and ultrathin sectioning. They were fixed in Karnovsky's solution. The cornea was cut open 1 hour after enucleation to facilitate the diffusion process. Connective tissue and muscles were removed from the eyeball to prevent them from disturbing the semi- and ultrathin sectioning.

After 24 hours, eyes were washed in 0.1 M cacodylate buffer for 30 minutes four times. Postfixation was performed using 1% osmium tetroxide and 0.8% potassium ferrocyanide in 0.1 M cacodylate buffer at 4 °C for 3 hours and 30 minutes. Eyes were dehydrated in a graded series of ethanol and embedded in Epon using a dilution of Epon in acetone. 1-µm-thick semi-thin sections were mounted on uncoated glass slides, followed by staining with methylene blue/azure II solution. Ultrathin sections were placed on uncoated copper grids and stained with uranyl acetate and lead citrate.

3.5.5 Immunohistochemical Staining

3.5.5.1 Slides from Paraffin Wax Embedded Eyes for Conventional Fluorescence Microscopy

Paraffin wax was removed in xylene and a graded series of isopropanol. Slides were placed into 0.05 M TRIS-HCl for five minutes, followed by the application of proteinase K (100 µl in 57 ml 0.05 M TRIS-HCl) for the same amount of time. Slides were washed with dH_2O once for five minutes, then incubated with 2N HCl for thirty minutes. Washing with dH_2O for five minutes was repeated.

Then, slides were put into 0.1 M PB and blocked with 2% BSA, 0.2% CWFG, 0.1% Triton in 0.1 M PB for 1 hour at RT on a teeterboard. Afterwards, they were incubated with either anti-FN rabbit immune globulin G (IgG) (1:250) or anti-α-SMA rabbit IgG (1:1000) at 4 °C overnight. The next day, slides were washed three times with 0.1 M PB for five minutes.

Slides for FN staining were incubated with biotinylated anti-rabbit antibodies (1:500) for one hour. The remaining slides were kept wet with 0.1 M PB. The washing process with 0.1 M PB was repeated another three times for all slides that were incubated with antibodies. Slides with FN staining were then incubated with Streptavidin Alexa-488 conjugated IgG (1:500) for 1 hour in the dark on a teeterboard. α-SMA staining was finished by application of CY3-conjugated anti-rabbit IgG antibodies (1:2000), also in the dark on a teeterboard. After washing three times for five minutes in the dark with 0.1 M PB and with dH_2O once, the slides were mounted using DakoCytomation fluorescent mounting medium with DAPI (1:10). The slides were dried in the dark overnight and stored at 4 °C prior to microscopy.

As a negative control for unspecific binding of secondary antibodies, slides were processed the same apart from incubation with 2% BSA, 0.2% CWFG, and 0.1% Triton in 0.1 M PB diluted 1:10 in 0.1 M PB instead of primary antibodies.

3.5.5.2 Slides from Paraffin Wax Embedded Eyes for Structured Illumination Microscopy

Slides for SIM were initially treated the same as described above, only blocking was performed with 5% BSA in 10x PBS solution instead of 2% BSA, 0.2% CWFG, and

0.1% Triton in 0.1 M PB. Anti-CD31 goat IgG was then applied in a 1:100 dilution in 0.5% BSA (from 1:10 dilution of 5% BSA in 10x PBS) overnight.

The next day, the samples were washed three times with 10x PBS, afterwards incubated with biotinylated anti-goat IgG in a 1:500 dilution in 0.5% BSA for 1 hour on a teeterboard, followed by washing with 10x PBS for five minutes three times. Finally, Streptavidin Alexa-488-conjugated IgG was applied in a 1:1000 dilution in 0.5% BSA in the dark on a teeterboard. To avoid artifacts, those slides cannot be mounted using DakoCytomation fluorescent mounting medium with DAPI and must instead be incubated with DAPI in a separate step. They were washed twice with 10x PBS for five minutes, followed by incubation with DAPI (1:200 in 10x PBS) for 30 minutes. A final 5-minute washing step with dH_2O was required to rule out possible precipitation of salts in the 10x PBS when getting in touch with the Mowiol mounting medium before finally mounting.

As a negative control for unspecific binding of secondary antibodies, slides were processed the same apart from incubation with 0.5% BSA in 10x PBS instead of primary antibodies.

3.5.5.3 Slides from Cryo-Embedded Eyes for Conventional Fluorescence Microscopy

Cryo-fixed eyes were put into 0.1 M PB and blocked with 2% BSA, 0.2% CWFG, 0.1% Triton in 0.1 M PB for 1 hour at RT on a teeterboard. Afterwards, they were incubated with either anti-FN rabbit IgG (1:250) or anti-α-SMA rabbit IgG (1:1000) at 4 °C overnight. The next day, slides were washed three times with 0.1 M PB for five minutes. Slides for FN staining were incubated with biotinylated anti-rabbit antibodies (1:500) for one hour. The remaining slides were kept wet with 0.1 M PB. The washing process with 0.1 M PB was repeated another three times for all slides that were incubated with antibodies.

Slides with FN staining were then incubated with Streptavidin Alexa-488 conjugated IgG (1:400) for 1 hour in the dark on a teeterboard. α-SMA staining was finished by application of CY3-conjugated anti-rabbit IgG antibodies (1:2000), also in the dark on a teeterboard. After washing three times for five minutes in the dark with 0.1 M PB and with dH_2O once, the slides were mounted using DakoCytomation fluorescent mounting

medium with DAPI 1:10. The slides were dried in the dark overnight and stored at 4 °C prior to microscopy.

As a negative control for unspecific binding of secondary antibodies, slides were processed the same apart from incubation with 2% BSA, 0.2% CWFG, and 0.1% Triton in 0.1 M PB diluted 1:10 in 0.1 M PB instead of primary antibodies.

3.6 Microscopy

3.6.1 Fluorescence Microscopy

Immunohistochemical stainings and semi-thin sections were examined using an Axio Imager Z1 microscope. Ultrathin slides were examined on a Zeiss Libra transmission electron microscope.

3.6.2 Objective Analysis of Microscope Pictures

The aim of the present study was to quantify the difference in immunohistochemical staining between different slides, avoiding reliance solely on the potentially subjective interpretation and comparison of images. The intensity of fluorescence was therefore quantified by measuring the brightness of the area of interest. All of the measurements and procedures that are described in the following paragraphs were done using ImageJ Version 1.51f (Schindelin et al., 2012) with some of the calculations being done in Microsoft Excel 2016 (Microsoft Corporation, Redmond, WA, USA).

The underlying idea is to replicate the evaluation process an experienced expert would follow when assessing a group of images, but in a more quantifiable manner. It is assumed that the greater the amount of target proteins on the slides, the more primary and secondary antibodies will bind. Examination under a fluorescence microscope and activation of the fluorophores will therefore lead to a more elevated brightness that should be directly related to the amount of the target protein present within the sample. This is essentially the same principle an expert applies when comparing microscope images – except that the expert relies on visual perception rather than numerical data to detect brightness differences.

The first step was to eliminate any signal from the analysis that was not emitted from the target fluorophores. Therefore, the required color channel had to be selected (e.g., green for Alexa 488-labeled samples); this channel was then exported as a tiff-format file in greyscale. In the selected greyscale picture, the area of the TM and SC was defined as the area of interest. Pictures that did not allow a definitive localization of any of these anatomical structures were excluded from the analysis.

The next challenge was to remove any noise from the analysis. Noise refers to pixels whose brightness is above 0 – above complete black, so to speak – but is not generated by fluorophore fluorescence, but rather by slight autofluorescence, for example. In general, there are two possible ways to address this: one is to subtract the mean brightness of a negative control from all the obtained data. The other is to define a threshold based on a mathematical method. The latter option seemed preferable as it can be adapted to every image individually. If there is a small aggregation of fluorophores in a picture, for example, the effect of this distorting object will only be partially reduced by subtraction of negative control values, but can be fully eliminated by setting the appropriate threshold.

To select the correct thresholding method from the 16 available options in ImageJ, images were assessed using Auto Threshold Plugin Version 1.16.5. A representative result is shown in Figure 6, pixels included in the threshold are shown in white, others in black. The thresholds shown in the top left, top right, and third row, third from left (marked in red), demonstrate a continuous inclusion of pixels surrounding SC, but also exclude unnecessary areas that light up under other thresholding settings. As SC and TM are the areas of interest, these three threshold settings were examined further by evaluating the mean luminosity using a simple histogram for each thresholded image in ImageJ. The threshold with the lowest luminosity was selected as this indicates the lowest level of background noise.

After comparing results for all images to be analyzed as described above, the Otsu method (Otsu, 1979) was selected for FN and glial fibrillary acidic protein staining, while the Moments method (O'Gorman, 1996) was used for α-SMA. Areas with erythrocytes were excluded manually due to strong autofluorescence of these cells and inability of thresholding algorithms to reliably exclude them. Of the remaining pixels, the

medium brightness was calculated. The brightness of a pixel is attributed a value between 0 and 255. Starting from the threshold, the sum of all included pixels times their assigned brightness was calculated and then divided by the number of all included pixels:

$$Mean\ brightness = \frac{\sum_{255}^{threshold}(number\ of\ pixels\ \times\ value\ of\ brightness)}{\sum_{255}^{threshold} number\ of\ pixels}$$

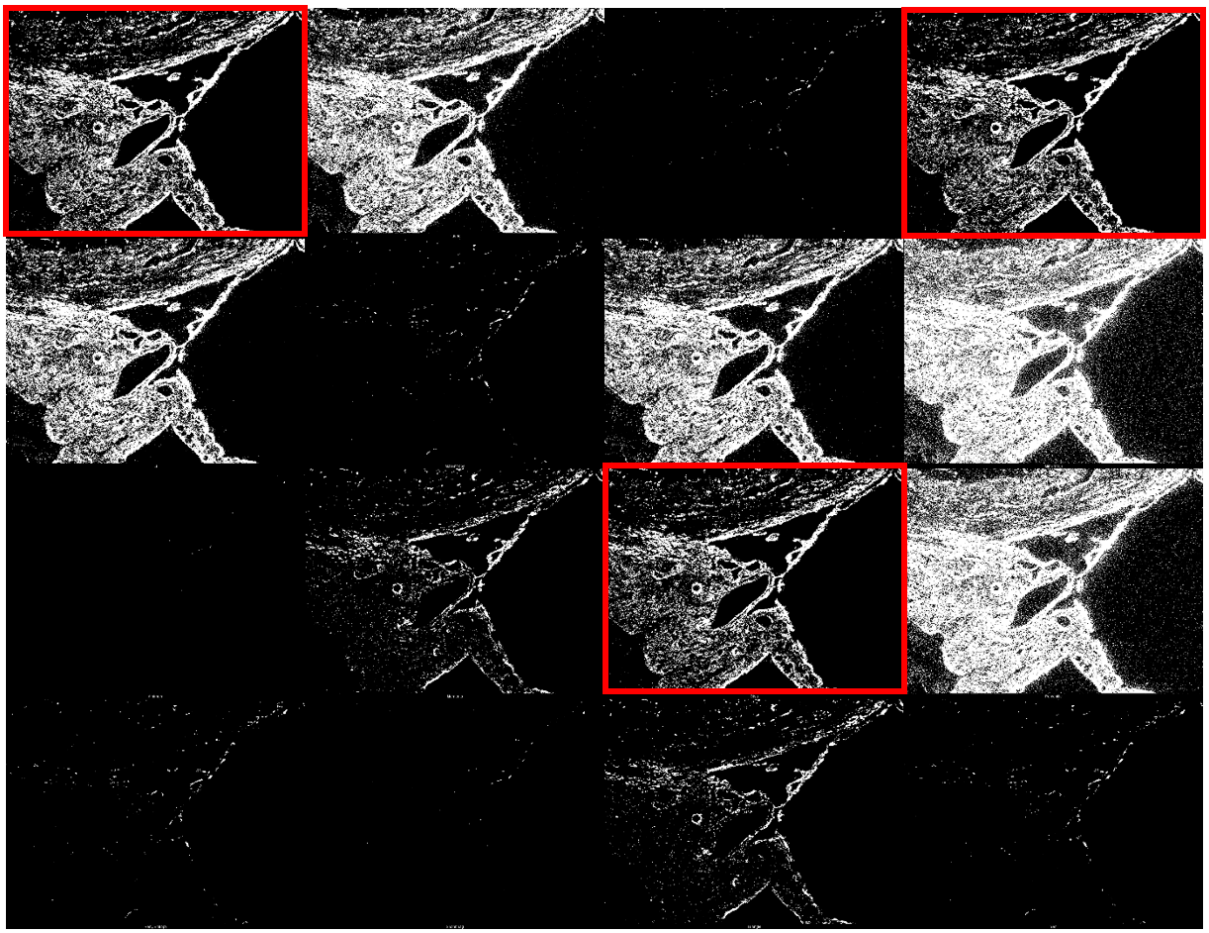

Figure 6 – Example of an output of Auto Threshold Plugin. Each of the 16 images depicts the same microscopic image under a different thresholding variant, with pixels included in the threshold shown in white, and others in black. Suitable thresholds excluding noise sufficiently and fully representing the anatomical structures, especially showing a continuous inclusion of pixels surrounding the SC and TM as primary areas of interest, are marked with a red rectangle.

This yielded a mean brightness value for all pixels included in the analysis. However, microscope images are often taken with different settings across sample sets, as staining intensity may vary, and different exposure times might be required. This variation would limit the method to small, internally consistent image sets. Moreover, the method requires sufficient statistical power (i.e., a high number of images), which is not always feasible.

So how can brightness be compared across images taken under different settings? The solution is to normalize the absolute brightness to a relative value. Relative brightness is calculated by comparing the mean brightness of a given image to the average brightness of all images taken under the same conditions.

This is done by first computing the group's average brightness – i.e., summing all brightness values and dividing by the number of images. The relative brightness of an individual image is then calculated by dividing its mean brightness by this group average. Expressed as a formula:

$$relative\ mean = \frac{brightness\ mean\ of\ one\ picture}{\sum all\ brightness\ means} \times number\ of\ pictures$$

In this study, these values were multiplied by 100 to bring them closer in scale to the original absolute values. This linear transformation was performed for ease of interpretation. The method was initially validated using a small dataset of microscope images with clearly distinguishable differences, before being applied to FN and α-SMA stainings of CD1 mouse eyes.

3.6.3 Validation Dataset

For validation purposes, a set of six microscope images was selected from a larger dataset that was already established and proven to show a difference between WT and tg littermates with another quantification method (Reinehr et al., 2019). However, the method of quantification described by Reinehr et al. (2019) is only applicable for larger and more continuous areas of interest in tissue sections and was therefore not suitable for the purposes of this thesis. As the region of interest spanned the entire retina, treatment of the samples changed slightly. Only regions of the picture underwent examination that included all layers of the retina and where the cell column from top to bottom was entirely visible in the picture. Threshold-setting method remained Otsu.

3.6.4 Quantification of Extracellular Matrix in Electron Microscopy

To verify the effect of the CTGF pathway on the deployment of ECM, slides of ICA were examined using EM as well. The region between the inner wall endothelium of

SC and the consecutive four cell layers of the TM was analyzed. This area was selected as it contains the JCT, or inner wall region (Johnson, 2006). The inner wall region is, as described above, formed by two to five cell layers embedded in a loose connective tissue ECM, measuring 2–20 µm. This region seems to be responsible for nearly all of the resistance to AH outflow (Ethier, 2002; Johnson, 2006). Hence, it makes sense to focus on this area for further investigation. All procedures and measurements described in the following paragraph were conducted using ImageJ Version 1.51f (Schindelin et al., 2012) with basic calculations and data collection performed in Microsoft Excel 2016 (Microsoft Corporation, Redmond, WA, USA).

The area of interest was identified, and its surface measured after ensuring the correct scale was selected in ImageJ. Subsequently, both the ECM-covered and non-ECM-covered areas were measured. Figure 7 illustrates a typical image. The area covered by cells was calculated by subtracting the ECM and non-ECM-covered areas from the total area. To make the findings comparable between different sections, the relative amounts of the area covered by ECM, not covered by ECM, and covered by cells were calculated and compared.

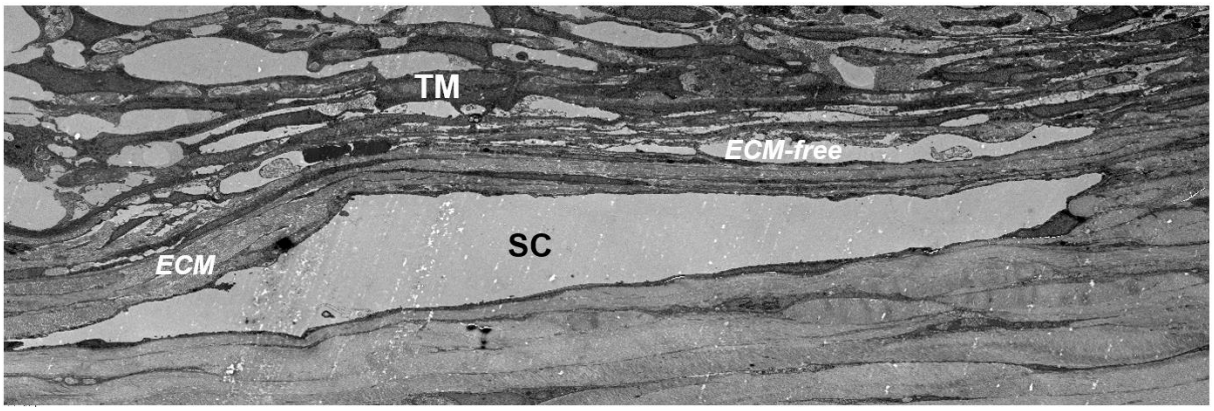

Figure 7 – ECM deployment in EM in TM above SC in a tg animal aged 52 weeks. Above SC, one can find the TM. Within the TM, it is easy to distinguish between ECM-covered (ECM) in darker grey and ECM-free areas (ECM-free) in light grey with cell bodies and nuclei in between.

3.6.4 Quantification of Optic Nerve Axons

3.6.4.1 Manual Quantification

POAG is characterized by axonal loss, as previously described. In order to assess the extent of the ON degeneration, axons were manually counted on cross-sections of ONs from different animals. Following paraphenylenediamine staining, images were acquired at 100× magnification. For each ON, five squares of 12500 µm^2 were defined

using a standardized mask. Within each square, all axons were counted using Image J (Schindelin et al., 2012). To estimate the total number of axons per nerve, the entire ON area was measured using ZEN imaging software (Carl Zeiss, Jena, Germany), and the axon count was extrapolated accordingly. The person performing the counting was blinded regarding the genotype of the examined mice.

3.6.4.2 Quantification with AxonJ

Quantification of ON axons by an expert may be subjective and susceptible to error. Therefore, automated axon quantification was additionally performed using AxonJ. AxonJ is a plugin for ImageJ that automatically identifies and counts axons in ON cross-sections by detecting connected regions within defined size thresholds. Regions are counted as axons if their area falls between 0.144 µm² and 14.4 µm² (Zarei et al., 2016a, 2016b).

3.6.5 Structured Illumination Microscopy

3.6.5.1 General Introduction

SIM is a technique that allows to surpass the limits in resolution of conventional light microscopes. In general, due to the diffractive wave-nature of light, the best achievable resolution *d* of an even ideal microscope has long been defined by the light gathering ability of the imaging objective lens (the numerical aperture *NA*) and the wavelength of light, *λ*, used for imaging (Harten, 2017):

$$d = \frac{\lambda}{2NA}$$

In practical terms, *NA* values rarely exceed 1.5, and the usable wavelength range for conventional optics spans approximately 400 nm (blue) to 750 nm (far-red), resulting in a resolution limit of around 200 nm (Vangindertael et al., 2018).

However, several super-resolution microscopy techniques have recently been developed to circumvent this so-called diffraction limit (Coltharp & Xiao, 2012). One such method is SIM (Gustafsson, 1999), which enhances resolution by illuminating the sample with patterned light rather than uniform sample illumination. Compared to other

super-resolution microscopy techniques, it offers practical advantages: It is easily applicable as probes do not need special preparation, and image acquisition is relatively fast (Opstad et al., 2018). But how come the resolution of an acquired image can be increased by simply altering its illumination pattern? The following explanation follows *en gros* the description by Vangindertael et al. (2018).

The explanation requires at least a basic understanding of what a Fourier Transform (FT) is. FT is a mathematical paradigm based on the idea that signals of any complexity can be represented by an infinite summation of simpler sinusoidal components. This is illustrated in Figure 8, where a step function (A) is gradually replaced by more and more sinusoidal functions (B to E, in blue), resulting in a better and better approximation (red) of the initial function.

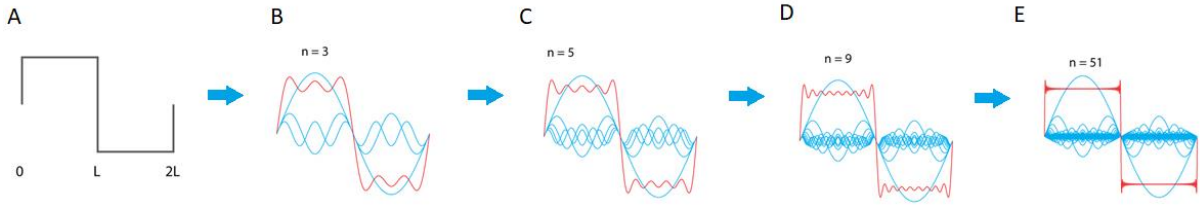

Figure 8 – FT (Vangindertael et al., 2018), adapted. (A) is depicting a step function representing an arbitrary signal. (B)-(E) are illustrating how this function can be approximated by a sum (red) of sine functions (blue) with n indicating the number of overlaying sine functions.

The step function example is a one-dimensional signal with very low complexity. But FT can be applied on data of *any* complexity or dimensionality. Images, for example, can be interpreted as a two-dimensional signal consisting of a superposition of spatial frequencies of varying orientations.

The result of this transformation is called a Fourier image (FI), which is fully interchangeable with the original image - no information is lost. In an FI, the distance from the centre encodes frequency, while pixel brightness encodes amplitude. Thus, bright spots far from the centre represent high-frequency, high-amplitude components. Figure 9 illustrates this transformation.

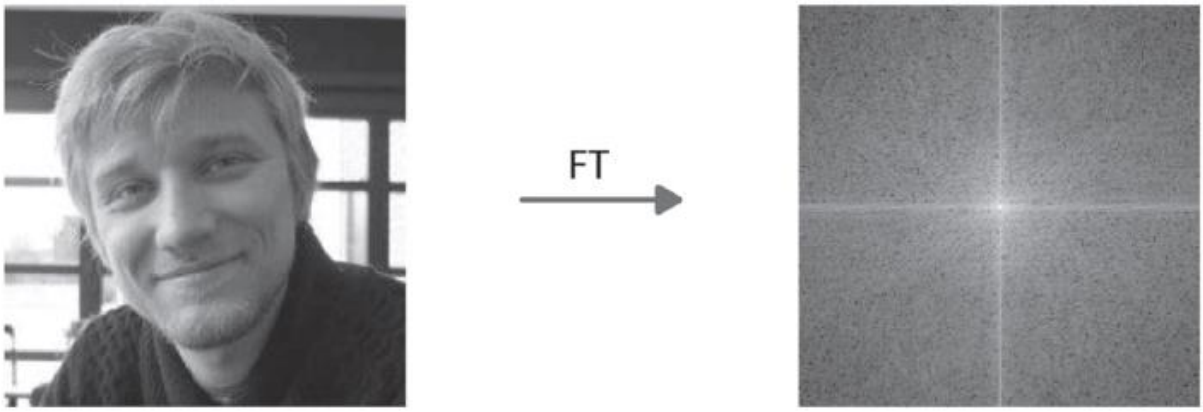

Figure 9 – FT of an image (Vangindertael et al., 2018), adapted. A photograph (left) is transformed into its corresponding FI.

Crucially, coarse image features are represented near the center of the FI, while fine details (i.e., high-resolution information) are located toward the periphery (Figure 10).

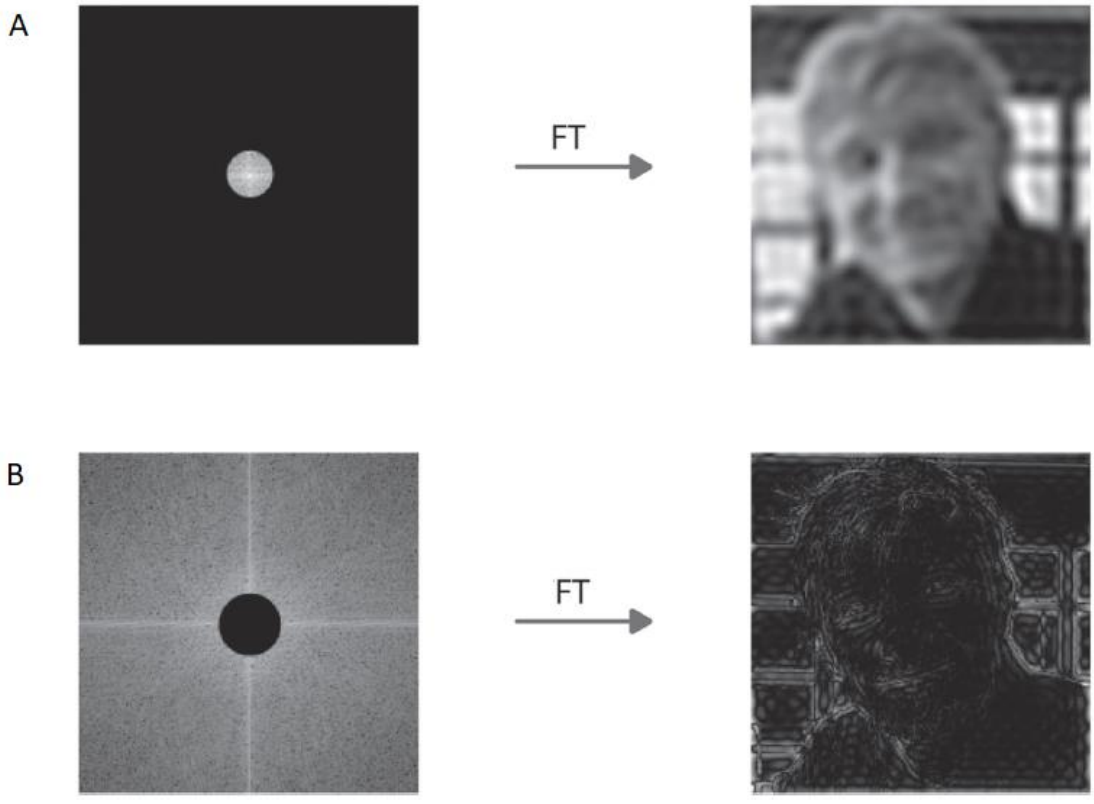

Figure 10 – Spatial distribution of information in a FI (Vangindertael et al., 2018), adapted. In the Fourier image, low frequency information is located near the center (A), while high frequency information (B) is located near the edges of the Fourier image. This means that the center of the picture contains the coarser information (A), whereas the information increasing the resolution is located further from the center (B).

A standard microscope cannot capture the full FI; it is limited to a finite region around the center, defined by the maximum detectable spatial frequency. This limitation explains why optical resolution is constrained. The radius of observable region of frequencies in Fourier space is denoted here as k_0, λ still being the wavelength, and NA the numerical aperture (Arnison & Sheppard, 2002):

$$k_0 = \frac{2NA}{\lambda}$$

As shown above in Figure 10, the fine details of an image are encoded on the edges of the FI. Thus, increasing the numerical aperture expands the observable range and improves resolution.

SIM overcomes this frequency limitation by artificially enlarging the numerical aperture by generating Moiré patterns through structured illumination. A Moiré pattern emerges when two high-frequency patterns interfere, creating a third pattern with lower apparent frequency that is within the detectable range of a standard microscope. This is exemplified in Figure 11, where two dotted patterns, put on top of each other, form a completely new pattern with lower frequency components:

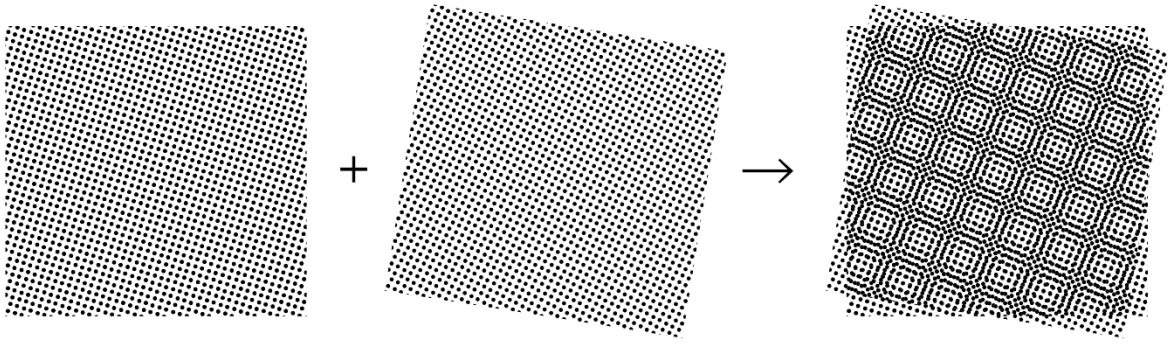

Figure 11 – Moiré effect in two dotted patterns. An overlay (right) of two dotted patterns (left and middle) creates a pattern of a lower frequency.

In SIM, the sample is illuminated with defined, striped light patterns at different angles (Galbraith & Galbraith, 2011). Figure 12 demonstrates how a sample illuminated like this creates different Moiré patterns. It is crucial to see that the resulting Moiré pattern has a lower frequency than its component frequencies – which means that it can pass the resolution barrier even though the two frequencies by themselves might not have been detectable before. Because the illumination pattern is known, the original high-

frequency information can be mathematically reconstructed from the recorded Moiré patterns, thereby producing a super-resolved SIM image (Gustafsson, 2000).

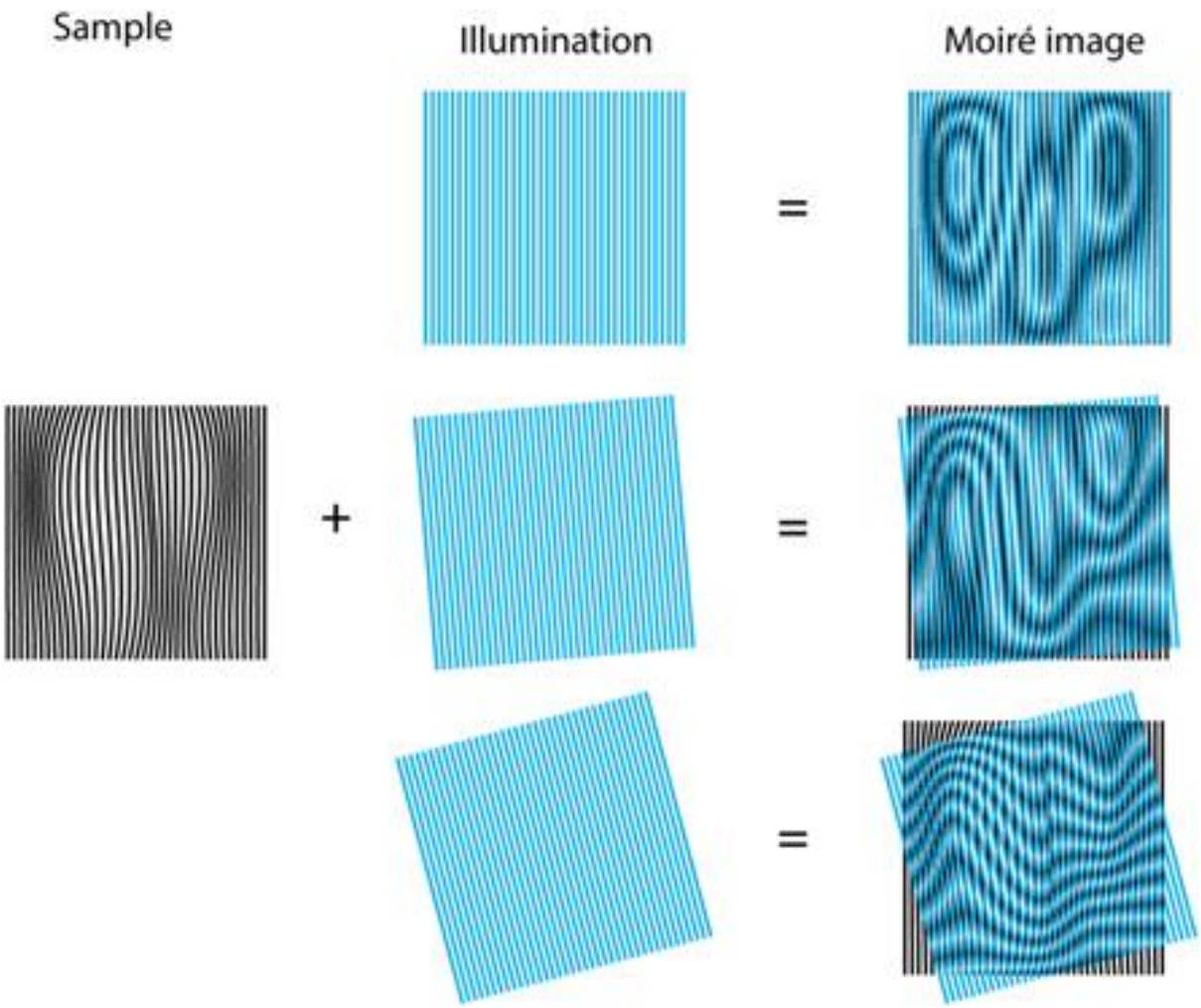

Figure 12 – Moiré effect in SIM Imaging (Vangindertael et al., 2018). A sample containing features with high spatial frequencies (left) is illuminated with different defined, periodic illumination patterns (middle). This creates different Moiré fringes (right) of lower frequency that can be readily resolved by the optical system of a microscope.

3.6.5.2 Structured Illumination Microscopy as Performed in This Study

In this study, SIM imaging was performed using a DeltaVision OMX V4 Blaze imaging system with a 60x 1.42 NA oil-immersion objective, three sCMOS cameras, and 405, 488, 568, and 642 nm lasers for excitation of the fluorophores. Optical resolution of the system (3D SIM) is 110-160 nm laterally, and 340-380 nm axially as specified by the vendor. Exact resolution depends on the color channel as resolution is dependent on wavelength as described above.

To surpass the diffraction limit, the used Structured Illumination Microscope uses sinusoidal illumination patterns and takes 120 images per 1 µm of z-stack thickness per color channel (3 angles × 5 phase shifts × 8 planes per µm). For image registration and color alignment the manufacturer-supplied SoftWoRx program (GE Healthcare) was used. Further image processing was done using Fiji/ImageJ (Schindelin et al., 2012).

3.7 Statistical Analysis

All numeric data were collected in Microsoft Excel 2016 (Microsoft Corporation, Redmond, WA, USA) documents. Statistical analyses were performed using IBM SPSS Statistics version 25 (IBM, Armonk, NY, USA) and JASP Stats version 0.19.1.0 (Department of Psychological Methods, University of Amsterdam, Amsterdam, The Netherlands). Statistical significance was set at $p < .05$, indicating that results with a probability of less than 5% of occurring under the null hypothesis were considered significant.

Additionally, SD is provided as a measure of data dispersion around the mean. A higher SD indicates greater variability, meaning the data points are more dispersed, while a lower SD suggests that the data points are closer to the mean, indicating less variability (Anderson, 1960).

3.8 Declaration of the Use of Generative Artificial Intelligence

During the preparation of this work, the author used DeepL Translate to translate the abstract from English to German and both ChatGPT by OpenAI and Consensus AI by Consensus NLP for online research and for reviewing the text for spelling and grammar errors. After using these tools, the author carefully reviewed and edited the content as needed and takes full responsibility for the content of the publication.

4 Results

4.1 Genotyping

To distinguish between mice carrying the tg CTGF-overexpression and their WT littermates, a PCR and agarose gel electrophoresis were performed as described above. Tg animals showed a band both in the SV40 as well as in the βB1-PCR at 360 bp (Figure 13), whereas WT animals did not.

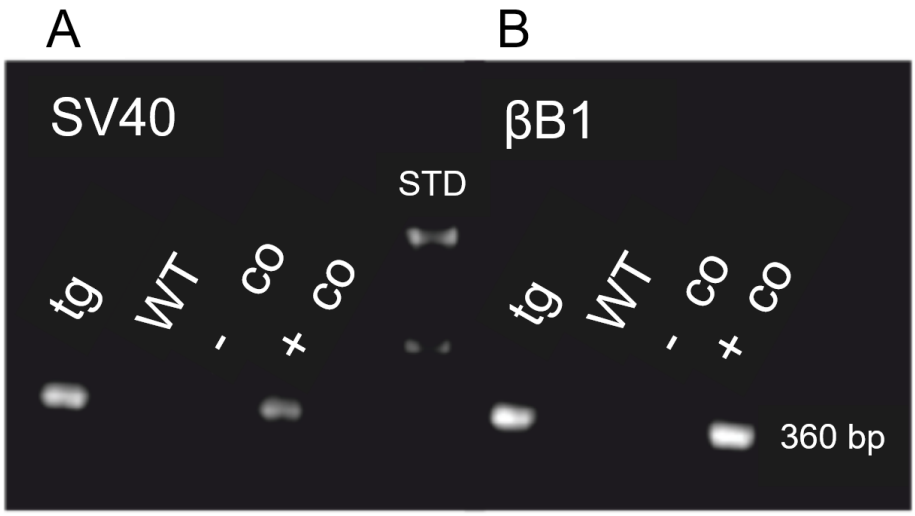

Figure 13 – Detection of PCR products after agarose gel electrophoresis (kindly provided by M. Sc. F. Frömel née Scherl, adapted). Standard (STD) showed a band at 100 bp at the top and 500 bp at the bottom. Tg animals (tg) showed a band at 360 bp both in SV40- (A) and βB1-PCR (B) as did the positive controls (+co). Negative controls (-co) and WT littermates (WT) did not show any bands.

4.2 Intraocular Pressure Measurements for Mice Aged 26 and 52 Weeks

A group of 69 animals was examined. Of those, 35 were aged 26 weeks (22 WT and 13 tg), and 34 were aged 52 weeks (22 WT and 12 tg). To assess the difference between WT and tg animals at 26 and 52 weeks of age, statistical analysis was performed using an independent samples t-test.

At 26 weeks of age, there was a difference in IOP between WT and tg animals. Mean IOP for WT animals was 16.32 mmHg, SD_{WT} = 3.695, compared to 19.70 mmHg for their tg littermates, SD_{tg} = 4.345. Therefore, IOP was elevated by 21% in tg animals at 26 weeks of age. This difference was statistically significant, p = .009.

At 52 weeks of age, the difference in IOP between WT and tg animals was more pronounced. The mean IOP for WT animals was at 12.90 mmHg, SD_{WT} = 2.940, compared to 17.51 mmHg for their tg littermates, SD_{tg} = 3.083. IOP was therefore elevated by 36% in tg animals at 52 weeks of age. This difference was also statistically significant, $p < .001$.

For further assessment, a unifactorial analysis of variance (2x2 ANOVA) was performed with between subject factors genotype (tg, WT) and age (26, 52 weeks). The mean IOP regardless of age was 14.60 mmHg in WT animals, SD_{WT} = 3.601, compared to 18.68 mmHg in tg animals, SD_{tg} = 3.891. This represents an increase of 28% or almost one third in tg animals. The difference between both genotypes across both age groups was statistically significant, $p < .001$. Regarding the effect of age on both genotypes, IOP decreased statistically significant between 26 and 52 weeks of age. The mean IOP declined from 17.5 mmHg at 26 weeks of age, SD = 4.156, to 14.5 mmHg at 52 weeks of age, SD = 3.697, which corresponds to a 17% reduction, $p = .003$. The factors 'age' and 'genotype' did not show any significant interaction, $p = .461$. Figure 14 provides an overview of the findings.

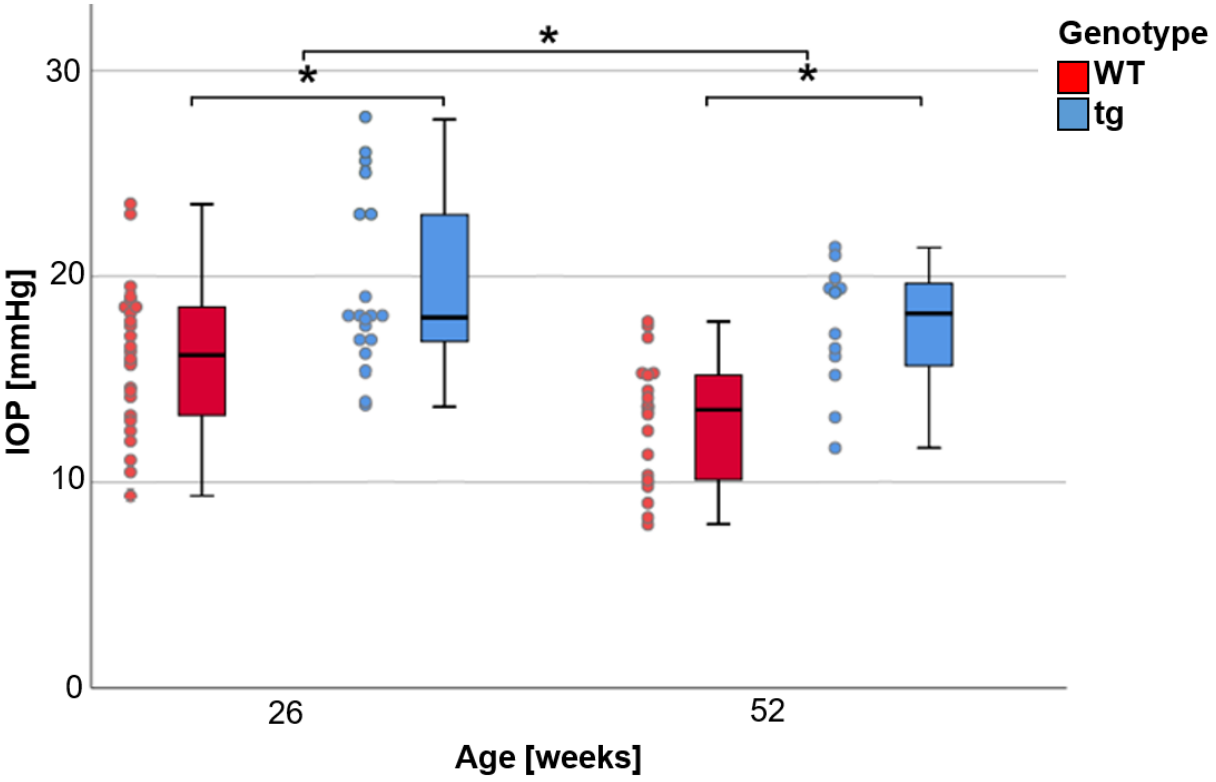

*Figure 14 – IOP at 26 and 52 weeks of age, both for WT mice and their tg littermates. Center horizontal lines show the medians. Box limits indicate the 25th and 75th percentiles. Whiskers extend 1.5 times the interquartile range from the 25th and 75th percentiles. Data points are plotted as colored dots; *p < .05.*

4.3 Light and Fluorescence Microscopy

4.3.1 Fluorescence Microscopy Acquired Images

Slides were stained for FN and α-SMA. FN is a marker for changes in ECM, α-SMA for cell contractility. Both are known to undergo changes in the development of POAG, especially in the TM (Kottler et al., 2005). Both FN and α-SMA are suspected to be stronger expressed in POAG as cell contractility intensifies and more ECM is produced. The findings visually supported this hypothesis, which is illustrated in Figure 15. To further corroborate this visual impression, an objective analysis of microscope pictures was performed afterwards.

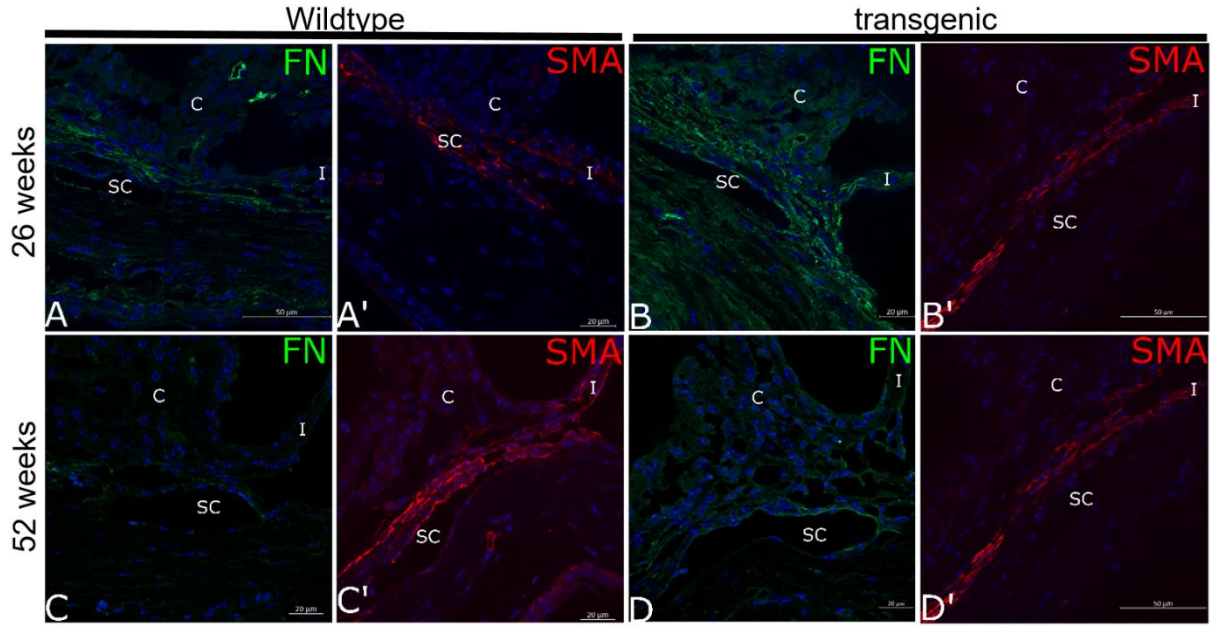

Figure 15 – Staining overview for FN and α-SMA at 26 and 52 weeks. An example of each condition is included in the picture: (A) 26 weeks FN staining of a wildtype animal, (A') 26 weeks α-SMA staining of a wildtype animal, (B) 26-week FN staining of a transgenic animal, and so forth. FN indicates an FN labelling, SMA an α-SMA labelling. C indicates the ciliary body, I the iris, and SC Schlemm's Canal.

4.3.2 Objective Analysis of Microscope Pictures

4.3.2.1 Validation Dataset

For the validation of the new method, six microscope pictures of a previously published glial fibrillary acidic protein staining were compared. These pictures were selected for their visually detectable difference between both groups; thus, they could be seen as significantly different under currently established, expert-based methods of examination. In the study mentioned above, the whole of GFAP stainings showed a strong trend

towards an enhanced GFAP signal in βB1-CTGF animals with p = .090 using the different quantification method employed in the paper by Reinehr et al. (2019), combined with a significant up-regulation of GFAP mRNA levels in βB1-CTGF retinae, p = .020.

Statistical analysis was performed using an independent samples t-test. The tg animals appeared to have an increased relative intensity of 40% compared to their WT littermates. Relative values of intensity for both genotypes (M_{WT} = 0.83, SD_{WT} = .118; M_{tg} =1.17, SD_{tg} = .080) differed statistically significant, p = .018. Figure 16 gives a graphic overview of the results.

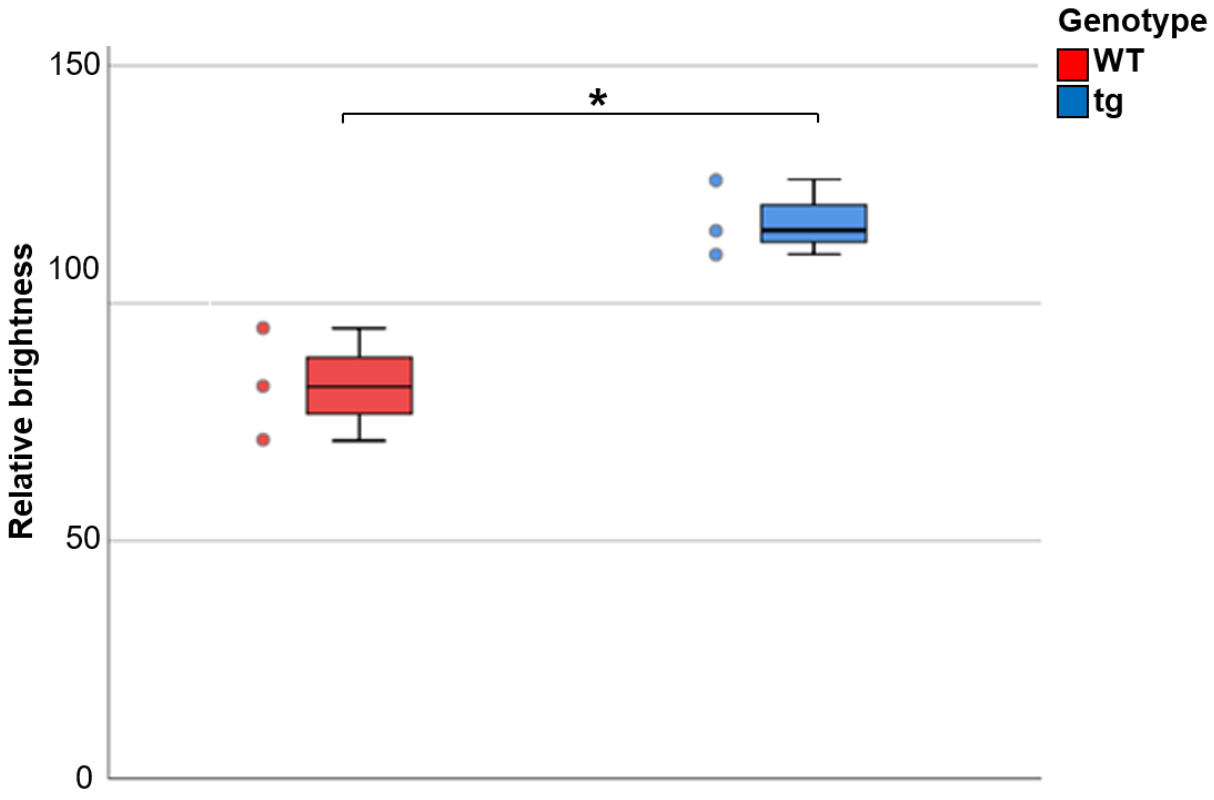

*Figure 16 – Relative values of brightness in sections of GFAP mice of the validation dataset, both of tg mice and WT littermates. Center horizontal lines show the medians. Box limits indicate the 25th and 75th percentiles. Whiskers extend 1.5 times the interquartile range from the 25th and 75th percentiles. Data points are plotted as colored dots, *p < .05.*

4.3.2.2 CD1 Mice Aged 26 and 52 Weeks

A group of 60 animals was examined regarding differences in staining brightness. Table 11 provides the exact distribution of the animals regarding age, genotype, and staining.

	FN staining		**α-SMA staining**		∑
Age	WT	tg	WT	tg	
26 weeks	11	6	11	9	37
52 weeks	5	6	5	7	23
∑	16	12	16	16	**60**

Table 11 – Distribution of Slides Analysed, According to Age and Genotype

At 26 weeks of age, the difference in relative brightness in FN staining between WT and tg animals was calculated using an independent samples t-test. Mean brightness for WT animals was 91.49, SD_{WT} = 31.637, compared to 115.60 for their tg littermates, SD_{tg} = 26.651. Thus, mean brightness was 26% higher in tg animals; however, the difference was not statistically significant, p = .135.

At 26 weeks of age, the difference in relative brightness in α-SMA staining between WT and tg animals was again calculated using an independent samples t-test. Mean brightness for WT animals was 84.73, SD_{WT} = 63.517, compared to 96.44 for their tg littermates, SD_{tg} = 49.075. Mean brightness was 14% higher in tg animals, yet the difference was not statistically significant, p = .656.

At 52 weeks of age, the difference in relative brightness in FN staining between WT and tg animals was also analysed using an independent samples t-test. Mean brightness for WT animals was 90.29, SD_{WT} = 14.347, compared to 104.00 for their tg littermates, SD_{tg} = 20.391. Therefore, mean brightness was 15% higher in tg animals, yet the difference was not statistically significant, p = .239.

Regarding α-SMA staining at 52 weeks of age, differences between WT and tg animals were assessed using an independent samples t-test. Mean brightness for WT animals was 80.57, SD_{WT} = 14.493, compared to 118.84 for their tg littermates, SD_{tg} = 22.002.

In this case, mean brightness was 47% higher in tg animals, and the difference was statistically significant, p = .007.

For further assessment, statistical analysis was performed using a multifactorial analysis of variance (2x2x2 ANOVA) with between subject factors genotype (tg, WT), age (26, 52 weeks) and staining (FN, α-SMA). Mean relative brightness, regardless of age or staining, was 87.48 for WT animals, SD_{WT} = 41.174, compared to 107.77 for tg mice, SD_{tg} = 33.482 - an elevation of relative brightness by 23%. The difference was statistically significant, p = .006.

A similar difference between WT and tg animals was observed when comparing the stainings individually. For FN staining, mean brightness increased from 91.12 in WT mice, SD_{WT} = 26.879, to 109.80 in tg mice, SD_{tg} = 23.421, equalling an increase of 20.5%. For α-SMA staining, the means increased from 83.43 for WT animals, SD_{WT} = 52.437, to 106.24 for tg mice, SD_{tg} = 40.123, an increase of 27.3%. None of the other factors, especially not the age, had any statistically significant influence on the outcome; all ps > .210.
Figure 17 gives an overview of the findings.

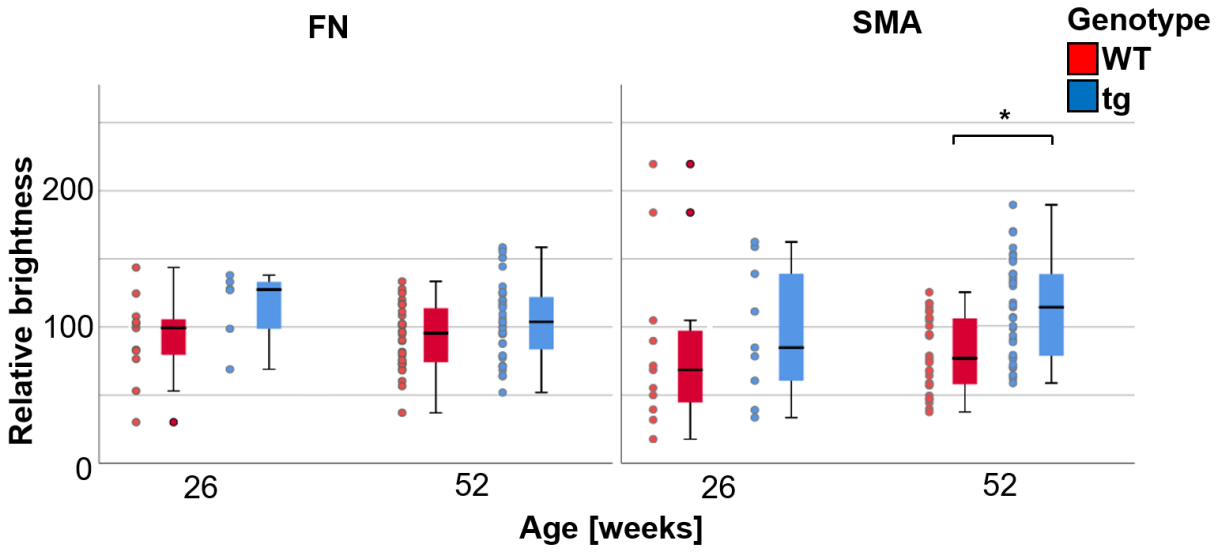

*Figure 17 – Relative values of brightness in sections of CD1 mice, both of WT and tg mice at ages 26 and 52 weeks and for FN and α-SMA staining. Center horizontal lines show the medians. Box limits indicate the 25th and 75th percentiles. Whiskers extend 1.5 times the interquartile range from the 25th and 75th percentiles. Data points are plotted as colored dots. *p < .05.*

4.3.3 Quantification of Optic Nerve Axons

ON axons were counted both manually and automatically. The distribution of the ONs by age and genotype is shown in Table 12.

Age	WT	tg	∑
26 weeks	7	9	16
52 weeks	9	9	18
∑	16	18	**34**

Table 12 – Distribution of ON Analysed, Regarding Age and Genotype

4.3.3.1 Statistical Analysis of Manual Count

The results regarding the two age groups were first compared using an independent samples t-test. At 26 weeks, mean manual axon count for WT animals was 34,436, SD_{WT} = 10,518.642, compared to 28,864 for their tg littermates, SD_{tg} = 7,288.392. This represents a 17% lower manual axon count in tg animals. However, the difference was not statistically significant, p = .253.

At 52 weeks, mean manual axon count for WT animals was 37,237, SD_{WT} = 6,176.248, compared to 29,110 for their tg littermates, SD_{tg} = 7,053.320. This corresponds to a 22% reduction in tg animals, and the difference was statistically significant, p = .019.

The results were also compared using a unifactorial analysis of variance. For the manual count, the 2x2 ANOVA included subject factors genotype (tg, WT) and age (26, 52 weeks). The mean axon count was 35,837 in WT animals, SD_{WT} = 8,490.913, compared to 29,003 in their tg littermates, SD_{tg} = 6,913.553. This means the number of axons was reduced by 19% in tg animals. The overall mean axon count per ON was 32,621, SD = 8,417.459. This difference was statistically significant, p = .019. None of the other factors, particularly age, had any statistically significant influence on the outcome, all ps > .584. Results are visualized in Figure 18.

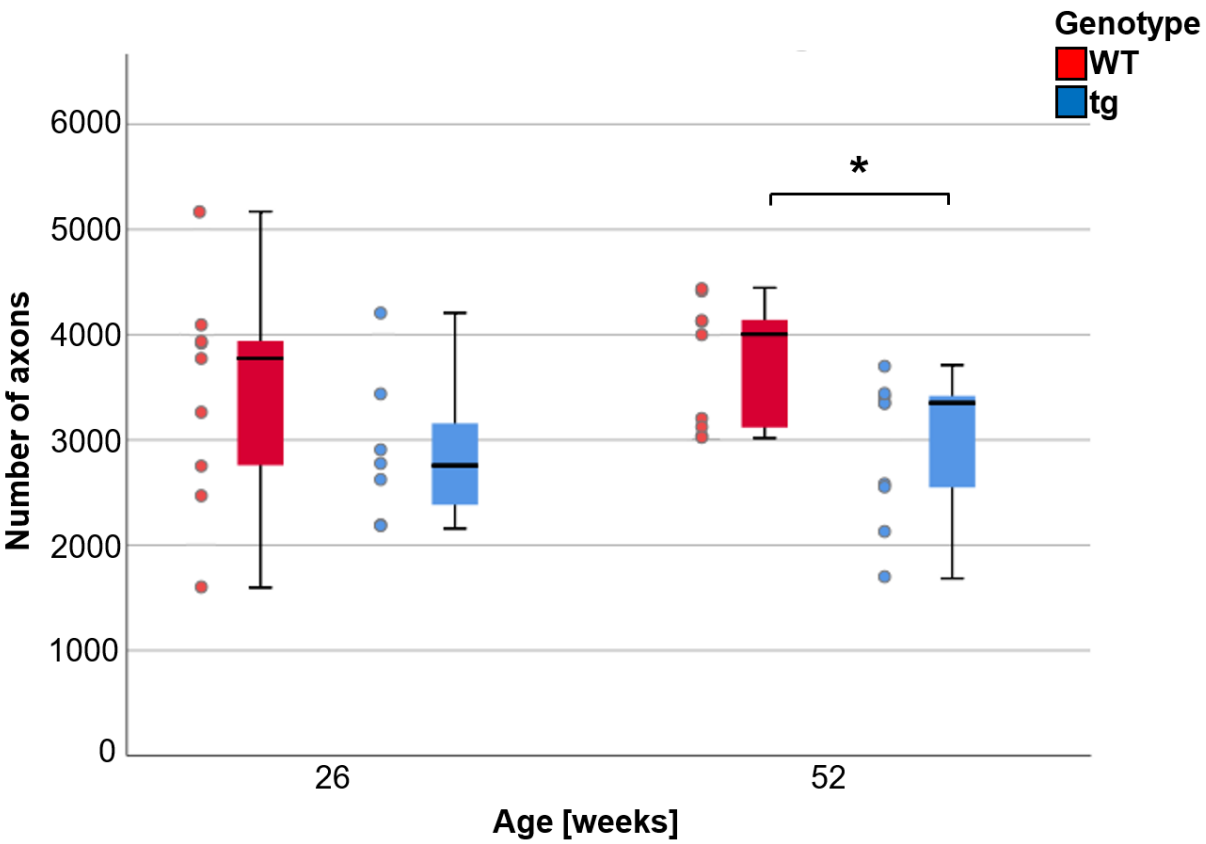

*Figure 18 – Manually acquired axon count in ON sections of both tg and WT mice, further differentiated by their age, 26 or 52 weeks. Center horizontal lines show the medians. Box limits indicate the 25th and 75th percentiles. Whiskers extend 1.5 times the interquartile range from the 25th and 75th percentiles. Data points are plotted as colored dots. *p < .05.*

4.3.3.2 Statistical Analysis of Automated AxonJ Count

As above, the results regarding the different age groups were compared using an independent samples t-test. At 26 weeks, mean automated axon count for WT animals was 48,354, SD_{WT} = 26,098.093, compared to 38,241 for their tg littermates, SD_{tg} = 26,183.223. Therefore, automated axon count was 21% lower in tg animals. The difference was not statistically significant, p = .455.

At 52 weeks, mean automated axon count for WT animals was 49,906, SD_{WT} = 14,816.825, compared to 55,380 for their tg littermates, SD_{tg} = 8,517.200. Therefore, automated axon count was elevated by 11% in tg animals. This increase was not statistically significant, p = .351.

Results from automated AxonJ counting were also assessed by a 2x2 ANOVA. Subject factors were, as above, genotype (tg, WT) and age (26, 52 weeks). The same group

of 34 ON sections was examined. The mean axon number was 49,130 in WT mice, SD_{WT} = 20,602.744, compared to 47,881 in tg mice, SD_{tg} = 19,749.019, which equals an overall difference of only 3%. The overall mean number of axons per ON was 48,542, SD = 19,908.580, which means the number of axons counted by AxonJ is nearly 50% higher than in the manual count (see above). Neither genotype, nor age, nor both factors altogether had any statistically significant influence on the counts, all ps > .184. An overview of the results is plotted in Figure 19.

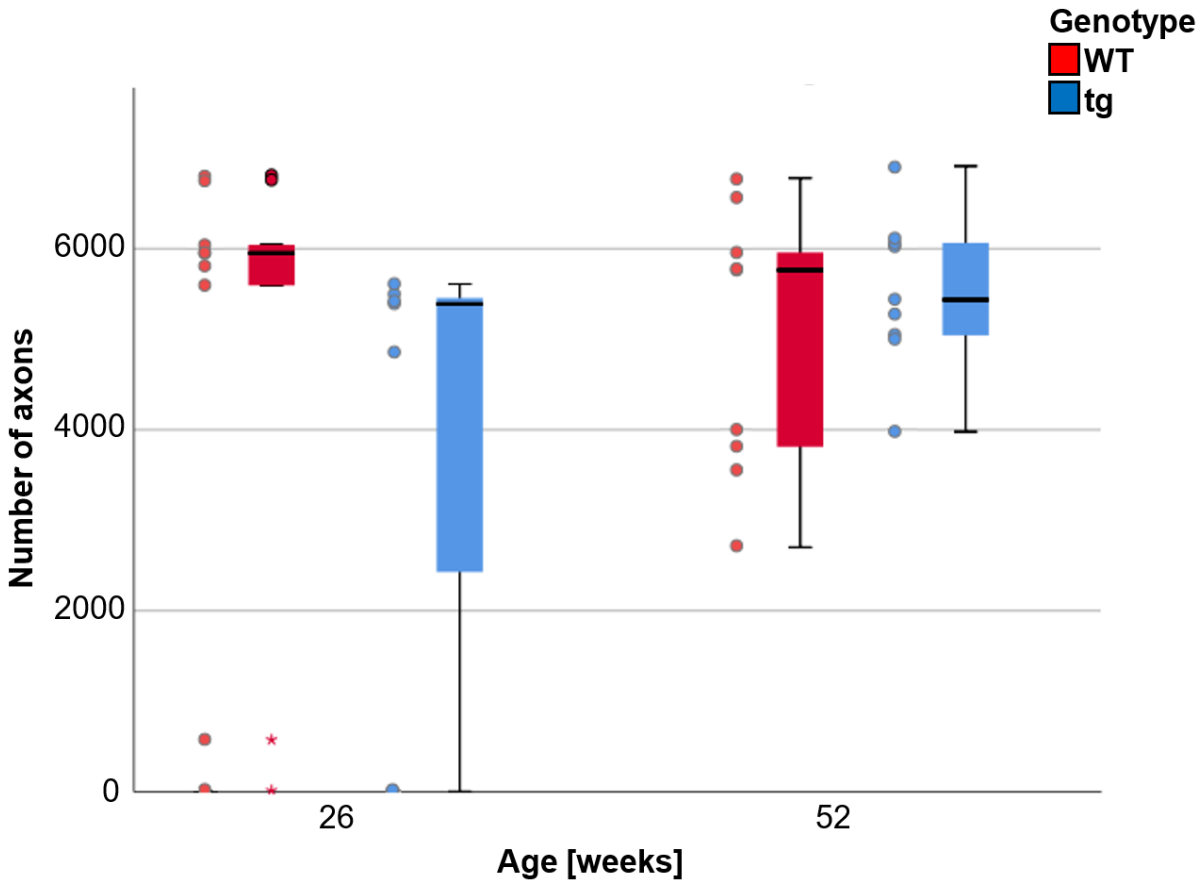

Figure 19 – Axon count in ON sections of both tg and WT mice as acquired by automated counting with AxonJ, further differentiated by their age, 26 or 52 weeks. Center horizontal lines show the medians. Box limits indicate the 25th and 75th percentiles, whiskers extend 1.5 times the interquartile range from the 25th and 75th percentiles. Data points are plotted as colored dots.

4.3.3.3 Correlation Between the Two Ways of Axon Count

To determine whether values of manual and automated count correlated with each other, a correlation was calculated. There was no significant correlation between the count in AxonJ and the manual count, r_{BP} = -.27, p = .122. This is illustrated in Figure 20, where the values are randomly distributed and do not gather along a line as they should if they were correlated.

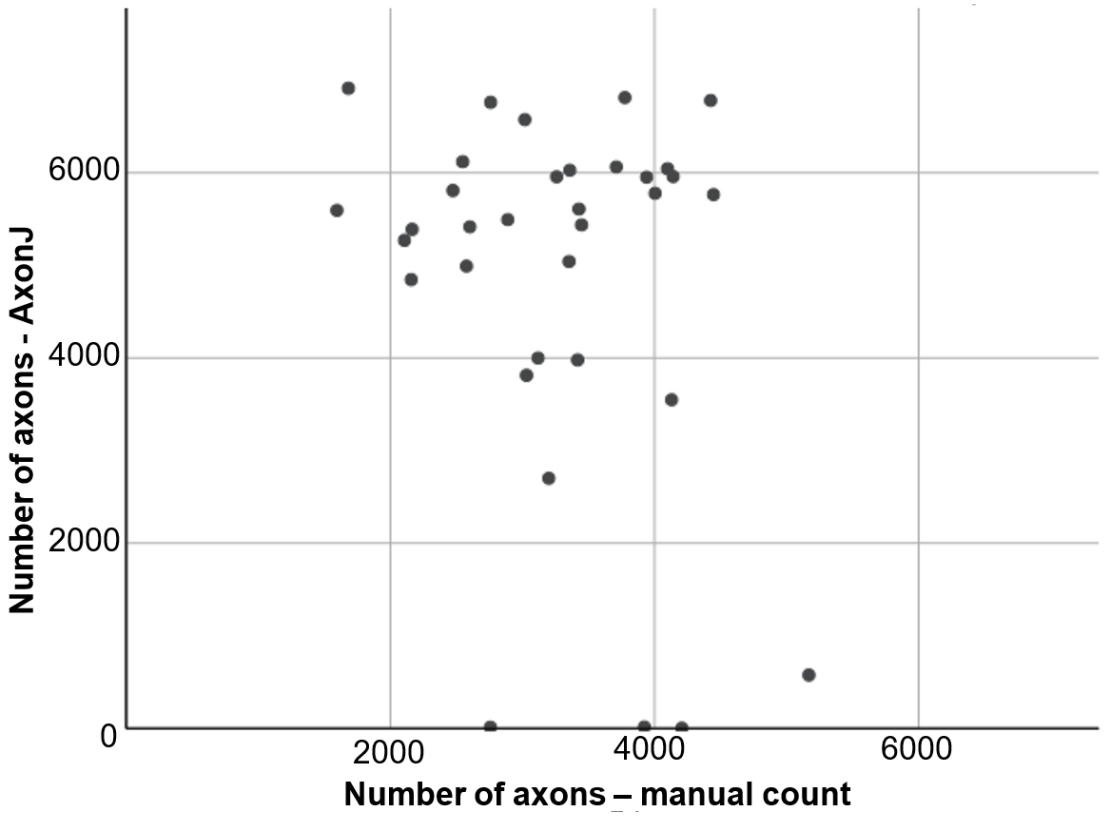

Figure 20 – Results for counts of ON axons from manual count and automated count with AxonJ plotted against each other. If the correlation between the two ways of assessing the number of axons was perfect, points would align along a straight line f(x)=y, as values should be identical. Here, they are more randomly distributed.

4.3.3.4 Problems Regarding the Automated Count

The number of axons counted was constantly higher in the automated count than in the manual count. Also, results from automated counting did not match with the results from manual counting from the same sample. Therefore, the question is why the automated counting failed to produce accurate results. The discrepancy can be explained by numerous inaccurate axon detections in automated counting, which is visualized in Figure 21. In the overview of the ON (a), it is easily visible that there are no axons on the top and bottom of the tissue section. However, one can see that AxonJ still counted axons there (marked in white), even though the density is lower (b). The same applies to the more detailed sections (c) and (d), where counted axons appear in turquoise: There are no axons in the blood vessel, but AxonJ counts them nonetheless. This problem is not unique to small capillary blood vessels, however: In (e) and (f), axons are counted in a region most probably consisting of ECM.

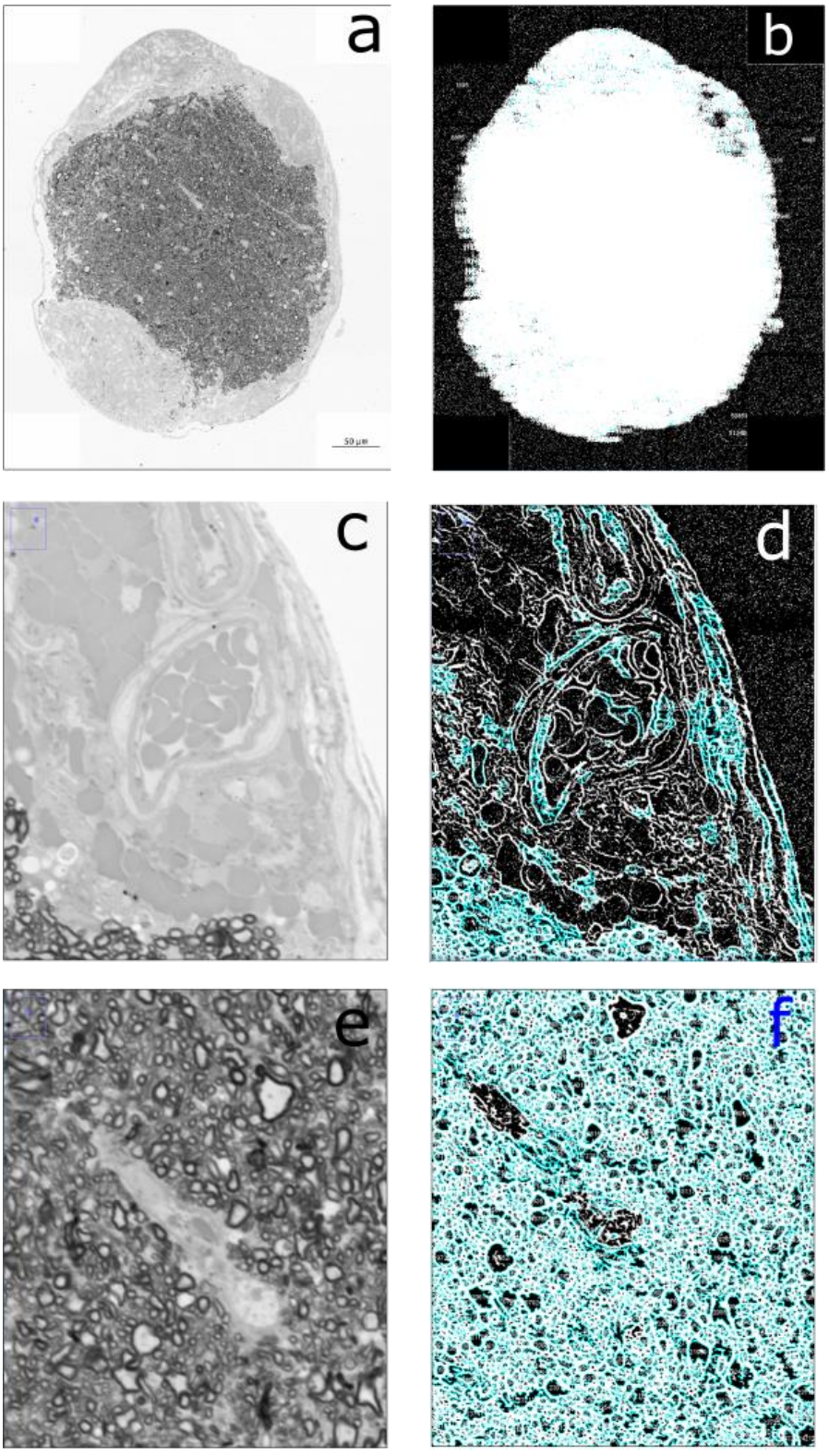

Figure 21 – Microscope pictures of an ON before (left) and after the automated axon count (right) with matching image sections. In pictures (a) and (b), it is clearly visible that axons (marked in white) are counted in upper and lower regions of the tissue sections where there are none, marked in white. The same is true for (c) and (d), a picture of a small capillary blood vessel, and (e) and (f), most probably a region with ECM; axons detected by AxonJ are marked in turquoise there.

4.3.4 Electron Microscopy

EM was performed to determine whether the increase in IOP could be caused by an obstruction of the TM outflow pathways (e.g., due to increased deposition of ECM components). The results of the quantification are shown in the following section. In EM pictures, the ultrastructure of the TM and SC endothelium was overall not obviously different between 26- and 52 week old mice (Figure 22). Optically empty spaces and putative pathways for AH were present underneath the inner wall endothelium, but they appeared to be reduced in tg and 52-week old mice. In addition, there was a visible increase in ECM deposition when comparing WT and tg animals at any age. In summary, the increase in IOP in tg animals might be caused by an increased amount of ECM in the TM impeding AH outflow.

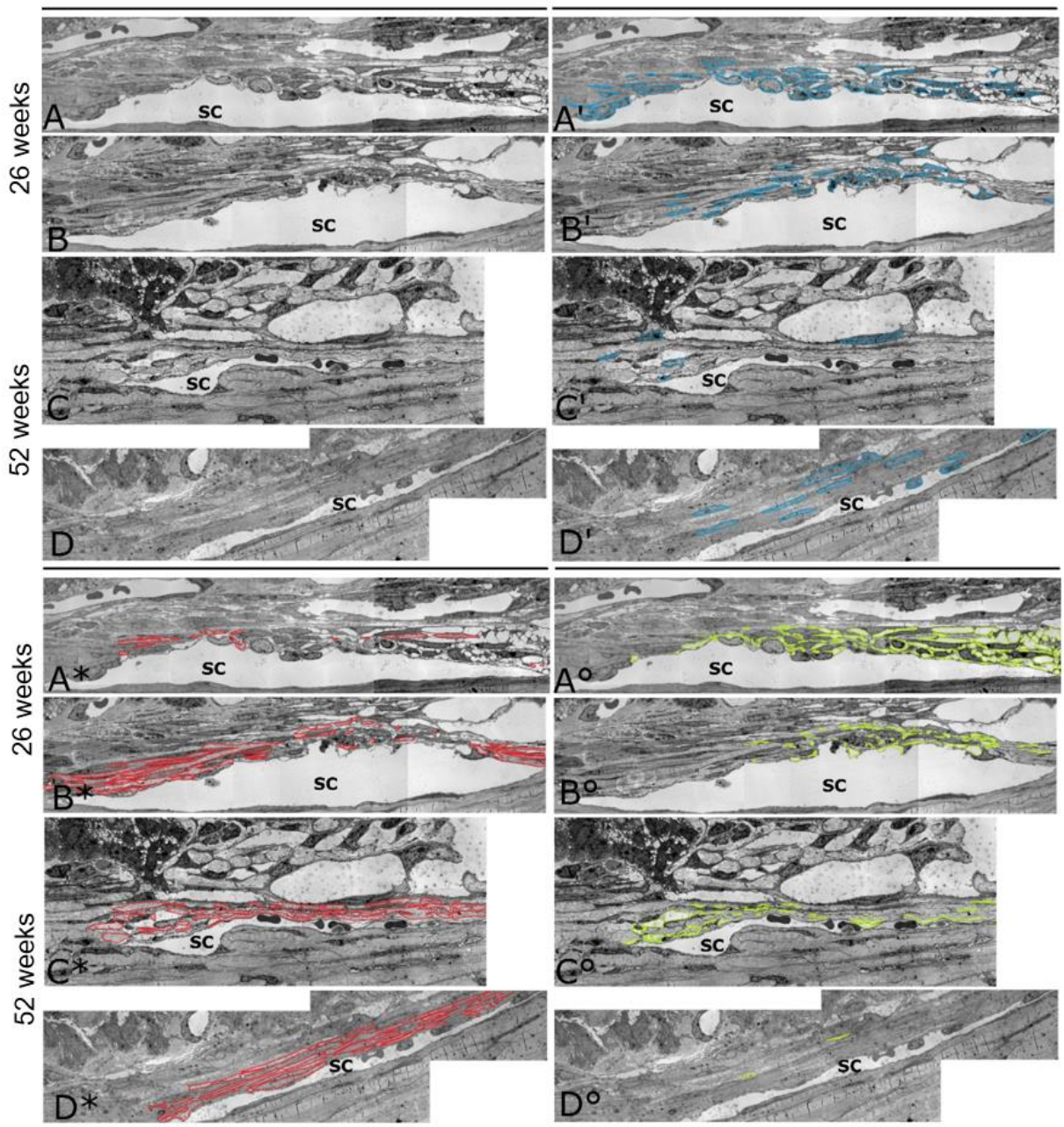

*Figure 22 – Overview of pictures of the ICA as obtained by EM. An example of each condition is included in the picture: (A) 26 weeks WT animal, (B) 26 weeks tg animal, (C) 52 weeks WT animal, (D) 52 weeks tg animal. Pictures marked with ' indicate marked cells in blue, * indicates areas filled with ECM marked in red, ° indicates an ECM-free area, marked in green. SC indicates Schlemm's Canal. Orientation: Iris and ciliary body are not, or only partly visible, but are located to the top and to the right.*

4.3.5 Quantification of Extracellular Matrix in Electron Microscopy

The fraction of surface both covered and not covered by ECM as well as the fraction covered with cells within the TM, especially the JCT, was measured as described above. A group of 33 sections of the ICA region was examined, Table 13 gives the exact distributions regarding age and genotype.

Age	WT	tg	∑
26 weeks	13	10	23
52 weeks	5	5	10
∑	18	15	**33**

Table 13 – Distribution of Pictures from EM, Regarding Age and Genotype

Results for mice aged 26 weeks were first compared by multiple independent sample t-tests. Values for the area covered with ECM (M_{WT} = 0.216, SD_{WT} = .147; M_{tg} = 0.426, SD_{tg} = .114) differed significantly, p = .001. Values for the ECM-free area (M_{WT} = 0.263, SD_{WT} = .104; M_{tg} = 0.131, SD_{tg} = .097) also differed significantly, p = .005. Values for the area covered with cells (M_{WT} = 0.520, SD_{WT} = .107; M_{tg} = 0.443, SD_{tg} = .106) did not show a statistically significant difference, p = .100.

Results for mice aged 52 weeks were comparable when analysed by multiple independent sample t-tests. Values for the area covered with ECM (M_{WT} = 0.272, SD_{WT} = .169; M_{tg} = 0.434, SD_{tg} = .137) did not differ significantly, p = .133. Values for the ECM-free area (M_{WT} = 0.194, SD_{WT} = .123.; M_{tg} = 0.045, SD_{tg} = .067) did differ significantly, p = .045. Values for the area covered with cells (M_{WT} = 0.534, SD_{WT} = .224; M_{tg} = 0.520, SD_{tg} = .115) did not show a statistically significant difference, p = .906.

Results were also compared in a 2x2 ANOVA including subject factors genotype (tg, WT) and age (26, 52 weeks). The mean area covered with ECM in WT mice regardless of age was 23%, SD_{WT} = .150, compared to 43% in tg mice, SD_{tg} = .117. ECM-free areas were 24% for WT animals, SD_{WT} = .111, and 10% for tg mice, SD_{tg} = .094. Statistically, both genotypes differed significantly regarding the region that was free of ECM, p < .01, as well as the region that was ECM-covered, p < .01. The area covered by cells was comparable, at 52% for WT animals, SD_{WT} = .141, and 47% for tg animals, SD_{tg} = .111. The area covered by cells did not differ significantly between WT and tg animals, p = .366.

The factor age was showing a slight tendency towards possible significance regarding ECM-free areas, p = .053. None of the other factors had any statistically significant influence on the outcome, all ps > .366. Results are visualized in Figure 23 to Figure 25.

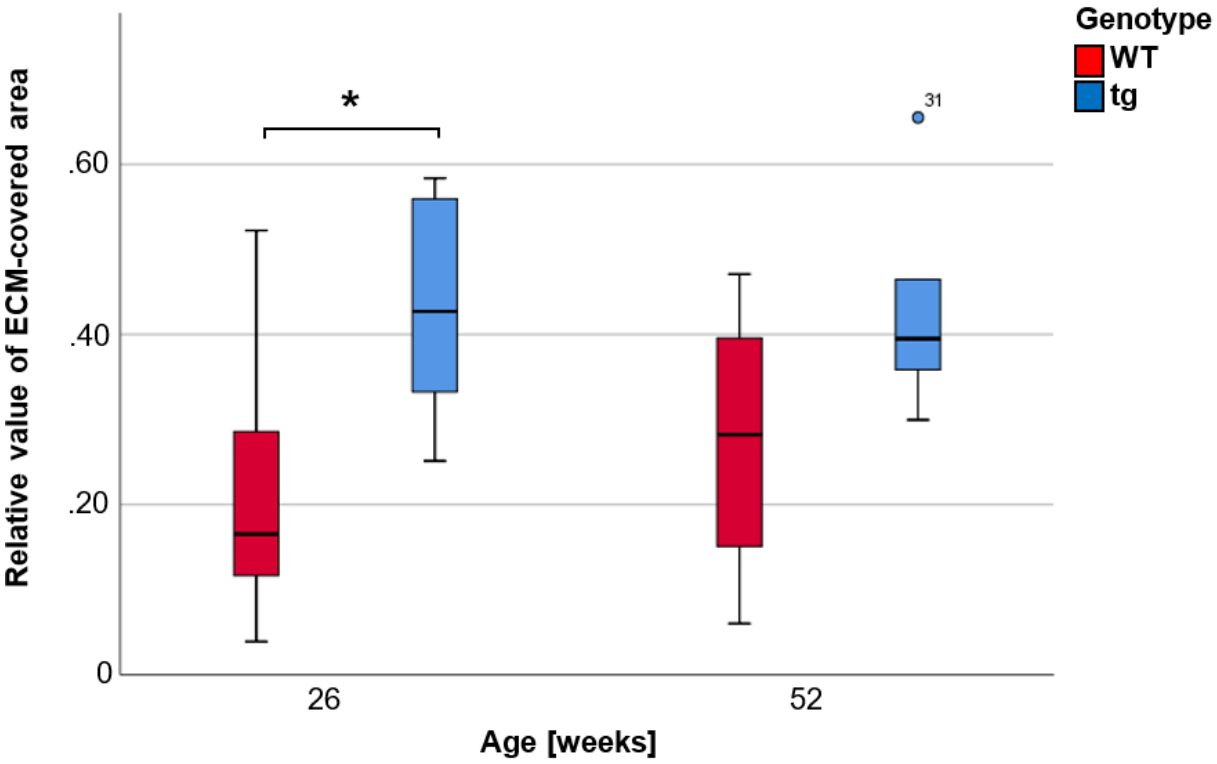

*Figure 23 – Relative value of area in the TM covered by ECM for tg and WT mice, further differentiated by their age, 26 or 52 weeks. Center horizontal lines show the medians. Box limits indicate the 25th and 75th percentiles, whiskers extend 1.5 times the interquartile range from the 25th and 75th percentiles. *p < .05.*

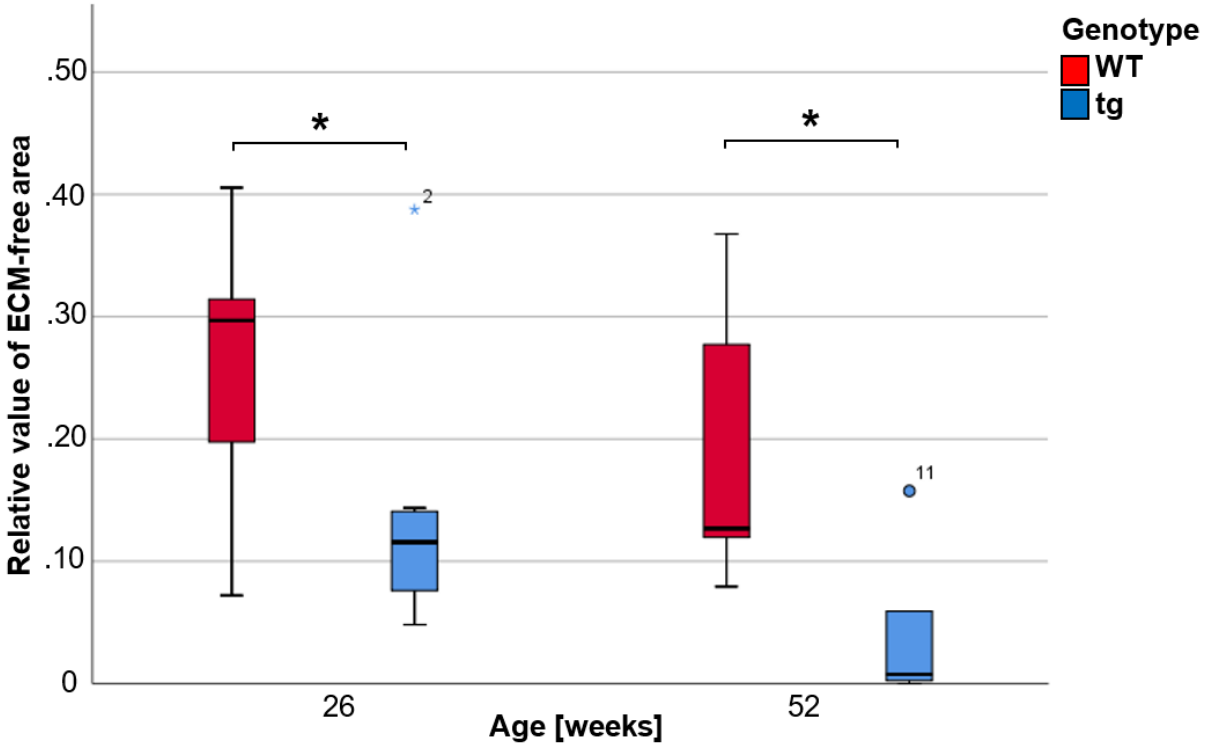

*Figure 24 – Relative value of area in the TM neither covered by cells nor by ECM of both tg and WT mice, further differentiated by their age, 26 or 52 weeks. Center horizontal lines show the medians. Box limits indicate the 25th and 75th percentiles, whiskers extend 1.5 times the interquartile range from the 25th and 75th percentiles. *p < .05.*

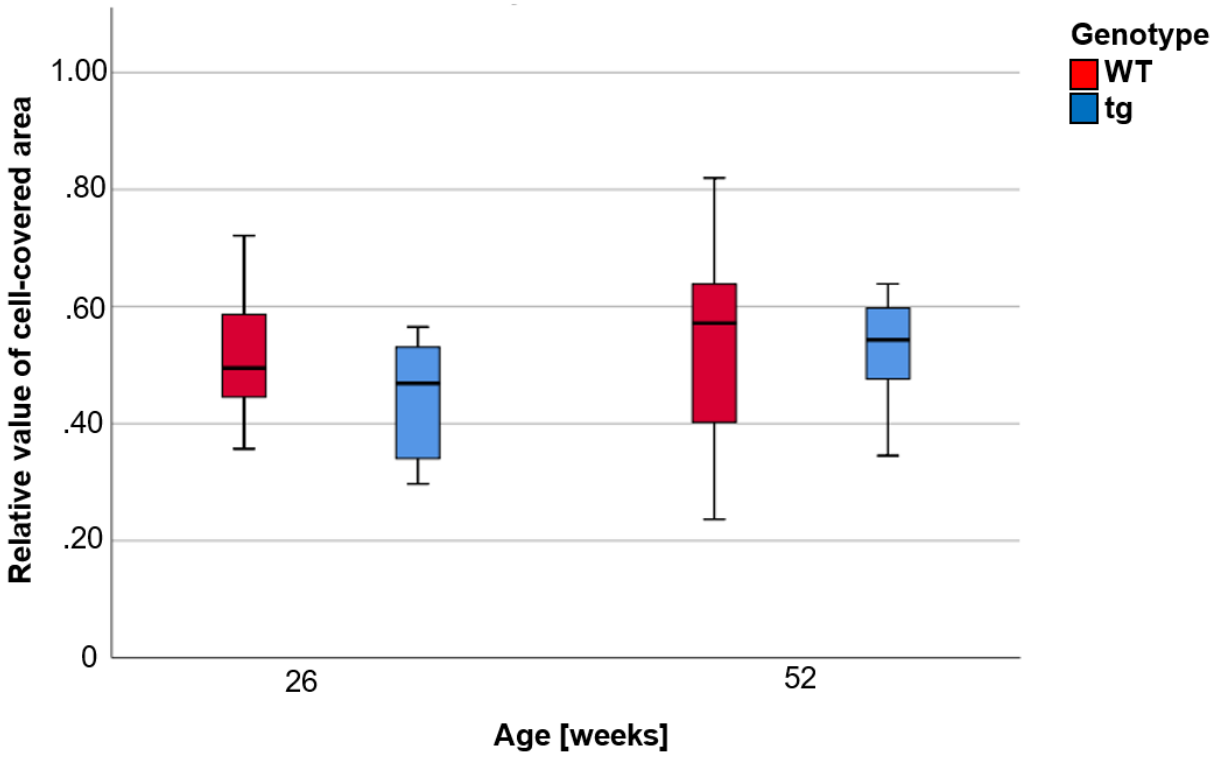

Figure 25 – Area in the TM covered by cells as a relative value for tg and WT mice, further differentiated by their age (26 or 52 weeks). Center horizontal lines show the medians. Box limits indicate the 25th and 75th percentiles, whiskers extend 1.5 times the interquartile range from the 25th and 75th percentiles.

4.3.6 Structured Illumination Microscopy

Slides were prepared as described in the methods section and stained against CD31. The staining against CD31 depicts inner wall endothelium both of blood vessels and of SC. To facilitate orientation within the sample and to localize the area of interest, cell nuclei were also marked with DAPI. To localize the area of interest in deconvolution microscopy, images were taken using DAPI and tissue autofluorescence.

Figure 26 gives an overview of imaging of SC of a WT animal using conventional deconvolution microscopy and super-resolution 3D-SIM. In Figure 26 A, the image clearly shows a CD31-signal at the endothelia both of SC and a blood vessel in deconvolution microscopy already. After localizing the area of interest, namely SC, focus was placed exclusively on the CD31 signal to fully demonstrate the capabilities of SIM. Consequently, cell structures other than the endothelium are visible only in panel A.

Under B, only the CD31-signal of SC can be seen. Already in the pictures showing an overview of the endothelium of SC, the roughly double increase in resolution is easily visible. When zooming in more closely, this advantage in resolution becomes even

more obvious. The endothelium is now visible as a clearly distinguishable entity with sharp edges instead of appearing blurry and without a clear border.

The images depicted here are reconstructed from a stack of images and are therefore containing information about the depth of the fluorophores as well. Hence, it is even possible to create a 3D-reconstruction of the area visualized (data not shown). In order to visualize this depth-related information, the images in Figure 26 B show that information color-coded, meaning structures at the bottom of the sample appear light blue, towards the middle blue and yellow, and towards the surface in light yellow. Overall, the enhanced contrast and the resolution doubling offered by super-resolution 3D-SIM provides a clearer picture and a much more detailed visualization of anatomical structures.

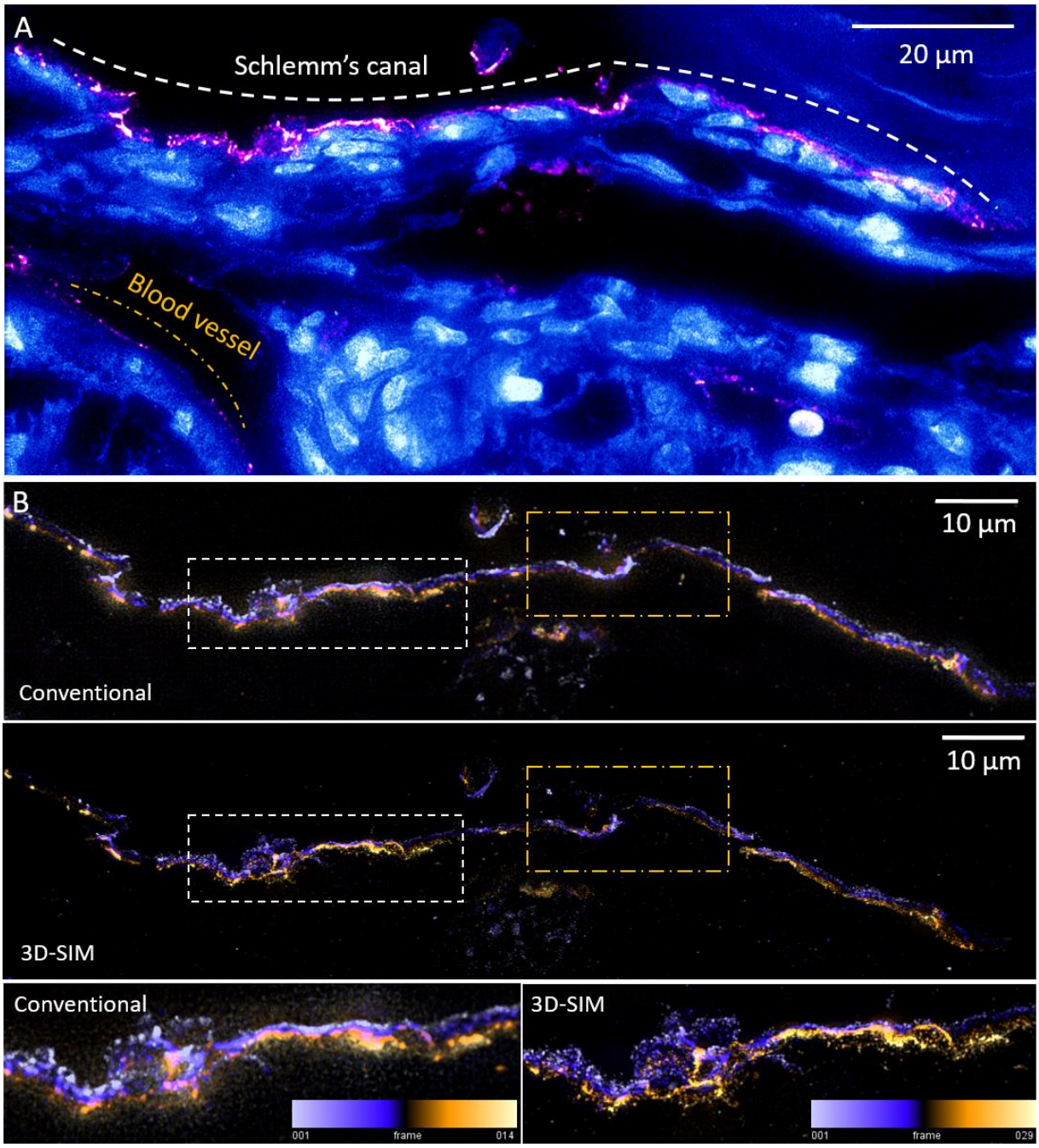

Figure 26 – SIM on SC. A: Deconvolution microscopy of CD31-AF647 (magenta) and DAPI + tissue autofluorescence (blue) providing an overview of the eye tissue morphology with SC and a blood vessel also showing up positive for CD31. The image is a maximum intensity projection of the 3D image stack. B: Comparison of SC imaged using conventional deconvolution microscopy and super-resolution 3D-SIM. The enhanced contrast and resolution doubling offered by 3D-SIM provide a clearer picture. The images are projected with color-coded depth information according to the color bars as they are reconstructed from a stack of several frames (14 frames at 250 nm/frame for the conventional, and 29 frames at 125nm/frame for the 3D-SIM image).

5 Discussion

In summary, this study aimed at validating the impact of CTGF on IOP, axon loss, ECM remodeling, and other related factors in tg and WT mice at 26 and 52 weeks of age in a transgenic mouse model. Furthermore, both an automated axon count with AxonJ was validated as well as a brightness-based objective analysis of microscope pictures in fluorescence microscopy. Finally, SIM-imaging was applied on eyes for the first time. Elevated IOP was observed in tg mice across both age groups. A decrease in IOP was noted with age, which is consistent with previous findings in other mouse strains. Differences in axon numbers were significant at 52 weeks but not at 26 weeks, with lower counts observed compared to previous literature. Fluorescence microscopy confirmed previous findings of increased expression of FN and α-SMA in tg mice, and ECM analysis showed significant differences in ECM-covered areas. SIM provided high-resolution imaging of SC endothelium, offering new research possibilities regarding the visualization of pores. Overall, the tg CTGF construct and its effects proved to be constant also over longer periods of time. Therefore, this model is well able to serve for studying long-term effects, such as the application of medication over longer periods of time.

5.1 Intraocular Pressure Measurements

For mice aged 26 and 52 weeks, IOP measurements demonstrated a statistically significant difference between tg and WT mice. IOP was elevated by 21 to 36% across both age groups, confirming that the previously observed effect of CTGF on IOP persists in older mice.

However, IOP values significantly decreased between 26 and 52 weeks. At 26 weeks, the results aligned with the IOP values reported by Junglas et al. (2012). While exact values differed slightly, the trend of higher IOP in tg compared to WT mice was consistent. By 52 weeks, IOP had further declined in both groups. This decrease might seem counterintuitive, given that glaucoma is generally associated with aging, and IOP is a primary risk factor. However, a decline in IOP with age has been documented in healthy mice from B6, 129P3/J, and C3H/HeJ strains (Savinova et al., 2001). In contrast, C57BL/6 mice show a relatively stable IOP throughout their lifespan (Li et al., 2024; Savinova et al., 2001). To date, no comparative IOP data exist for WT CD1 mice.

In humans, several studies indicate that IOP tends to decrease with age, particularly in large cohorts from Asian populations (Di Zhao et al., 2014; Nakano et al., 2005). Contrarily, some Western studies report an age-related increase in IOP, suggesting that systemic conditions, genetics, or lifestyle-associated factors such as blood pressure and body mass index may contribute to regional differences (David et al., 1987; Shiose, 1990).

The side effects of CTGF may also influence the current findings. CTGF has been implicated in age-related cataract formation (Hwang et al., 2016). To prevent confounding effects from cataracts and glaucoma, mice with cataracts were excluded from the analysis. This could mean that mice with higher CTGF expression were disproportionately removed, contributing to the observed IOP decline at 52 weeks.

Moreover, the mice used in this study are not part of a healthy population; they develop glaucoma at a younger age due to their tg construct. Therefore, a more relevant question is when the tg effects are most pronounced and at what age mice should be assessed for optimal scientific and clinical insights.

The findings suggest that at 26 weeks, IOP values remain comparable to those reported in the literature for 12-week-old mice. Additionally, comparisons with an existing dataset (Junglas et al., 2009) support this conclusion (results not shown). Therefore, for experiments with interventions at a defined point in time, continuing research with 12-week-old mice appears justified regarding IOP. Given this consistency, the model may also serve to observe effects of long-term interventions, such as continuous medication.

5.2 Light and Fluorescence Microscopy and their Objective Analysis

Mice carrying a tg construct that induces lens-specific overexpression of CTGF exhibited more intense staining for both FN and α-SMA compared to their WT littermates in a prior study (Junglas et al., 2012). In this study, FN immunoreactivity in WT mice was limited to a small area adjacent to the inner and outer walls of SC and the stroma of

the ciliary processes. In tg mice, FN staining was more intense and extended from the iris root to the base of the ciliary processes and the sclera near the outer wall of SC.

Differences were also observed for α-SMA. In WT mice, α-SMA was expressed in a few cells within and around the TM, whereas in tg mice, it was present throughout the entire TM and in the stroma of the ciliary body and iris. These findings were confirmed by western blotting in the prior study. The experiments conducted largely replicated these observations, with α-SMA appearing even more widely dispersed in 52-week-old animals.

However, instead of using western blotting, differences in microscope images were quantified by measuring fluorescence brightness. Similar methods have been described in the literature (Smith et al., 2005), with some studies employing more sophisticated image acquisition techniques like time-gated imaging (Su et al., 2022). In glaucoma research, fluorescence brightness analysis has primarily been used for CD44H staining which was used to detect hyaluron in the TM (Knepper, Goossens, & Mayanil, 1998). According to the validation dataset, this method effectively makes visually apparent differences measurable.

Interestingly, this method appears to detect subtler differences. While expert evaluation did not reveal a clear difference between 26-week-old subgroups, fluorescence measurements showed a significant distinction. This suggests that brightness analysis may be particularly useful in large datasets, where visual assessment becomes impractical.

Fluorescence values in 26-week-old mice showed greater variability compared to those at 52 weeks. Interestingly, the overall brightness in 26-week microscopy images was noticeably lower. Although not included in the main results due to the focus on relative brightness, this observation suggests a weaker absolute fluorescence signal at 26 weeks. This finding raises the possibility that increasing exposure time during image acquisition might enhance signal detection by capturing more fluorophores, though this hypothesis requires further structured validation.
In conclusion, prior findings could be successfully replicated for both 26- and 52-week-old mice, confirming them objectively through relative brightness comparison. To fully

validate this method, future studies should correlate fluorescence intensity with protein expression using techniques such as western blotting. Nevertheless, the results indicate that waiting for mice to age may not significantly impact immunohistochemistry-based assessments when relying on visually acquired images. Again, given this consistency in the findings, the model may well serve for observing effects of long-term interventions like long-term medication.

Importantly, the technique developed here is highly usable even with relatively small datasets and does not require thousands of annotated images for training. In contrast, conventional deep learning approaches for biomedical image segmentation, such as U-Net, typically rely on large amounts of training data to achieve high accuracy (Ronneberger, Fischer, & Brox, 2015). This feature makes the method described here particularly suitable for studies where acquiring extensive image datasets is impractical.

5.3 Quantification of Optic Nerve Axons

As glaucoma is defined as chronic neuropathy and gradual loss of axons of retinal ganglion cells, it is well known that axon loss can be found in ON sections, both in glaucoma models in mice (Maddineni et al., 2020) and in human patients (Hernandez, 2000; Weinreb & Khaw, 2004). In this study, manual axon counting revealed a statistically significant difference in axon numbers at 52 weeks of age and across genotypes regardless of age. However, at 26 weeks, no statistically significant difference was observed, despite a reduction in axon numbers in tg mice. Notably, the factor age did not significantly differ between groups, suggesting that the overall observed effect is primarily driven by differences at 52 weeks.

In this study, manual axon counts were consistently lower in tg compared to WT animals at both 26 and 52 weeks, although only the difference at 52 weeks was statistically significant. Also, there was a slight yet not statistically significant difference between both age groups. Overall, our values were notably lower than those reported by Junglas et al. (2012), who found substantially higher axon counts in younger WT and tg mice. Across the literature, typical axon numbers in the optic nerve of mice aged 1–6 months range widely – from approximately 25,000 to 70,000 – depending on factors

such as age and and strain (Anderson et al., 2006; Brambilla et al., 2012; Jeon, Strettoi, & Masland, 1998; Prasov et al., 2012; Templeton et al., 2014; Williams et al., 1996). For CD1 WT mice specifically, Steinhart et al. (2014) reported a decrease from over 50,000 axons at 2 months to just over 40,000 at 12 months.

Therefore, the findings differ from previous literature in two key aspects: First, the absence of a detectable effect at 26 weeks and second, the total axon numbers observed. Regarding the absence of a detectable effect at 26 weeks and comparing this study to prior studies using manual axon counting, particularly Junglas et al. (2012), it is evident that differences between WT and tg animals were detected with small sample sizes (5 vs. 5 per subgroup). Despite a slightly larger cohort in this study (7 vs. 9), a possible effect might have been missed due to sample size limitations. A larger study is recommended to confirm findings at both 26 and 52 weeks, as there is no indication that overlying – such as neuroprotective effects of CTGF – would be present at 26 weeks but vanish at 52 weeks.

Regarding the lower axon numbers observed, there are probably several overlying effects at least partially explaining the findings. Axon loss is influenced by both aging and genetic background. Axon density in the ON is known to decrease with age. CD1 mice show greater axon loss than C57BL/6 and DBA/2J strains, suggesting strain-specific vulnerabilities (Cone et al., 2010). In CD1 mice, older mice lost significantly more axons compared to younger ones (Steinhart et al., 2014). Also in the data from Junglas et al. (2012) there seems to be an age-related decrease in axons especially in tg animals, even though this was not statistically analyzed.

Also, susceptibility to axon loss seems to change with age. Younger DBA/2J and C57BL/6 mice exhibit more pronounced changes in ocular dimensions and axon loss than older counterparts (Cone et al., 2010). Elevated IOP in 2-month-old mice induces axon loss similar to that seen in 10-month-old mice with comparable IOP levels (Inman et al., 2006). This is not in line with the current findings that found the effect of CTGF only in older mice with a comparingly reduced IOP (see above).

Also, possible overlying neuroprotective effects might influence the results of this study. TGF-β1 signaling was shown to possibly protect RGCs from oxidative stress

(Chen et al., 2020). Also crystallins like αB-crystallin were shown to have neuroprotective effects in the TM (Anders et al., 2017; Anders et al., 2018; Liu et al., 2022), with their expression being related to CTGF (Kuespert et al., 2015).

In conclusion, it remains unclear which of the several overlapping and interacting effects influenced the current findings and to what extent. It would be interesting to measure ON counts in WT CD1 mice over a longer period of time as a baseline in order to be able to differentiate between the different influential factors more clearly.

Even though, stating that there is a difference in numbers of ON axons between both genotypes, it overlooks one of the methods that were validated in the present study: automated axon count with AxonJ as described by Zarei et al. (2016a, 2016b). AxonJ has been described as being as reliable as manual counting, with the primary advantage of saving time, but also avoiding a possible bias due to axon density variations in manual sectioned counting.

The findings raise concerns about the reliability of AxonJ. At 26 weeks, the generated values are characterized by a number of statistically significant outliers, unlike the data from 52-week-old mice. However, a reliable method should assess any given ON section equally, without arbitrary exclusions. Furthermore, AxonJ systematically counted more axons than manual counting: The mean counted in AxonJ is 48542, compared to 32621 in manual count. As discussed above, the values counted by AxonJ would be closer to previously reported axon counts. However, closer inspection revealed that AxonJ misidentified non-axonal structures as axons (see Figure 21), potentially explaining the elevated numbers. The reason for the misidentification could be that AxonJ was validated using 40x images, whereas this study relies on 100x images. As the author is not familiar with the underlying image analysis algorithms, further examination of this question must be left to a software expert. It is strongly recommended to use manual axon counting as a reliable baseline in future studies and to compare it with AxonJ results if needed. Importantly, while AxonJ illustrates the limitations of traditional automated tools, the future of axon quantification probably lies in image analysis methods based on neural networks, such as AxonDeep, which provide higher accuracy, consistency, and full pixel-wise segmentation (Deng et al., 2021).

To further assess AxonJ, consecutive slides from the same ON could be analyzed. These slides would have the same number of axons as they derive from one animal and one ON, ensuring consistency. However, evaluating AxonJ's potential was beyond the scope of this study, leaving this question for future research.

5.4 Measurement of Extracellular Matrix-Covered, Extracellular Matrix-Free and Areas Covered by Cells in Electron Microscopy

POAG is characterized by significant structural and cellular changes in the TM, observable by the use of EM. These changes collectively contribute to impaired AH drainage and increased IOP, which are hallmarks of the disease. This includes ECM alterations especially in the ICA. These play a key role in POAG pathophysiology, with MMPs being central regulators. Changes in MMP activity drive ECM remodeling in glaucoma, with TGF-β2 promoting ECM deposition and altering MMP activity, leading to pathological ECM. This has been observed in both experimental models and human glaucoma tissues (Groef et al., 2013; Reinhard et al., 2021; Vranka et al., 2015).

Also, the cellularity in the TM is undergoing changes in POAG. There is a marked loss of TM cells, leading to fusion and thickening of trabecular lamellae (Tektas & Lütjen-Drecoll, 2009).TM cellularity declines more rapidly in glaucomatous patients than in nonglaucomatous individuals, with inner tissues being most affected and outermost tissues least affected (Alvarado, Murphy, & Juster, 1984).

In the present study, the area covered by cells remained nearly constant across ages and genotypes. This is in line with the just described pathomechanism. Consequently, ECM-covered and ECM-free areas likely correlate inversely. Statistically significant differences were observed in ECM-covered and ECM-free areas between 26- and 52-week-old mice, as well as between WT and tg mice overall. However, at 52 weeks, ECM coverage was not significantly different, while ECM-free area remained significantly altered. Regarding the indirect correlation described above and given the small sample size (5 vs. 5), this result may reflect limited statistical power rather than an actual absence of effect. A larger cohort is needed for further verification.

Again, ageing did not seem to influence the findings, with only the ECM-free area showing a tendency towards possible significance. Thus, assessing mice at younger ages may be sufficient for evaluating ECM-related changes, but as above, given the consistency in the findings also at older age, the model may well serve for observing effects of long-term interventions like long-term medication.

5.5 Structured Illumination Microscopy

SIM (Gustafsson, 2000; Gustafsson et al., 2008; Heintzmann & Huser, 2017) was successfully applied to whole-eye tissue slides for the first time, offering high-resolution imaging capabilities. While SIM has previously been used to analyze retinal cells (Ach et al., 2012), its application to entire eye sections opens new research possibilities.

One promising application is the assessment of pores in SC endothelium. These pores range from 0.1 to 3 µm in diameter (Johnson, 2006) with an average diameter ranging from 0.40 µm to 0.67 µm (Braakman et al., 2014). The pores serve as a blood-aqueous barrier and prevent blood and serum proteins from entering back into the eye while facilitating AH outflow (Braakman et al., 2015). They can be classified into two types: transcellular “I” pores, which pass directly through SC cells, and paracellular “B” pores, which pass between neighboring SC cells (Ethier et al., 1998).

Some studies have observed that these pores and giant vacuoles appear both more frequently and prominently in perfusion-fixed tissues compared to immersion-fixed tissues, which raised concerns about them being mostly artifacts. The explanation could be that fixation by perfusion mimics physiological IOP, potentially preserving features like giant vacuoles and pores, while immersion fixation may lead to collapse or distortion of these structures. Research comparing immersion and perfusion fixation supports this interpretation, noting that pores such as I-pores were more apparent in perfusion-fixed eyes, whereas immersion-fixed samples showed fewer or no such pores (Lai et al., 2019; Swain et al., 2022).

Serial block-face scanning EM and advanced 3D reconstruction techniques have further validated the existence of these structures under near-physiological conditions, reducing the likelihood that all observed pores are artefacts. However, some features,

like rough or jagged edges in pore openings, have been identified as artefactual, often attributable to sectioning or sample preparation during EM studies (Swain et al., 2022).

SIM's resolution is sufficient to visualize these pores using immunohistochemistry, offering an alternative to EM for their analysis. This presents exciting opportunities for future research, though a detailed investigation would be beyond the scope of this thesis.

5.6 Crossbreeding

The crossbreeding was not finished at the time this thesis was written. Data was too limited also for statistical analysis (results not shown). Up to now, only the IOP values of mice up to generation four (BALB/c-crossbreeding) and seven (C57BL/6J-crossbreeding) are available as the breeding still takes some time to be finished.

Eyes and ONs were preserved after every IOP measurement at 12 weeks, so they are ready to be assessed in another thesis. As this study has validated some possible methods that could be used for studying the differences, I hope to have laid the basis for a detailed and straight forward analysis of the effects of CTGF in the BALB/c and C57/BI6J mouse strains.

6 Summary

Glaucoma is the main reason for irreversible blindness in humans. It is defined as a chronic neuropathy of the ON, characterized by the subsequent loss of RGC axons. Previous research established a tg mouse model based on a lense-specific overexpression of CTGF. This mouse model mimics pathological changes that are present in glaucomatous patients, such as changes in IOP, changes in cellular stiffness and deployment of ECM in regions that are relevant to the outflow of AH and therefore to the regulation of IOP, and loss of axons of RGCs. This thesis aimed at validating the above mouse model under different conditions for glaucoma research, especially in older age at 26 and 52 weeks and in different mouse strains, namely BALB/c and C57BL/6J.

IOP measurements were performed, and mice eyes were assessed using EM and immunohistochemical stainings. The analysis aimed to be objective by measuring surfaces covered with or free of ECM in EM samples and quantifying brightness in fluorescence microscopy images. Axon counts were conducted both manually and automatically. Additionally, samples were prepared for evaluation using SIM.

Key findings demonstrated that IOP measurements, manual axon counts, changes in the deployment of ECM detectable by EM and fluorescence intensity analysis indicate significant differences between tg and WT mice aged 26 and 52 weeks. A transfer of the tg construct to different background strains (C57BL/6J and BALB/c) was begun but partly pending at the time of completion of this thesis.

Comparing the brightness of images acquired through fluorescence microscopy instead of comparing them by expert opinion only proved to be reliable. A protocol for analyzing samples with SIM that breaches the known limits of optical microscopy could be established. Automated axon counting instead of manual counting, however, proved to be problematic. Automated counting, though more efficient, produced elevated and sometimes unreliable results, warranting further assessment before widespread adoption.

Overall, this thesis provides essential validation for using this tg mouse model in glaucoma research also at older age, showing the consistency of the effects over time, and explores the strengths and weaknesses of different image analysis techniques.

7 References

Abraham, D. (2008). Connective tissue growth factor: Growth factor, matricellular organizer, fibrotic biomarker or molecular target for anti-fibrotic therapy in SSc? *Rheumatology (Oxford, England)*, *47 Suppl 5*, v8-9. https://doi.org/10.1093/rheumatology/ken278

Abreu, J. G., Ketpura, N. I., Reversade, B., & Robertis, E. M. de (2002). Connective-tissue growth factor (CTGF) modulates cell signalling by BMP and TGF-β. *Nature Cell Biology*, *4*(8), 599–604. https://doi.org/10.1038/ncb826

Abu-Hassan, D. W., Acott, T. S., & Kelley, M. J. (2014). The Trabecular Meshwork: A Basic Review of Form and Function. *Journal of Ocular Biology*, *2*(1).

Ach, T., Best, G., Rossberger, S., Heintzmann, R., Cremer, C., & Dithmar, S. (2012). Autofluorescence imaging of human RPE cell granules using structured illumination microscopy. *The British Journal of Ophthalmology*, *96*(8), 1141–1144. https://doi.org/10.1136/bjophthalmol-2012-301547

Acott, T. S., Samples, J. R., Bradley, J. M., Bacon, D. R., Bylsma, S. S., & van Buskirk, E. M. (1989). Trabecular repopulation by anterior trabecular meshwork cells after laser trabeculoplasty. *American Journal of Ophthalmology*, *107*(1), 1–6. https://doi.org/10.1016/0002-9394(89)90805-2

Acott, T. S., & Kelley, M. J. (2008). Extracellular matrix in the trabecular meshwork. *Experimental Eye Research*, *86*(4), 543–561. https://doi.org/10.1016/j.exer.2008.01.013

Agarwal, P., Daher, A. M., & Agarwal, R. (2015). Aqueous humor TGF-β2 levels in patients with open-angle glaucoma: A meta-analysis. *Molecular Vision*, *21*, 612–620.

The AGIS Investigators (2000). The advanced glaucoma intervention study, 6: Effect of cataract on visual field and visual acuity. The AGIS Investigators. *Archives of Ophthalmology (Chicago, Ill. : 1960)*, *118*(12), 1639–1652.

Albon, J., Purslow, P. P., Karwatowski, W. S., & Easty, D. L. (2000). Age related compliance of the lamina cribrosa in human eyes. *The British Journal of Ophthalmology*, *84*(3), 318–323.

Alvarado, J., Murphy, C., & Juster, R. (1984). Trabecular meshwork cellularity in primary open-angle glaucoma and nonglaucomatous normals. *Ophthalmology*, *91*(6), 564–579. https://doi.org/10.1016/S0161-6420(84)34248-8

Anders, F., Liu, A., Mann, C., Teister, J., Lauzi, J., Thanos, S., . . . Prokosch, V. (2017). The Small Heat Shock Protein α-Crystallin B Shows Neuroprotective Properties in a Glaucoma Animal Model. *International Journal of Molecular Sciences*, *18*(11). https://doi.org/10.3390/ijms18112418

Anders, F., Mann, C., Liu, A., Teister, J., Funke, S., Thanos, S., . . . Prokosch, V. (2018). Correlation of Crystallin Expression and RGC Susceptibility in Experimental Glaucoma Rats of Different Ages. *Current Eye Research*, *43*(10), 1267–1273. https://doi.org/10.1080/02713683.2018.1485950

Anderson, M. G., Libby, R. T., Mao, M., Cosma, I. M., Wilson, L. A., Smith, R. S., & John, S. W. M. (2006). Genetic context determines susceptibility to intraocular

pressure elevation in a mouse pigmentary glaucoma. *BMC Biology*, *4*, 20. https://doi.org/10.1186/1741-7007-4-20

Anderson, N. H. (1960). On Teaching F Instead of t. *The Journal of Experimental Education*, *28*(3), 261–263. https://doi.org/10.1080/00220973.1960.11010659

Arnison, M. R., & Sheppard, C. J. (2002). A 3D vectorial optical transfer function suitable for arbitrary pupil functions. *Optics Communications*, *211*(1-6), 53–63. https://doi.org/10.1016/S0030-4018(02)01857-6

Babizhayev, M. A., & Brodskaya, M. W. (1989). Fibronectin detection in drainage outflow system of human eyes in ageing and progression of open-angle glaucoma. *Mechanisms of Ageing and Development*, *47*(2), 145–157. https://doi.org/10.1016/0047-6374(89)90017-1

Bartholin, L., Wessner, L. L., Chirgwin, J. M., & Guise, T. A. (2007). The human Cyr61 gene is a transcriptional target of transforming growth factor beta in cancer cells. *Cancer Letters*, *246*(1-2), 230–236. https://doi.org/10.1016/j.canlet.2006.02.019

Bill, A., & Phillips, C. I. (1971). Uveoscleral drainage of aqueous humour in human eyes. *Experimental Eye Research*, *12*(3), 275–281. https://doi.org/10.1016/0014-4835(71)90149-7

Bill, A., & Svedbergh, B. (1972). Scanning electron microscopic studies of the trabecular meshwork and the canal of Schlemm--an attempt to localize the main resistance to outflow of aqueous humor in man. *Acta Ophthalmologica*, *50*(3), 295–320. https://doi.org/10.1111/j.1755-3768.1972.tb05954.x

Braakman, S. T., Moore, J. E., Ethier, C. R., & Overby, D. R. (2015). Transport across Schlemm's canal endothelium and the blood-aqueous barrier. *Experimental Eye Research*, *146*, 17–21. https://doi.org/10.1016/j.exer.2015.11.026

Braakman, S. T., Pedrigi, R. M., Read, A. T., Smith, J. A. E., Stamer, W. D., Ethier, C. R., & Overby, D. R. (2014). Biomechanical strain as a trigger for pore formation in Schlemm's canal endothelial cells. *Experimental Eye Research*, *127*, 224–235. https://doi.org/10.1016/j.exer.2014.08.003

Bradham, D. M., Igarashi, A., Potter, R. L., & Grotendorst, G. R. (1991). Connective tissue growth factor: A cysteine-rich mitogen secreted by human vascular endothelial cells is related to the SRC-induced immediate early gene product CEF-10. *The Journal of Cell Biology*, *114*(6), 1285–1294. https://doi.org/10.1083/jcb.114.6.1285

Bradley, J. M. B., Vranka, J., Colvis, C. M., Conger, D. M., Alexander, J. P., Fisk, A. S., . . . Acott, T. (1998). Effect of matrix metalloproteinases activity on outflow in perfused human organ culture. *Investigative Ophthalmology and Visual Science*, *39*(13), 2649–2658.

Brambilla, R., Dvoriantchikova, G., Barakat, D., Ivanov, D., Bethea, J. R., & Shestopalov, V. I. (2012). Transgenic inhibition of astroglial NF-κB protects from optic nerve damage and retinal ganglion cell loss in experimental optic neuritis. *Journal of Neuroinflammation*, *9*, 213. https://doi.org/10.1186/1742-2094-9-213

Braunger, B. M., Pielmeier, S., Demmer, C., Landstorfer, V., Kawall, D., Abramov, N., . . . Tamm, E. R. (2013). TGF-β Signaling Protects Retinal Neurons from Programmed Cell Death during the Development of the Mammalian Eye.

Journal of Neuroscience, *33*(35), 14246–14258. https://doi.org/10.1523/JNEUROSCI.0991-13.2013

Chaqour, B., Yang, R., & Sha, Q. (2006). Mechanical stretch modulates the promoter activity of the profibrotic factor CCN2 through increased actin polymerization and NF-kappaB activation. *The Journal of Biological Chemistry*, *281*(29), 20608–20622. https://doi.org/10.1074/jbc.M600214200

Chen, C. C., Chen, N., & Lau, L. F. (2001). The angiogenic factors Cyr61 and connective tissue growth factor induce adhesive signaling in primary human skin fibroblasts. *The Journal of Biological Chemistry*, *276*(13), 10443–10452. https://doi.org/10.1074/jbc.M008087200

Chen, H.-Y., Ho, Y.-J., Chou, H.-C., Liao, E.-C., Tsai, Y.-T., Wei, Y.-S., . . . Chan, H.-L. (2020). Tgf-β1 signaling protects retinal ganglion cells from oxidative stress via modulation of the HO-1/Nrf2 pathway. *Chemico-Biological Interactions*, *331*, 109249. https://doi.org/10.1016/j.cbi.2020.109249

Clark, D. A., & Coker, R. (1998). Molecules in focus Transforming growth factor-beta (TGF-β). *The International Journal of Biochemistry & Cell Biology*, *30*(3), 293–298. https://doi.org/10.1016/S1357-2725(97)00128-3

Clement Freiberg, J., Spreckelsen, A. von, Kolko, M., Azuara-Blanco, A., & Virgili, G. (2022). Rho kinase inhibitor for primary open-angle glaucoma and ocular hypertension. *The Cochrane Database of Systematic Reviews*, *6*(6), CD013817. https://doi.org/10.1002/14651858.CD013817.pub2

Collaborative Normal-Tension Glaucoma Study Group (1998). Comparison of glaucomatous progression between untreated patients with normal-tension glaucoma and patients with therapeutically reduced intraocular pressures. Collaborative Normal-Tension Glaucoma Study Group. *American Journal of Ophthalmology*, *126*(4), 487–497.

Coltharp, C., & Xiao, J. (2012). Superresolution microscopy for microbiology. *Cellular Microbiology*, *14*(12), 1808–1818. https://doi.org/10.1111/cmi.12024

Cone, F. E., Gelman, S. E., Son, J. L., Pease, M. E., & Quigley, H. A. (2010). Differential susceptibility to experimental glaucoma among 3 mouse strains using bead and viscoelastic injection. *Experimental Eye Research*, *91*(3), 415–424. https://doi.org/10.1016/j.exer.2010.06.018

Conlon, R., Saheb, H., & Ahmed, I. I. K. (2017). Glaucoma treatment trends: A review. *Canadian Journal of Ophthalmology. Journal Canadien D'ophtalmologie*, *52*(1), 114–124. https://doi.org/10.1016/j.jcjo.2016.07.013

David, R., Zangwill, L., Stone, D., & Yassur, Y. (1987). Epidemiology of intraocular pressure in a population screened for glaucoma. *The British Journal of Ophthalmology*, *71*(10), 766–771. https://doi.org/10.1136/bjo.71.10.766

Deng, W., Hedberg-Buenz, A., Soukup, D. A., Taghizadeh, S., Wang, K., Anderson, M. G., & Garvin, M. K. (2021). AxonDeep: Automated Optic Nerve Axon Segmentation in Mice With Deep Learning. *Translational vision science & technology*, *10*(14), 22. https://doi.org/10.1167/tvst.10.14.22

Di Zhao, Kim, M. H., Pastor-Barriuso, R., Chang, Y., Ryu, S., Zhang, Y., . . . Cho, J. (2014). A longitudinal study of age-related changes in intraocular pressure: The

Kangbuk Samsung Health Study. *Investigative Ophthalmology & Visual Science*, *55*(10), 6244–6250. https://doi.org/10.1167/iovs.14-14151

Dobolyi, A., Vincze, C., Pál, G., & Lovas, G. (2012). The neuroprotective functions of transforming growth factor beta proteins. *International Journal of Molecular Sciences*, *13*(7), 8219–8258. https://doi.org/10.3390/ijms13078219

Downs, J. C. (2003). Viscoelastic Characterization of Peripapillary Sclera: Material Properties by Quadrant in Rabbit and Monkey Eyes. *The British Journal of Ophthalmology*, *125*(1), 124. https://doi.org/10.1115/1.1536930

Downs, J. C., & Girkin, C. A. (2017). Lamina cribrosa in glaucoma. *Current Opinion in Ophthalmology*, *28*(2), 113–119. https://doi.org/10.1097/ICU.0000000000000354

Edlund, S., Landström, M., Heldin, C.-H., & Aspenström, P. (2002). Transforming growth factor-beta-induced mobilization of actin cytoskeleton requires signaling by small GTPases Cdc42 and RhoA. *Molecular Biology of the Cell*, *13*(3), 902–914. https://doi.org/10.1091/mbc.01-08-0398

Ethier, C. R., Coloma, F. M., Sit, A. J., & Johnson, M. (1998). Two pore types in the inner-wall endothelium of Schlemm's canal. *Investigative Ophthalmology & Visual Science*, *39*(11), 2041–2048.

Ethier, C. R. (2002). The inner wall of Schlemm's canal. *Experimental Eye Research*, *74*(2), 161–172. https://doi.org/10.1006/exer.2002.1144

Flaxman, S. R., Bourne, R. R. A., Resnikoff, S., Ackland, P., Braithwaite, T., Cicinelli, M. V., . . . Taylor, H. R. (2017). Global causes of blindness and distance vision impairment 1990-2020: A systematic review and meta-analysis. *The Lancet. Global Health*, *5*(12), e1221-e1234. https://doi.org/10.1016/S2214-109X(17)30393-5

Foster, P. J., Buhrmann, R., Quigley, H. A., & Johnson, G. J. (2002). The definition and classification of glaucoma in prevalence surveys. *The British Journal of Ophthalmology*, *86*(2), 238–242.

Frazier, K., Williams, S., Kothapalli, D., Klapper, H., & Grotendorst, G. R. (1996). Stimulation of fibroblast cell growth, matrix production, and granulation tissue formation by connective tissue growth factor. *The Journal of Investigative Dermatology*, *107*(3), 404–411.

Fuchshofer, R., Birke, M., Welge-Lüssen, U., Kook, D., & Lütjen-Drecoll, E. (2005). Transforming growth factor-beta 2 modulated extracellular matrix component expression in cultured human optic nerve head astrocytes. *Investigative Ophthalmology & Visual Science*, *46*(2), 568–578. https://doi.org/10.1167/iovs.04-0649

Fuchshofer, R., & Tamm, E. R. (2009). Modulation of extracellular matrix turnover in the trabecular meshwork. *Experimental Eye Research*, *88*(4), 683–688. https://doi.org/10.1016/j.exer.2009.01.005

Fuchshofer, R., Welge-Lüssen, U., & Lütjen-Drecoll, E. (2003). The effect of TGF-β2 on human trabecular meshwork extracellular proteolytic system. *Experimental Eye Research*, *77*(6), 757–765. https://doi.org/10.1016/S0014-4835(03)00220-3

Galbraith, C. G., & Galbraith, J. A. (2011). Super-resolution microscopy at a glance. *Journal of Cell Science*, *124*(Pt 10), 1607–1611. https://doi.org/10.1242/jcs.080085

Gao, R., & Brigstock, D. R. (2004). Connective tissue growth factor (CCN2) induces adhesion of rat activated hepatic stellate cells by binding of its C-terminal domain to integrin alpha(v)beta(3) and heparan sulfate proteoglycan. *The Journal of Biological Chemistry*, *279*(10), 8848–8855. https://doi.org/10.1074/jbc.M313204200

Garg, A., Hood, D. C., Pensec, N., Liebmann, J. M., & Blumberg, D. M. (2018). Macular Damage, as Determined by Structure-Function Staging, is Associated with Worse Vision-Related Quality of Life in Early Glaucoma. *American Journal of Ophthalmology, 194*, 88–94. https://doi.org/10.1016/j.ajo.2018.07.011

Gong, H., Tripathi, R. C., & Tripathi, B. J. (1996). Morphology of the aqueous outflow pathway. *Microscopy Research and Technique*, *33*(4), 336–367. https://doi.org/10.1002/(SICI)1097-0029(19960301)33:4<336::AID-JEMT4>3.0.CO;2-N

Gordon, M. O., Beiser, J. A., Brandt, J. D., Heuer, D. K., Higginbotham, E. J., Johnson, C. A., . . . Kass, M. A. (2002). The Ocular Hypertension Treatment Study: Baseline factors that predict the onset of primary open-angle glaucoma. *Archives of Ophthalmology (Chicago, Ill. : 1960)*, *120*(6), 714-20; discussion 829-30.

Gottanka J., Johnson, D. H., Martus P., & Lütjen-Drecoll, E. (April 1997). Severity of Optic Nerve Damage in Eyes with POAG Is Correlated with Changes in the Trabecular Meshwork. *Journal of Glaucoma*, *6*(2), 123–132.

Groef, L. de, van Hove, I., Dekeyster, E., Stalmans, I., & Moons, L. (2013). MMPs in the trabecular meshwork: Promising targets for future glaucoma therapies? *Investigative Ophthalmology & Visual Science*, *54*(12), 7756–7763. https://doi.org/10.1167/iovs.13-13088

Grotendorst, G. R., Okochi, H., & Hayashi, N. (1996). A novel transforming growth factor beta response element controls the expression of the connective tissue growth factor gene. *Cell Growth & Differentiation : The Molecular Biology Journal of the American Association for Cancer Research*, *7*(4), 469–480.

Gustafsson, M. G. (1999). Extended resolution fluorescence microscopy. *Current Opinion in Structural Biology*, *9*(5), 627–634. https://doi.org/10.1016/s0959-440x(99)00016-0

Gustafsson, M. G. (2000). Surpassing the lateral resolution limit by a factor of two using structured illumination microscopy. *Journal of Microscopy*, *198*(Pt 2), 82–87. https://doi.org/10.1046/j.1365-2818.2000.00710.x

Gustafsson, M. G. L., Shao, L., Carlton, P. M., Wang, C. J. R., Golubovskaya, I. N., Cande, W. Z., . . . Sedat, J. W. (2008). Three-dimensional resolution doubling in wide-field fluorescence microscopy by structured illumination. *Biophysical Journal*, *94*(12), 4957–4970. https://doi.org/10.1529/biophysj.107.120345

Harten, U. (2017). *Physik für Mediziner* (15., überarbeitete Auflage). *Springer-Lehrbuch*. Berlin, Heidelberg. https://doi.org/10.1007/978-3-662-54447-1

Hashimoto, G., Inoki, I., Fujii, Y., Aoki, T., Ikeda, E., & Okada, Y. (2002). Matrix metalloproteinases cleave connective tissue growth factor and reactivate angiogenic activity of vascular endothelial growth factor 165. *The Journal of Biological Chemistry*, *277*(39), 36288–36295. https://doi.org/10.1074/jbc.M201674200

Heintzmann, R., & Huser, T. (2017). Super-Resolution Structured Illumination Microscopy. *Chemical Reviews*, *117*(23), 13890–13908. https://doi.org/10.1021/acs.chemrev.7b00218

Hernandez, M. R. (2000). The optic nerve head in glaucoma: Role of astrocytes in tissue remodeling. *Progress in Retinal and Eye Research*, *19*(3), 297–321. https://doi.org/10.1016/s1350-9462(99)00017-8

Hernandez, M. R., Igoe, F., & Neufeld, A. H. (1988). Cell culture of the human lamina cribrosa. *Investigative Ophthalmology & Visual Science*, *29*(1), 78–89.

Heusinger-Ribeiro, J., Eberlein, M., Wahab, N. A., & Goppelt-Struebe, M. (2001). Expression of connective tissue growth factor in human renal fibroblasts: Regulatory roles of RhoA and cAMP. *Journal of the American Society of Nephrology : JASN*, *12*(9), 1853–1861.

Holmes, A., Abraham, D. J., Sa, S., Shiwen, X., Black, C. M., & Leask, A. (2001). CTGF and SMADs, maintenance of scleroderma phenotype is independent of SMAD signaling. *The Journal of Biological Chemistry*, *276*(14), 10594–10601. https://doi.org/10.1074/jbc.M010149200

Hwang, H. B., Yim, H. B., Cho, Y. K., & Choi, J. A. (2016). The Association Between Aqueous Connective Tissue Growth Factor and the Severity of Age-related Cataracts as Graded by the Lens Opacities Classification System III. *Current Eye Research*, *41*(3), 350–356. https://doi.org/10.3109/02713683.2015.1082601

Igarashi, A., Okochi, H., Bradham, D. M., & Grotendorst, G. R. (1993). Regulation of connective tissue growth factor gene expression in human skin fibroblasts and during wound repair. *Molecular Biology of the Cell*, *4*(6), 637–645. https://doi.org/10.1091/mbc.4.6.637

Inatani, M., Tanihara, H., Katsuta, H., Honjo, M., Kido, N., & Honda, Y. (2001). Transforming growth factor-beta 2 levels in aqueous humor of glaucomatous eyes. *Graefe's Archive for Clinical and Experimental Ophthalmology = Albrecht Von Graefes Archiv Für Klinische Und Experimentelle Ophthalmologie*, *239*(2), 109–113. https://doi.org/10.1007/s004170000241

Inman, D. M., Sappington, R. M., Horner, P. J., & Calkins, D. J. (2006). Quantitative correlation of optic nerve pathology with ocular pressure and corneal thickness in the DBA/2 mouse model of glaucoma. *Investigative Ophthalmology and Visual Science*, *47*(3), 986–996. https://doi.org/10.1167/iovs.05-0925

Iwamoto, Y., & Tamura, M. (1988). Immunocytochemical study of intermediate filaments in cultured human trabecular cells. *Investigative Ophthalmology & Visual Science*, *29*(2), 244–250.

Jampel, H. D., Roche, N., Stark, W. J., & Roberts, A. B. (1990). Transforming growth factor-beta in human aqueous humor. *Current Eye Research*, *9*(10), 963–969. https://doi.org/10.3109/02713689009069932

Jedsadayanmata, A., Chen, C. C., Kireeva, M. L., Lau, L. F., & Lam, S. C. (1999). Activation-dependent adhesion of human platelets to Cyr61 and Fisp12/mouse connective tissue growth factor is mediated through integrin alpha(IIb)beta(3). *The Journal of Biological Chemistry*, *274*(34), 24321–24327. https://doi.org/10.1074/jbc.274.34.24321

Jeon, C.-J., Strettoi, E., & Masland, R. H. (1998). The Major Cell Populations of the Mouse Retina. *The Journal of Neuroscience : The Official Journal of the Society for Neuroscience*, *18*(21), 8936–8946. https://doi.org/10.1523/JNEUROSCI.18-21-08936.1998

Johnson, M., Shapiro, A., Ethier, C. R., & Kamm, R. D. (1992). Modulation of outflow resistance by the pores of the inner wall endothelium. *Investigative Ophthalmology and Visual Science*, *33*(5), 1670–1675.

Johnson, M. (2006). What controls aqueous humour outflow resistance?. *Experimental Eye Research*, *82*(4), 545–557. https://doi.org/10.1016/j.exer.2005.10.011

Junglas, B., Kuespert, S., Seleem, A. A., Struller, T., Ullmann, S., Bösl, M., . . . Fuchshofer, R. (2012). Connective tissue growth factor causes glaucoma by modifying the actin cytoskeleton of the trabecular meshwork. *The American Journal of Pathology*, *180*(6), 2386–2403. https://doi.org/10.1016/j.ajpath.2012.02.030

Junglas, B., Yu, A. H. L., Welge-Lüssen, U., Tamm, E. R., & Fuchshofer, R. (2009). Connective tissue growth factor induces extracellular matrix deposition in human trabecular meshwork cells. *Experimental Eye Research*, *88*(6), 1065–1075. https://doi.org/10.1016/j.exer.2009.01.008

Kang, J. M., & Tanna, A. P. (2021). Glaucoma. *The Medical Clinics of North America*, *105*(3), 493–510. https://doi.org/10.1016/j.mcna.2021.01.004

Kaye, G. W. C., & Laby, T. H. (1995). *Tables of physical and chemical constants* (16. ed.). Harlow: Longman.

Kiel, J. W. (2010). *The Ocular Circulation*. San Rafael (CA): Morgan & Claypool Life Sciences. https://doi.org/10.4199/C00024ED1V01Y201012ISP012

Knepper, P. A., Goossens, W., & Mayanil, C. S. (1998). CD44H localization in primary open-angle glaucoma. *Investigative Ophthalmology and Visual Science*, *39*(5), 673–680.

Kottler, U. B., Jünemann, A. G. M., Aigner, T., Zenkel, M., Rummelt, C., & Schlötzer-Schrehardt, U. (2005). Comparative effects of TGF-beta 1 and TGF-beta 2 on extracellular matrix production, proliferation, migration, and collagen contraction of human Tenon's capsule fibroblasts in pseudoexfoliation and primary open-angle glaucoma. *Experimental Eye Research*, *80*(1), 121–134. https://doi.org/10.1016/j.exer.2004.08.018

Kuespert, S., Junglas, B., Braunger, B. M., Tamm, E. R., & Fuchshofer, R. (2015). The regulation of connective tissue growth factor expression influences the viability of human trabecular meshwork cells. *Journal of Cellular and Molecular Medicine*, *19*(5), 1010–1020. https://doi.org/10.1111/jcmm.12492

Kumar, S., Ichhpujani, P., Singh, R., Thakur, S., Sharma, M., & Nagpal, N. (2018). The impact of primary open-angle glaucoma: Quality of life in Indian patients. *Indian Journal of Ophthalmology*, *66*(3), 416–419. https://doi.org/10.4103/ijo.IJO_847_17

Kwon, Y. H., Fingert, J. H., Kuehn, M. H., & Alward, W. L. M. (2009). Primary open-angle glaucoma. *The New England Journal of Medicine*, *360*(11), 1113–1124. https://doi.org/10.1056/NEJMra0804630

Lai, J., Su, Y., Swain, D. L., Huang, D., Getchevski, D., & Gong, H. (2019). The Role of Schlemm's Canal Endothelium Cellular Connectivity in Giant Vacuole Formation: A 3D Electron Microscopy Study. *Investigative Ophthalmology & Visual Science*, *60*(5), 1630–1643. https://doi.org/10.1167/iovs.18-26011

Lang, G. K. (2019). *Augenheilkunde*. Stuttgart: Georg Thieme Verlag. https://doi.org/10.1055/b-006-163269

Leite, M. T., Sakata, L. M., & Medeiros, F. A. (2011). Managing Glaucoma In Developing Countries. *Arquivos Brasileiros De Oftalmologia*, *74*(2), 83–84.

Li, G., van Batenburg-Sherwood, J., Safa, B. N., Fraticelli Guzmán, N. S., Wilson, A., Bahrani Fard, M. R., . . . Stamer, W. D. (2024). Aging and intraocular pressure homeostasis in mice. *Aging Cell*, e14160. https://doi.org/10.1111/acel.14160

Lichter, P. R., Musch, D. C., Gillespie, B. W., Guire, K. E., Janz, N. K., Wren, P. A., & Mills, R. P. (2001). Interim clinical outcomes in the Collaborative Initial Glaucoma Treatment Study comparing initial treatment randomized to medications or surgery. *Ophthalmology*, *108*(11), 1943–1953.

Lipson, K. E., Wong, C., Teng, Y., & Spong, S. (2012). CTGF is a central mediator of tissue remodeling and fibrosis and its inhibition can reverse the process of fibrosis. *Fibrogenesis & Tissue Repair*, *5*(Suppl 1), S24. https://doi.org/10.1186/1755-1536-5-S1-S24

Liu, H., Bell, K., Herrmann, A., Arnhold, S., Mercieca, K., Anders, F., . . . Prokosch, V. (2022). Crystallins Play a Crucial Role in Glaucoma and Promote Neuronal Cell Survival in an In Vitro Model Through Modulating Müller Cell Secretion. *Investigative Ophthalmology & Visual Science*, *63*(8), 3. https://doi.org/10.1167/iovs.63.8.3

Loeys, B. L., Schwarze, U., Holm, T., Callewaert, B. L., Thomas, G. H., Pannu, H., . . . Dietz, H. C. (2006). Aneurysm syndromes caused by mutations in the TGF-beta receptor. *The New England Journal of Medicine*, *355*(8), 788–798. https://doi.org/10.1056/NEJMoa055695

Lütjen-Drecoll, E. (1999). Functional morphology of the trabecular meshwork in primate eyes. *Progress in Retinal and Eye Research*, *18*(1), 91–119.

Lütjen-Drecoll, E., Futa, R., & Rohen, J. W. (1981). Ultrahistochemical studies on tangential sections of the trabecular meshwork in normal and glaucomatous eyes. *Investigative Ophthalmology & Visual Science*, *21*(4), 563–573.

Lütjen-Drecoll E & Rohen J. W. (2001). *Functional morphology of the trabecular meshwork. In: Tasman W, Jaeger EA, editors. Duane's foundations of clinical ophthalmology.* Philadelphia: JB Lippincott.

Macknight, A. D., McLaughlin, C. W., Peart, D., Purves, R. D., Carré, D. A., & Civan, M. M. (2000). Formation of the aqueous humor. *Clinical and Experimental Pharmacology & Physiology*, *27*(1-2), 100–106. https://doi.org/10.1046/j.1440-1681.2000.03208.x

Maddineni, P., Kasetti, R. B., Patel, P. D., Millar, J. C., Kiehlbauch, C., Clark, A. F., & Zode, G. S. (2020). CNS axonal degeneration and transport deficits at the optic nerve head precede structural and functional loss of retinal ganglion cells in a mouse model of glaucoma. *Molecular Neurodegeneration*, *15*(1), 48. https://doi.org/10.1186/s13024-020-00400-9

Mansouri, K., Leite, M. T., Medeiros, F. A., Leung, C. K., & Weinreb, R. N. (2011). Assessment of rates of structural change in glaucoma using imaging technologies. *Eye (London, England)*, *25*(3), 269–277. https://doi.org/10.1038/eye.2010.202

Mazia, D., Schatten, G., & Sale, W. (1975). Adhesion of cells to surfaces coated with polylysine. Applications to electron microscopy. *The Journal of Cell Biology*, *66*(1), 198–200. https://doi.org/10.1083/jcb.66.1.198

McKetta, J. J., & Weismantel, G. E. (1999). *Water and wastewater treatment, protective coating system to zeolites*. *Encyclopedia of chemical processing and design / executive ed.: John J. McKetta: Vol. 67*. New York [u.a.]: Dekker.

Mehran, N. A., Sinha, S., & Razeghinejad, R. (2020). New glaucoma medications: Latanoprostene bunod, netarsudil, and fixed combination netarsudil-latanoprost. *Eye (London, England)*, *34*(1), 72–88. https://doi.org/10.1038/s41433-019-0671-0

Miglior, S., Zeyen, T., Pfeiffer, N., Cunha-Vaz, J., Torri, V., & Adamsons, I. (2005). Results of the European Glaucoma Prevention Study. *Ophthalmology*, *112*(3), 366–375. https://doi.org/10.1016/j.ophtha.2004.11.030

Mokhles, P., Schouten, J. S., Beckers, H. J., Azuara-Blanco, A., Tuulonen, A., & Webers, C. A. (2017). Glaucoma blindness at the end of life. *Acta Ophthalmologica*, *95*(1), 10–11. https://doi.org/10.1111/aos.12933

Musch, D. C., Gillespie, B. W., Niziol, L. M., Lichter, P. R., Varma, R., & CIGTS Study Group (2011). Intraocular pressure control and long-term visual field loss in the Collaborative Initial Glaucoma Treatment Study. *Ophthalmology*, *118*(9), 1766–1773. https://doi.org/10.1016/j.ophtha.2011.01.047

Nakano, T., Tatemichi, M., Miura, Y., Sugita, M., & Kitahara, K. (2005). Long-term physiologic changes of intraocular pressure: A 10-year longitudinal analysis in young and middle-aged Japanese men. *Ophthalmology*, *112*(4), 609–616. https://doi.org/10.1016/j.ophtha.2004.10.046

O'Gorman, L. (1996). *Document image analysis*. Los Alamitos, CA: IEEE computer Society.

Opstad, I. S., Wolfson, D. L., Øie, C. I., & Ahluwalia, B. S. (2018). Multi-color imaging of sub-mitochondrial structures in living cells using structured illumination microscopy. *Nanophotonics*, *7*(5), 935–947. https://doi.org/10.1515/nanoph-2017-0112

Otsu, N. (1979). A Threshold Selection Method from Gray-Level Histograms. *IEEE Transactions on Systems, Man, and Cybernetics*, *9*(1), 62–66. https://doi.org/10.1109/TSMC.1979.4310076

Park, S. K., Kim, J., Seomun, Y., Choi, J., Kim, D. H., Han, I. O., . . . Joo, C. K. (2001). Hydrogen peroxide is a novel inducer of connective tissue growth factor. *Biochemical and Biophysical Research Communications*, *284*(4), 966–971. https://doi.org/10.1006/bbrc.2001.5058

Pease, M. E., McKinnon, S. J., Quigley, H. A., Kerrigan-Baumrind, L. A., & Zack, D. J. (2000). Obstructed axonal transport of BDNF and its receptor TrkB in experimental glaucoma. *Investigative Ophthalmology & Visual Science*, *41*(3), 764–774.

Pena, J. D., Netland, P. A., Vidal, I., Dorr, D. A., Rasky, A., & Hernandez, M. R. (1998). Elastosis of the lamina cribrosa in glaucomatous optic neuropathy. *Experimental Eye Research*, *67*(5), 517–524. https://doi.org/10.1006/exer.1998.0539

Pena, J. D., Varela, H. J., Ricard, C. S., & Hernandez, M. R. (1999). Enhanced tenascin expression associated with reactive astrocytes in human optic nerve heads with primary open angle glaucoma. *Experimental Eye Research*, *68*(1), 29–40. https://doi.org/10.1006/exer.1998.0577

Prasov, L., Nagy, M., Rudolph, D. D., & Glaser, T. (2012). Math5 (Atoh7) gene dosage limits retinal ganglion cell genesis. *Neuroreport*, *23*(10), 631–634. https://doi.org/10.1097/WNR.0b013e328355f260

Quigley, H. A. (1996). Number of people with glaucoma worldwide. *The British Journal of Ophthalmology*, *80*(5), 389–393.

Quigley, H. A., & Broman, A. T. (2006). The number of people with glaucoma worldwide in 2010 and 2020. *The British Journal of Ophthalmology*, *90*(3), 262–267. https://doi.org/10.1136/bjo.2005.081224

Quigley, H. A., McKinnon, S. J., Zack, D. J., Pease, M. E., Kerrigan-Baumrind, L. A., Kerrigan, D. F., & Mitchell, R. S. (2000). Retrograde axonal transport of BDNF in retinal ganglion cells is blocked by acute IOP elevation in rats. *Investigative Ophthalmology & Visual Science*, *41*(11), 3460–3466.

Quigley, H. A. (2011). Glaucoma. *Lancet (London, England)*, *377*(9774), 1367–1377. https://doi.org/10.1016/S0140-6736(10)61423-7

Quigley, H. A. (2015). The contribution of the sclera and lamina cribrosa to the pathogenesis of glaucoma: Diagnostic and treatment implications. *Progress in Brain Research*, *220*, 59–86. https://doi.org/10.1016/bs.pbr.2015.04.003

Reinehr, S., Koch, D., Weiss, M., Froemel, F., Voss, C., Dick, H. B., . . . Joachim, S. C. (2019). Loss of retinal ganglion cells in a new genetic mouse model for primary open-angle glaucoma. *Journal of Cellular and Molecular Medicine*, *23*(8), 5497–5507. https://doi.org/10.1111/jcmm.14433

Reinhard, J., Wiemann, S., Hildebrandt, S., & Faissner, A. (2021). Extracellular Matrix Remodeling in the Retina and Optic Nerve of a Novel Glaucoma Mouse Model. *Biology*, *10*(3). https://doi.org/10.3390/biology10030169

Resnikoff, S., Pascolini, D., Mariotti, S. P., & Pokharel, G. P. (2008). Global magnitude of visual impairment caused by uncorrected refractive errors in 2004. *Bulletin of the World Health Organization*, *86*(1), 63–70. https://doi.org/10.2471/blt.07.041210

Rohen, J. W., Futa, R., & Lütjen-Drecoll, E. (1981). The fine structure of the cribriform meshwork in normal and glaucomatous eyes as seen in tangential sections. *Investigative Ophthalmology and Visual Science*, *21*(4), 574–585.

Rohen, J. W., Lütjen-Drecoll, E., Flügel, C., Meyer, M., & Grierson, I. (1993). Ultrastructure of the trabecular meshwork in untreated cases of primary open-angle glaucoma (POAG). *Experimental Eye Research*, *56*(6), 683–692. https://doi.org/10.1006/exer.1993.1085

Ronneberger, O., Fischer, P., & Brox, T. (2015). U-Net: Convolutional networks for biomedical image segmentation. In N. Navab, J. Hornegger, W. M. Wells, & A. F.

Frangi (Eds.), *Medical image computing and computer-assisted intervention – MICCAI 2015* (Lecture Notes in Computer Science, Vol. 9351, pp. 234–241). Springer. https://doi.org/10.1007/978-3-319-24574-4_28

Ross, M. H., & Pawlina, W. (2015). *Histology: A text and atlas* (7th ed.). Philadelphia: Wolters Kluwer/Lippincott Williams & Wilkins Health.

Savinova, O. V., Sugiyama, F., Martin, J. E., Tomarev, S. I., Paigen, B. J., Smith, R. S., & John, S. W. (2001). Intraocular pressure in genetically distinct mice: An update and strain survey. *BMC Genetics*, *2*, 12. https://doi.org/10.1186/1471-2156-2-12

Schindelin, J., Arganda-Carreras, I., Frise, E., Kaynig, V., Longair, M., Pietzsch, T., . . . Cardona, A. (2012). Fiji: An open-source platform for biological-image analysis. *Nature Methods*, *9*(7), 676–682. https://doi.org/10.1038/nmeth.2019

Schober, J. M., Chen, N., Grzeszkiewicz, T. M., Jovanovic, I., Emeson, E. E., Ugarova, T. P., . . . Lam, S. C.-T. (2002). Identification of integrin alpha(M)beta(2) as an adhesion receptor on peripheral blood monocytes for Cyr61 (CCN1) and connective tissue growth factor (CCN2): Immediate-early gene products expressed in atherosclerotic lesions. *Blood*, *99*(12), 4457–4465. https://doi.org/10.1182/blood.v99.12.4457

Segarini, P. R., Nesbitt, J. E., Li, D., Hays, L. G., Yates, J. R., & Carmichael, D. F. (2001). The low density lipoprotein receptor-related protein/alpha2-macroglobulin receptor is a receptor for connective tissue growth factor. *The Journal of Biological Chemistry*, *276*(44), 40659–40667. https://doi.org/10.1074/jbc.M105180200

Seitz, R., Ohlmann, A., & Tamm, E. R. (2013). The role of Müller glia and microglia in glaucoma. *Cell and Tissue Research*, *353*(2), 339–345. https://doi.org/10.1007/s00441-013-1666-y

Shiose, Y. (1990). Intraocular pressure: New perspectives. *Survey of Ophthalmology*, *34*(6), 413–435. https://doi.org/10.1016/0039-6257(90)90122-c

Shi-Wen, X., Leask, A., & Abraham, D. (2008). Regulation and function of connective tissue growth factor/CCN2 in tissue repair, scarring and fibrosis. *Cytokine & Growth Factor Reviews*, *19*(2), 133–144. https://doi.org/10.1016/j.cytogfr.2008.01.002

Smith, P. D., McLean, K. J., Murphy, M. A., Wilson, Y., Murphy, M., Turnley, A. M., & Cook, M. J. (2005). A brightness-area-product-based protocol for the quantitative assessment of antigen abundance in fluorescent immunohistochemistry. *Brain Research. Brain Research Protocols*, *15*(1), 21–29. https://doi.org/10.1016/j.brainresprot.2005.02.004

Stamer, W. D., Lei, Y., Boussommier-Calleja, A., Overby, D. R., & Ethier, C. R. (2011). eNOS, a pressure-dependent regulator of intraocular pressure. *Investigative Ophthalmology & Visual Science*, *52*(13), 9438–9444. https://doi.org/10.1167/iovs.11-7839

Steinhart, M. R., Cone-Kimball, E., Nguyen, C., Nguyen, T. D., Pease, M. E., Chakravarti, S., . . . Quigley, H. A. (2014). Susceptibility to glaucoma damage related to age and connective tissue mutations in mice. *Experimental Eye Research*, *119*, 54–60. https://doi.org/10.1016/j.exer.2013.12.008

Su, F., Luo, X., Du, Z., Chen, Z., Liu, Y., Jin, X., . . . Jin, D. (2022). High-Contrast Luminescent Immunohistochemistry Using PEGylated Lanthanide Complexes. *Analytical Chemistry*, *94*(50), 17587–17594. https://doi.org/10.1021/acs.analchem.2c04058

Suvarna, S. K., Layton, C., & Bancroft, J. D. (2019). *Bancroft's theory and practice of histological techniques* (8th ed.). Elsevier.

Swain, D. L., Yasmin, S., Fernandes, B., Lamaj, G., Su, Y., & Gong, H. (2022). Schlemm's Canal Endothelium Cellular Connectivity in Giant Vacuole and Pore Formation in Different Flow-type Areas: A Serial Block-Face Scanning Electron Microscopy Study. *Frontiers in Cell and Developmental Biology*, *10*, 867376. https://doi.org/10.3389/fcell.2022.867376

Tamm, E. R. (2009). The trabecular meshwork outflow pathways: Structural and functional aspects. *Experimental Eye Research*, *88*(4), 648–655. https://doi.org/10.1016/j.exer.2009.02.007

Tamm, E. R., & Fuchshofer, R. (2007). What increases outflow resistance in primary open-angle glaucoma? *Survey of Ophthalmology*, *52 Suppl 2*, S101-4. https://doi.org/10.1016/j.survophthal.2007.08.002

Tektas, O.-Y., & Lütjen-Drecoll, E. (2009). Structural changes of the trabecular meshwork in different kinds of glaucoma. *Experimental Eye Research*, *88*(4), 769–775. https://doi.org/10.1016/j.exer.2008.11.025

Templeton, J. P., Struebing, F. L., Lemmon, A., & Geisert, E. E. (2014). Imagepad, a novel counting application for the Apple iPad, used to quantify axons in the mouse optic nerve. *Experimental Eye Research*, *128*, 102–108. https://doi.org/10.1016/j.exer.2014.10.001

Tezel, G., & Wax, M. B. (2003). Glial modulation of retinal ganglion cell death in glaucoma. *Journal of Glaucoma*, *12*(1), 63–68. https://doi.org/10.1097/00061198-200302000-00014

Tian, B., Geiger, B., Epstein, D. L., & Kaufman, P. L. (2000). Cytoskeletal involvement in the regulation of aqueous humor outflow. *Investigative Ophthalmology & Visual Science*, *41*(3), 619–623.

Tomarev, S. I., Wistow, G., Raymond, V., Dubois, S., & Malyukova, I. (2003). Gene expression profile of the human trabecular meshwork: Neibank sequence tag analysis. *Investigative Ophthalmology and Visual Science*, *44*(6), 2588–2596. https://doi.org/10.1167/iovs.02-1099

Tuck, M. W., & Crick, R. P. (1998). The age distribution of primary open angle glaucoma. *Ophthalmic Epidemiology*, *5*(4), 173–183.

Van Setten, G.-B., Blalock, T. D., Grotendorst, G., & Schultz, G. S. (2002). Detection of connective tissue growth factor in human aqueous humor. *Ophthalmic Research*, *34*(5), 306–308. https://doi.org/10.1159/000065601

Vangindertael, J., Camacho, R., Sempels, W., Mizuno, H., Dedecker, P., & Janssen, K. P. F. (2018). An introduction to optical super-resolution microscopy for the adventurous biologist. *Methods and Applications in Fluorescence*, *6*(2), 22003. https://doi.org/10.1088/2050-6120/aaae0c

Vranka, J. A., Bradley, J. M., Yang, Y.-F., Keller, K. E., & Acott, T. S. (2015). Mapping molecular differences and extracellular matrix gene expression in segmental outflow pathways of the human ocular trabecular meshwork. *PloS One*, *10*(3), e0122483. https://doi.org/10.1371/journal.pone.0122483

Wahab, N. A., Weston, B. S., & Mason, R. M. (2005). Connective tissue growth factor CCN2 interacts with and activates the tyrosine kinase receptor TrkA. *Journal of the American Society of Nephrology : JASN*, *16*(2), 340–351. https://doi.org/10.1681/ASN.2003100905

Weinreb, R. N., Aung, T., & Medeiros, F. A. (2014). The pathophysiology and treatment of glaucoma: A review. *JAMA*, *311*(18), 1901–1911. https://doi.org/10.1001/jama.2014.3192

Weinreb, R. N., & Khaw, P. T. (2004). Primary open-angle glaucoma. *Lancet (London, England)*, *363*(9422), 1711–1720. https://doi.org/10.1016/S0140-6736(04)16257-0

Welge-Lüssen, U., May, C. A., & Lütjen-Drecoll, E. (2000). Induction of tissue transglutaminase in the trabecular meshwork by TGF-beta1 and TGF-beta2. *Investigative Ophthalmology and Visual Science*, *41*(8), 2229–2238.

Wiederholt, M., Thieme, H., & Stumpff, F. (2000). The regulation of trabecular meshwork and ciliary muscle contractility. *Progress in Retinal and Eye Research*, *19*(3), 271–295. https://doi.org/10.1016/s1350-9462(99)00015-4

Williams, R. W., Strom, R. C., Rice, D. S., & Goldowitz, D. (1996). Genetic and Environmental Control of Variation in Retinal Ganglion Cell Number in Mice. *The Journal of Neuroscience : The Official Journal of the Society for Neuroscience*, *16*(22), 7193–7205. https://doi.org/10.1523/JNEUROSCI.16-22-07193.1996

Winter, P. D., Leoni, P., & Abraham, D. (2008). Connective tissue growth factor: Structure-function relationships of a mosaic, multifunctional protein. *Growth Factors (Chur, Switzerland)*, *26*(2), 80–91. https://doi.org/10.1080/08977190802025602

Zarei, K., Scheetz, T. E., Christopher, M., Miller, K., Hedberg-Buenz, A., Tandon, A., . . . Abràmoff, M. D. (2016a). Automated Axon Counting in Rodent Optic Nerve Sections with AxonJ. *Scientific Reports*, *6*, 26559. https://doi.org/10.1038/srep26559

Zarei, K., Scheetz, T. E., Christopher, M., Miller, K., Hedberg-Buenz, A., Tandon, A., . . . Abràmoff, M. D. (2016b). Corrigendum: Automated Axon Counting in Rodent Optic Nerve Sections with AxonJ. *Scientific Reports*, *6*, 34124. https://doi.org/10.1038/srep34124

8 Tables

9 Figures

10 Abbreviations

AH	aqueous humour
BSA	bovine serum albumin
cDNA	complementary deoxyribonucleic acid
CTGF	connective tissue growth factor
CWFG	cold water fish gelatine
DAPI	4′,6-Diamidin-2-phenylindol
dH_2O	purified water
DNA	deoxyribonucleic acid
dNTPs	deoxynucleotide triphosphates
ECM	extracellular matrix
EDTA	ethylenediaminetetraacetic acid
EM	electron microscopy
FI	Fourier image
FN	fibronectin
FT	Fourier Transform
g b. wt.	gram body weight
HCl	hydrochloric acid
ICA	iridocorneal angle
IgG	immune globulin G
IOP	intraocular pressure
JCT	juxtacannalicular tissue
LC	lamina cribrosa
MMP	matrix metallo proteinase
mRNA	messenger ribonucleic acid
NaCl	sodium chloride
ON	optic nerve
ONH	optic nerve head
PB	phosphate buffer
PBS	phosphate-buffered saline
PCR	polymerase chain reaction
PFA	paraformaldehyde
POAG	primary open angle glaucoma
RhoA	Ras homolog gene family, member A
RT	room temperature
SC	Schlemm’s canal
SD	standard deviation
SIM	Structured Illumination Microscopy
TBE	Tris-borat-EDTA
tg	transgenic
TGF-β	transforming growth factor β
TM	trabecular meshwork
WT	wildtype
α-SMA	α-smooth muscle actin

11 Acknowledgements

Eine Promotion ist nie eine Einzelleistung, sondern immer das Ergebnis einer umfangreichen Zusammenarbeit. Diese erstreckt sich zum einen auf die Arbeit am Lehrstuhl – daher möchte ich Rudolf Fuchshofer für seine Unterstützung danken. Er begleitete mich nicht nur bei meinen ersten Schritten in der Wissenschaft, sondern gab mir auch große Freiheit bei der Umsetzung meiner Ideen – sei es während meiner zahlreichen Auslandsaufenthalte oder bei der Entwicklung neuer Methoden.

Er war es auch, der mich in die Hände meiner Betreuerin Franziska Frömel gab, deren Geduld und Unterstützung außergewöhnlich waren. Mein großer Dank gilt auch den Laborantinnen Angelika, Elke, Margit und Silvia: Sie hatten stets ein offenes Ohr für meine Fragen und Freude daran, Neues auszuprobieren. Auch allen weiteren Mitarbeitenden des Lehrstuhls danke ich herzlich – dank ihnen herrschte bei der Arbeit stets eine positive und produktive Atmosphäre.

Aber auch außerhalb des Lehrstuhls durfte ich prägende Begegnungen machen. Ich hatte die Gelegenheit, sowohl das Schnabl-Labor in San Diego als auch die Nanoskopie-Gruppe in Tromsø zu besuchen. Yi Duan zeigte mir, was es bedeutet, ein guter und ehrlicher Wissenschaftler zu sein. Ida Opstad und Florian Ströhl eröffneten mir mit ihrem ganz anderen fachlichen Hintergrund neue Perspektiven – ohne sie würde ich SIM vermutlich noch immer falsch erklären.

Wissenschaft findet nie im leeren Raum statt. Mein besonderer Dank gilt meiner Frau, meiner Familie und meinen Freunden, die für mich sicherer Halt und große Stütze sind – menschlich, und im Fall meines Bruders Fabian auch fachlich. Ohne diese umfangreiche Unterstützung wäre dieser Arbeit nicht möglich gewesen.

13 Erklärung

Diese Dissertation ist auf Anregung und unter Supervision von Professor Rudolf Fuchshofer am Lehrstuhl für Humananatomie und Embryologie der Universität Regensburg entstanden. Die Betreuung im Labor oblag Doktor Franziska Frömel (geb. Scherl).

Ich erkläre hiermit, dass ich die vorliegende Arbeit ohne unzulässige Hilfe Dritter und ohne Benutzung anderer als der angegebenen Hilfsmittel angefertigt habe. Die aus anderen Quellen direkt oder indirekt übernommenen Daten und Konzepte sind unter Angabe der Quelle gekennzeichnet. Insbesondere habe ich nicht die entgeltliche Hilfe von Vermittlungs- bzw. Beratungsdiensten (Promotionsberater oder andere Personen) in Anspruch genommen. Niemand hat von mir unmittelbar oder mittelbar geldwerte Leistungen für Arbeit erhalten, die im Zusammenhang mit dem Inhalt der vorgelegten Dissertation stehen. Die Arbeit wurde bisher weder im In- noch im Ausland in gleicher oder ähnlicher Form einer anderen Prüfungsbehörde vorgelegt.

Zürich, 31.08.2025 Felix Hutmacher